Piezoelectric Transducers Based on Aluminum Nitride and Polyimide for Tactile Applications

POLITECNICO DI TORINO

SCUOLA INTERPOLITECNICA DI DOTTORATO

Doctoral Program in Material Science and Technology

Final Dissertation

Piezoelectric Transducers Based on Aluminum Nitride and Polyimide for Tactile Applications

Vincenzo Mariano Mastronardi

Tutor
Prof. Fabrizio C. Pirri

Co-tutor
Prof. Ing. Massimo De Vittorio
Dr. Francesco Rizzi

Co-ordinator of the Research Doctorate Course
Prof. Claudio Francesco Badini

04/04/2016

Nothing is impossible! Not if you can imagine it

ACKNOWLEDGMENTS

The author would like to thank the advisor Professor Massimo De Vittorio for his guidance and assistance throughout this thesis project. He has always provided encouragement and very helpful suggestions along the way.

I am sincerely grateful to my former supervisor Dr. Simona Petroni whose precious suggestions, teachings and support have been essential during this work. Thanks to have conveyed to me the knowledge in the area of research.

I would like to really thank Dr. Francesco Rizzi who has been greatly supportive with his profound knowledge and enthusiasm, especially during the last period of my activity. His help and suggestions have been crucial for the conclusion of this work.

I would like to thank also Gianmichele Epifani, the clean room technician specialist, for his fundamental contribute to the optimization of the fabrication processing. I am grateful too to Dr. Ing. Tiziana Stomeo and Dr. Ing. Antonio Qualtieri for their patience and support for the clean room security, trainings and ready help with laboratory facilities.

I am grateful to Prof. Skandar Basrour and Prof. Libor Rufer for the privilege of working in TIMA laboratories, in Grenoble (France), for their teachings and the availability during all my stay in France.

Additional thanks go to all my group lab-mates: Tommaso, Francesco, Massimiliano, Davide, Barbara, and Mino for the enlightening discussions and a lot of really funny moments.

I worked hard for the development and the success of this project and I hope this thesis will be helpful to those who follow.

TABLE OF CONTENTS

ABSTRACT

The development of micro systems with smart sensing capabilities is paving the way to progresses in the technology for humanoid robotics. The importance of sensory feedback has been recognized the enabler of a high degree of autonomy for robotic systems. In tactile applications, it can be exploited not only to avoid objects slipping during their manipulation but also to allow safe interaction with humans and unknown objects and environments. In order to ensure the minimal deformation of an object during subtle manipulation tasks, information not only on contact forces between the object and fingers but also on contact geometry and contact friction characteristics has to be provided. Touch, unlike other senses, is a critical component that plays a fundamental role in dexterous manipulation capabilities and in the evaluation of objects properties such as type of material, shape, texture, stiffness, which is not easily possible by vision alone. Understanding of unstructured environments is made possible by touch through the determination of stress distribution in the surrounding area of physical contact. To this aim, tactile sensing and pressure detection systems should be integrated as an artificial tactile system.

As illustrated in the Chapter I, the role of external stimuli detection in humans is provided by a great number of sensorial receptors: they are specialized endings whose structure and location in the skin determine their specific signal transmission characteristics. Especially, mechanoreceptors are specialized in the conversion of the mechanical deformations caused by force, vibration or slip on skin into electrical nerve impulses which are processed and encoded by the central nervous system.

Highly miniaturized systems based on MEMS technology seem to imitate properly the large number of fast responsive mechanoreceptors present in human skin. Moreover, an artificial electronic skin should be lightweight, flexible, soft and wearable and it should be fabricated with compliant materials. In this respect a big challenge of bio-inspired technologies is the efficient application of flexible active materials to convert the mechanical pressure or stress into a usable electric signal (voltage or current).

In the emerging field of soft active materials, able of large deformation, piezoelectrics have been recognized as a really promising and attractive material in both sensing and actuation applications. As outlined in Chapter II, there is a wide choice of materials and material forms (ceramics: PZT; polycrystalline films: ZnO, AlN; polymers and copolymers: PVDF, PVDF-TrFe) which are actively piezoelectric and exhibit features more or less attractive. Among them, aluminum nitride is a promising piezoelectric material for flexible technology. It has moderate piezoelectric coefficient, when available in *c*-axis oriented polycrystalline columnar structure, but, at same time, it exhibits low dielectric constant, high temperature stability, large band gap, large electrical resistivity, high breakdown voltage and low dielectric loss which make it suitable for

transducers and high thermal conductivity which implies low thermal drifts. The high chemical stability allows AlN to be used in humid environments. Moreover, all the above properties and its deposition method make AlN compatible with CMOS technology. Exploiting the features of the AlN, three-dimensional AlN dome-shaped cells, embedded between two metal electrodes, are proposed in this thesis. They are fabricated on general purpose Kapton™ substrate, exploiting the flexibility of the polymer and the electrical stability of the semiconductor at the same time. As matter of fact, the crystalline layers release a compressive stress over the polymer, generating three-dimensional structures with reduced stiffness, compared to the semiconductor materials.

In Chapter III, a mathematical model to calculate the residual stresses which arise because of mismatch in coefficient of thermal expansion between layers and because of mismatch in lattice constants between the substrate and the epitaxially grown films is adopted. The theoretical equation is then used to evaluate the dependence of geometrical features of the fabricated three-dimensional structures on compressive residual stress. Moreover, FEM simulations and theoretical models analysis are developed in order to qualitative explore the operation principle of curved membranes, which are labelled dome-shaped diaphragm transducers (DSDT), both as sensors and as piezo-actuators and for the related design optimization.

For the reliability of the proposed device as a force/pressure sensor and piezo-actuator, an exhaustive electromechanical characterization of the devices is carried out. A complete description of the microfabrication processes is also provided. As shown in Chapter IV, standard microfabrication techniques are employed to fabricate the array of DSDTs. The overall microfabrication process involves deposition of metal and piezoelectric films, photolithography and plasma-based dry and wet etching to pattern thin films with the desired features. The DSDT devices are designed and developed according to FEM and theoretical analysis and following the typical requirements of force/pressure systems for tactile applications.

Experimental analyses are also accomplished to extract the relationship between the compressive residual stress due to the aluminum nitride and the geometries of the devices. They reveal different deformations, proving the dependence of the geometrical features of the three-dimensional structures on residual stress. Moreover, electrical characterization is performed to determine capacitance and impedance of the DSDTs and to experimentally calculate the relative dielectric constant of sputtered AlN piezoelectric film.

In order to investigate the mechanical behaviour of the curved circular transducers, a characterization of the flexural deflection modes of the DSDT membranes is carried out. The natural frequency of vibrations and the corresponding displacements are measured by a Laser Doppler Vibrometer when a suitable oscillating voltage, with known amplitude, is applied to drive the piezo-DSDTs.

Finally, being developed for tactile sensing purpose, the proposed technology is tested in order to explore the electromechanical response of the device when impulsive dynamic and/or long

static forces are applied. The study on the impulsive dynamic and long static stimuli detection is then performed by using an *ad hoc* setup measuring both the applied loading forces and the corresponding generated voltage and capacitance variation. These measurements allow a thorough test of the sensing abilities of the AlN-based DSDT cells.

Finally, as stated in Chapter V, the proposed technology exhibits an improved electromechanical coupling with higher mechanical deformation per unit energy compared with the conventional plate structures, when the devices are used as piezo-actuator. On the other hand, it is well suited to realize large area tactile sensors for robotics applications, opening up new perspectives to the development of latest generation biomimetic sensors and allowing the design and the fabrication of miniaturized devices.

CHAPTER I

Contents

Summary

This chapter provides an introduction of the fundamental mechanism for touch sensations in humans. It explores the motivation for the design and the development of a bio-inspired artificial tactile system that mimics the abilities of human receptors, to be integrated on artificial fingertips and to perform advanced in-hand manipulation tasks.

The first two paragraphs provide an introduction of the morphology of the human tactile system as an active sensory system. A detailed description of the most important properties of human skin receptors and their principal functions is, here, presented.

Moreover, the last paragraphs are devoted to a brief and general overview of the biologically inspired artificial mechano-sensors based on microelectro-mechanical systems. Some design criteria, useful to develop an artificial tactile system are given, showing the corresponding applications in an artificial system. Finally, a classification of the most commonly used transduction mechanisms with reference to researches carried out to date is provided.

INTRODUCTION AND BACKGROUND

Nature has always inspired humans, providing an inexhaustible amount of examples as sources of inspiration, in terms of materials, structures, mechanisms, tools, systems and methods. The field of nature imitation is known as *Biomimetics* and offers enormous potential for inspiring and mimicking new capabilities for the future technologies. One of the most substantial purposes of biomimetics includes the extraction of nature's solutions to be implemented in order to increase the

value and the functionality of man-made mechanical designs and engineering solutions, especially in robotics and bio-inspired robotics.

The interaction of robots with unstructured and complex environments requires the acquisition of qualitative and quantitative information. Biomimetics of sensors and sensing systems are, therefore, essential components because they increase stimulus detection probability, sensitivity and signal discrimination, as natural sensing systems. Pressure, temperature, optical and acoustic sensors are some examples and efforts are made to improve their sensing capability and to reduce their size and power consumption. In such a way, humanoids can apply the right behaviours and takes proper decisions in response to external stimuli.

1.1. BIOLOGICALLY INSPIRED TECHNOLOGY FOR HUMAN INNOVATION

In recent years, research activities on autonomous robotic machines have been focused on the development of so-called *"Artificial Intelligence (AI)"*. This science is mainly based on the use of powerful and high-speed computers to model and replicate human behaviour. It covers a broad range of problems that arise in fields such as robotics, e-commerce, medical diagnostics, gaming, mathematics. Moreover, *AI* science focuses on the development of tools and algorithms coming from computer science allowing artificial machines to learn and perform intelligent tasks with minimal or without any human intervention.

In the last decade, a new branch of robotic engineering, known as *Cognitive Robotics (RC)*, has been developed. In opposition to the classical *AI*, *RC* science is concerned with giving to robotic machines intelligent capabilities by providing them with complex architectures and allowing to process information by the interaction with surrounding world. Robots can learn not only from human teaching, but even from own experience, developing abilities to effectively deal with surrounding environment. The primary goal of cognitive robotics is to make robots to act and react appropriately in real-world situations by providing them with functions including machine vision, voice recognition, proximity sensing, pressure sensing, texture sensing, programmable and imitation motion, ability to learn from mistakes and to explore on their own. So, the robotic intelligence evolves and lies on the availability and processing of information which come from a complex sensory system and are crucial for providing an intelligent and adaptive behavior.

Recent technological developments of Micro Electro Mechanical System (MEMS), with low costs and power consumption and reduced size and mass, have allowed engineers to focus to biomimetic sensors designs, i.e. to artificial sensors which are able to reproduce and mimic biological sensors for applications in robotics and biorobotics and, in general, in mechatronic and

biomechatronic machines. The combination of organic and inorganic materials, hybrid artificial-biological micro-structures and *"BioMEMS"*, shifted the trend in biomimetic sensor technology from discrete single function sensors to composite structures including integrated sensing, actuation and signal processing, exploiting high sensitivities and consolidated electronics for readouts [1-3]. Moreover, through miniaturization, high density of elements can be incorporated within a small area allowing the integration of electronics and sensing elements on same substrate to mimic the functionality of biological system through a variety of sensing structures. This opens up new perspectives to the development of latest generation biomimetic sensors, allowing the design and the fabrication of miniaturized devices which are realized with different materials and with sensing and processing capabilities difficult to obtain until now.

1.2. FROM HUMAN BIOLOGY TO BIOROBOTICS

Human tactile system has raised a huge attention in biorobotics. Humans use their five senses to observe and get information from surrounding environment. In such a case, tactile sensing plays an essential role in manipulating tools or objects, as well as for feature exploration and interaction.

Tactile sensing can be defined as the detection and measurement of contact parameters in a predetermined contact area and a subsequent pre-processing of signals. Touch provides information about contact forces, torques and contact distribution and, by means of exploration, the identification of object properties such as geometry, stiffness and texture. These properties can be better estimated by touching or mechanically interacting with objects, as humans do. The sense of touch also provides action related information, such as slip and helps in carrying out actions (for example, rolling an object between fingers without dropping it) [4, 5].

1.2.1. MORPHOLOGY OF HUMAN TACTILE SYSTEM

The tactile sense of humans is an active sensory organ extremely accurate and sensitive. In both human hairy and non-hairy skin, the role of external stimuli detection is provided by a great number of sensorial receptors: they are specialized endings whose structure and location in the skin determine their specific signal transmission characteristics. In the skin, thermoreceptors are involved in sensing and transducing temperature stimuli (heat and cold) whereas nocioreceptors deal with sensing pain and/or damage. Mechanoreceptors are specialized in the conversion of the mechanical deformations caused by force, vibration or slip of skin into electrical nerve impulses.

When skin is deformed, the corresponding deformation is transmitted from its surface to the mechanoreceptor's plasma membrane, causing ion channels to open and alter the membrane potential of the cell to create a graded potential, which in turn leads to the release of neurotransmitter or the generation of spikes of action potentials. In general, the magnitude of generated output voltages from tactile receptors is transformed in a train of actions potentials spikes and it is sent to the central nervous system, which processes and encodes received signals [6, 7]. A basic schematic of the conversion and perception of a stimulus during the interaction between skin and contact object is shown in Figure 1.1.

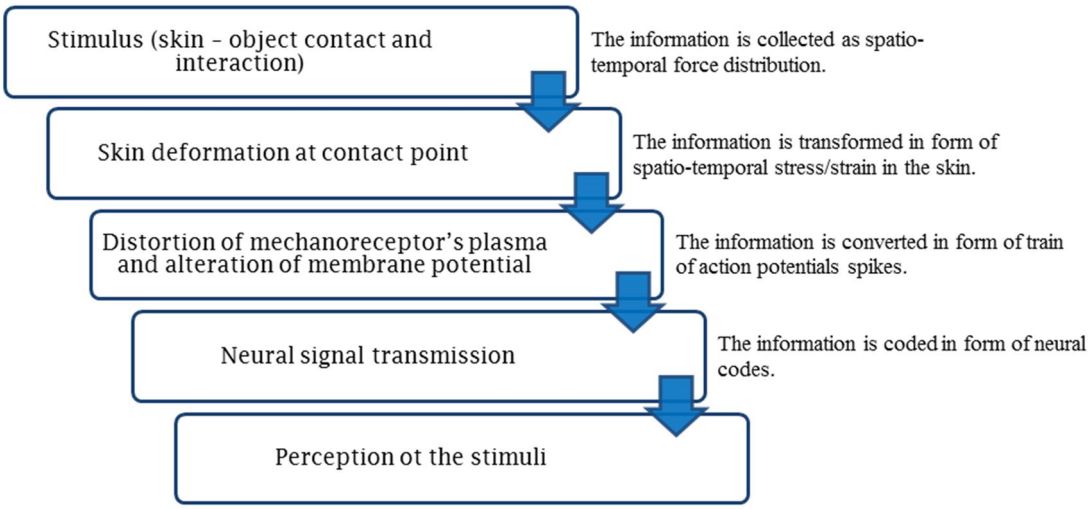

Figure 1.1: Schematic flow of the interaction between skin and object.

Hairless human skin, especially on the fingertips, contains four different types of neural tactile sensors. They can be classified into two main categories: static and dynamic. While static sensors are sensitive to temporally constant pressure, dynamic sensors react to time-variant stimuli. The most important tactile receptors reacting to static pressure are Merkel's discs and Ruffini endings. Merkel's discs, as well as Ruffini endings, adapt rather slowly to the stimuli. For this reason, they are classified also as slow adaptation (SA) mechanoreceptors because they continue to react in response to steady pressure of the skin. Merkel's discs provide continuous information about things touching the skin and are particularly sensitive to edges, comers and points, providing excellent detection of pressure intensity. Ruffini endings are suitable to provide information about vibrating stimuli of low frequencies and are also responsible of detecting shear on skin. They respond more actively to stretch than to indentation and are particularly sensitive to the shape of large objects.

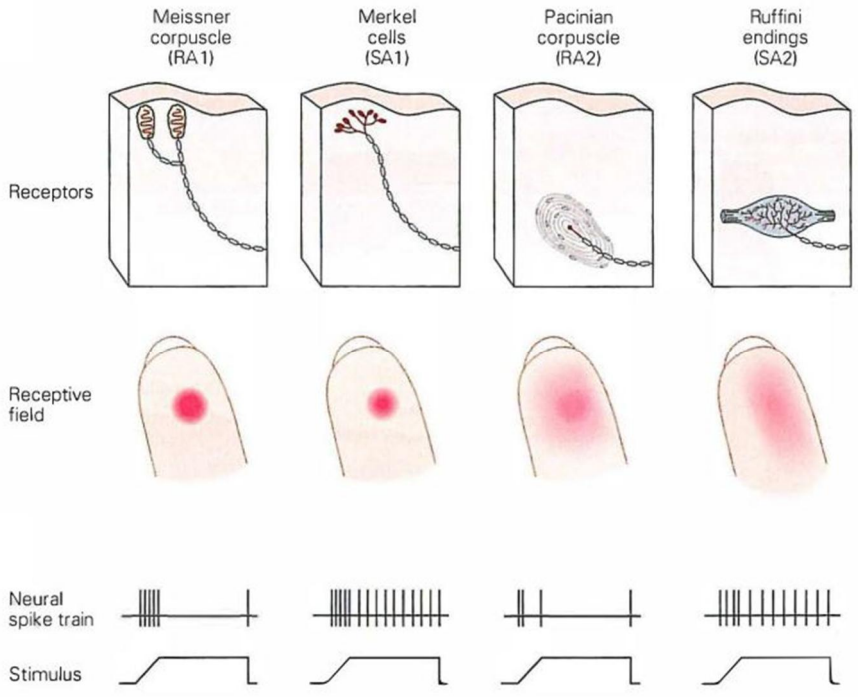

Figure 1.2: Schematic representation of human skin receptors. Skin can feel many sensations by the mechanoreceptors as a multi-modal sensing system (Adapted from Kandel, 2014 [8]).

Meissner's corpuscles, found primarily in non-hairy skin, and Pacinian corpuscles are involved in the reaction to vibrations or changes of indentation speed. They are very sensitive but adapt rapidly, so they are classified as fast adaptation (FA) mechanoreceptors because they respond to the motion of skin but not to steady pressure. Meissner's cells provide information about changes in things touching the skin, i.e. during the rolling of a small object between fingers (rather than holding it still) to discern its shape and texture. These receptors detect the initial contact with objects, slippage and motion of the hand over textured surfaces. For this reason, they are velocity detectors, since they move with the ridged skin allowing best reception of movement across it. Finally, Pacinian corpuscles provide detection and information about vibrating stimuli at high frequencies in tools and objects. Basically, they are acceleration detectors and respond to motion in nanometer range.

The biology and mechanical properties of human skin dictate how mechanoreceptors respond to a mechanical stimulus. In general, the receptive field of a mechanoreceptor reflects the location and its distribution in the skin. Therefore, touch receptors located closer to superficial layers of skin have smaller receptive field than those in deep layers [8-11]. Figure 1.2 shows a schematic picture of human skin mechanoreceptors and the corresponding neural spike train as response to the external stimulus. Even a very small piece of skin contains a variety of sensory cells that differ in morphology, innervation patterns, location in the skin, receptive field size and physiological responses to touch, making the skin a multi-modal sensing system. The picture also

shows the nerve fibers, innervating each type of mechanoreceptor, respond differently when activated. The spike trains are the responses of each type of nerve when its receptor is activated. The RA type fibers that innervate Meissner and Pacinian corpuscles adapt rapidly to constant stimulation while the SA type nerves that innervate Merkel cells and Ruffini endings adapt slowly [8]. A summary of the most important characteristics of human skin mechanoreceptors is listed in Table I.1 [12].

Table I.1

Summary of the tactile units, properties and principal functions

Endings	**Merkel's Disk**	**Ruffini Corpuscles**	**Meissner's Corpuscles**	**Pacinian Corpuscles**
Category	Static		Dynamic	
Class	SA I	SA II	FA I	FA II
Location	Shallow	Deep	Shallow	Deep
Number of endings/unit	4 – 7	1	12 – 17	1
Adaptation	Slow	Slow	Fast	Fast
Fiber innervation density (per cm^2)				
Fingertip	70	49	140	21
Distal phalax	42	28	77	15
Proximal and Middle phalax	30	14	37	10
Percentage in human hand	25%	20%	40%	10-15%
Receptive field (mm^2)	11	59	13	101
Spatial resolution	Good	Fair	Poor	Very Poor
Frequency range of stimuli (Hz)	0.4-3	100-500+	3-40	40-500+
Effective stimuli	Spatial deformation; Sustained pressure; Curvature, edges, corners	Sustained downward pressure; Lateral skin stretch; Skin slip	Temporal changes in skin deformation	Temporal changes in skin deformation
Sensory function	Low-frequency vibrations; Grip control; Tactile flow perception	Shape detection; Texture perception; Tactile flow detection	Finger position; Stable grasp; Tangential force; Motion direction	High-frequency vibrations

1.3. BIOLOGICALLY INSPIRED MECHANO-SENSORS

Neuroscience has long demonstrated the importance of tactile feedback in human manipulation. Furthermore, the development of multi-fingered robotic hands has increased the interest in tactile sensing for robotic manipulation utilizing tactile sensing for real-time control. A

great deal of effort has been devoted to developing artificial tactile sensors that can provide sufficient information for pressure and force measurements in a broad range of applications, as automated assembling, machining, sorting and stacking production, in minimal invasive medical surgery for evaluation of tissues stiffness as well as in prosthetic and orthotic devices for restoring loss of tactile sense.

Especially, humanoid robots need tactile interfaces for a safe interaction with humans in daily routines activities for assistance and co-existence for support and enhancement of human life. Equipping robots with specific sensors and transducers is a way to confer them sufficient autonomy to perform tasks, especially in unstructured environments (houses, offices, restaurants and so on). An artificial tactile system that emulates abilities of humans and performs advanced in-hand manipulation tasks should detect dynamic forces, such as normal and tangential contact for gathering spatial and geometrical information from surfaces exploration, as well as static forces, as human tactile system does. To this aim, arrays of pressure-sensitive sensors should be integrated on the robot fingertips as an electronic skin and flexibility, conformability and stretchability are desirable properties to increase the anthropomorphism.

On the basis of human tactile sensing system properties, pressure and force biomimetic sensors for manipulation applications should meet important design criteria. First of all, a rather high spatial resolution is required especially in in-hand manipulation of objects. High spatial resolution results in very small sensing cells. But the higher is the spatial resolution, the longer is the acquisition and processing time and larger the number of wire connections. Furthermore, as the sensing cells become smaller and smaller, the sensitivity to external electromagnetic noise and crosstalk increases. For this reason, the requirements of spatial resolution depend mainly on the position where the sensors are placed. As an example, fingertips require a resolution of ~1-2 mm, whereas on less sensitive parts like palm, the spatial resolution decreases up to 5-10 mm.

Sensitivity, defined as the smallest detectable variation in pressure/force, is very important especially in manipulation tasks. The dynamic range – the range from the minimum to maximum detectable pressure/force – is closely related to the sensitivity. Desirable values for sensitivity and dynamic range are 1 mN and 1000:1 (the maximum detectable force/pressure must be 1000 times greater than the minimum force/pressure), respectively.

Frequency response depends on the application of static rather than dynamic operation. The detectable vibration frequencies in humans vary from 5 to 400 Hz. Thus the frequency response should be significant at least up to 400 Hz for a dynamic sensor.

Surface properties, such as mechanical compliance and surface friction coefficient should fit to the manipulation tasks, i.e. low friction of sensor surface is needed in tactile exploration.

Robustness is necessary to guarantee highly repetitive usage of the sensors without loss of performances. Sensors should withstand various external conditions related to temperature,

humidity, radiation, chemical stresses and especially rather strong mechanical loads. At same time, they should be flexible enough in order to be attached to any type of surfaces.

Finally, hysteresis and memory effects ideally must be as low as possible in order to provide a stable, monotonic and repeatable output [12-14]. Kappassov Z. et al [13] have proposed a classification of pros and cons and possible applications according to the design criteria previously mentioned, as listed in the Table I.2.

Several technological approaches have been used to realize a low-cost, large-area-compatible artificial skin, suitable for object manipulation, with sufficient sensitivity in a wide pressure range (10–100 kPa) and that can meet the design criteria previously mentioned. One promising approach for biomimetic tactile sensors is based on silicon-based MEMS detecting inertial forces by capacitance variation or resistance variation of strain gauges. This kind of sensors shows high spatial resolution, reliable response and linearity, but they are brittle and not suitable for large deformations and coverage of three-dimensional curved surfaces. To overcome these limits, tactile sensors made of flexible materials have been integrated on various polymer-based materials as flexible substrates to make them able to bend, expand and adapt on irregular surfaces.

A first rough classification of pressure/force sensors can be made according to the most relevant technological approach, allowing to transduce the mechanical stimulus of touch into signals (mainly electrical).

Table I.2

Design criteria: pros and cons

Criteria	Pros	Cons	Applications
High spatial resolution	Smaller objects can be recognized features with higher precision can be detected	Smaller sensitivity and longer processing time	Contact pattern recognition and fine manipulation
High sensitivity	Smaller changes of contact forces can be detected	Dynamic range of the sensor narrows and the spatial resolution decreases	Light detection and fragile object manipulation
High frequency response	Fast response to the changes in the level of contact forces	Spatial resolution and dynamic range decrease	Detection of slip and texture recognition
Low hysteresis	High frequency response	Decrease of surface friction	Detection of slip and texture recognition
Low number of wire connections	The workspace does not change	Decrease of frequency response in serial data communication	Dexterous manipulation
High surface friction	Insuring stable grasp without application of high forces	Reduction of frequency response in soft paddings operation	Grasping

(Kappassov Z. et al. [13])

A tactile sensor can be designed on the basis of various transduction methods and of new materials. Focusing the attention on transduction methods, a second classification allows sensors to be classified in terms of coupled and/or non-coupled mechanical and electrical transduction. They are usually fabricated using standard MEMS technologies such as films deposition, plasma etching and photolithography.

1.3.1. METHODS FOR TACTILE SENSING: INDIRECT ELECTROMECHANICAL TRANSDUCTION

The working principles among indirect electromechanical transductions are optical, ultrasonic and magnetic methods.

Optical sensing [15-17] is based on optical reflection between mediums with different refractive indices. Optical force sensors usually contain a load transduction medium for applying the external force, a source of light, generally an array of infrared light-emitting diodes or a laser and a photo-detector (a photodiode) able to sense ranks of illumination, refractive index or spectrum of the light source that is proportionally varying with the magnitude of applied pressure on load medium. Sensors based on optical method have good spatial resolution, sensitivity, high repeatability and complete immunity from electro-magnetic interference, but they are relatively big in size and expensive in term of power consumption and computational circuitry.

The touch sensors based on magnetic transduction are usually developed measuring changes in magnetic flux using the Hall Effect or magnetoresistances, or measuring the changes in the magnetic coupling or in the inductance of a coil when a pressure is applied. Hall Effect-based sensors are only sensitive to magnetic fields in one direction while magnetoresistive sensors can be used to detect magnetic field having any orientation within a plane normal to the current flow. The magnetic-coupled or inductance-based sensors have the core generally made of magnetoelastic materials that deform under pressure and cause magnetic coupling between transformer windings or a coil's inductance to change. Tactile sensors based on magnetic principle have a number of advantages including high sensitivity and wide dynamic range, no mechanical hysteresis, linear response, and physical robustness. Nevertheless, they cannot be used in a magnetic medium [18-20].

An interesting example where mechanical transduction is decoupled from electrical transduction is represented by ultrasonic sensors. A typical ultrasonic sensor consists of a thin rubber layer that is deformed by the pressure: the amount of the deformation depends upon the magnitude of applied force and the stiffness of rubber. These sensors are composed of ultrasonic transmitters and receivers, both of them are covered by the rubber: the transmitters generate a small ultrasonic pulse that propagates and is reflected from deformed surface of rubber; the echo pulse is

received by receiver. Therefore, by measuring the change in transmitted and received time of pulse, it is possible to measure thickness variations of rubber and the applied force, as a consequence. Contact parameters can be detected also by measuring the change in resonance frequency of sensor, in accordance with contact object's acoustic impedance. With this approach, hardness and/or softness of objects can be easily detected [21-23]. Ultrasonic-based tactile sensors have fast dynamic response and good force resolution. However, many of such sensors use materials like lead zirconate titanate (PZT), which are difficult to process, especially with standard micromachining technologies and processes.

1.3.2. METHODS FOR TACTILE SENSING: DIRECT ELECTROMECHANICAL TRANSDUCTION

The most common tactile transducers based on coupled electromechanical method rely on capacitive, piezoresistive and piezoelectric transduction techniques. These sensing systems are often referred as transducers of contact information [13, 14, 24, 25].

Piezoresistive transduction methods exploit resistance variations in sensing material to detect and measure contact forces. Piezoresistive transducers can be grouped in conductor-based and semiconductor-based strain gauge transducers.

In piezoresisitive strain gauge sensors, the changes in resistance are typically due to the deformation of conductor or semiconductor – the material strain – under external mechanical stress. The working principle of a strain gauge is explained by the Hooke's low, where the mechanical stress, generated by force acting on object, is directly proportional to strain, defined as the ratio of object deformation and its length. Focusing on the voltage/current characteristic, the change in resistance is observed by a change in current (or voltage, respectively). Typically, the strain gauges are long winding snake-like structures whose cross-section decreases while the conduction length increases under external stimulus. The technology of strain gauges sensors is mature, well established and simple and they have a wide measuring range [26-30]. They have many advantages and drawbacks. They exhibit good sensitivity, high signal-to-noise ratio and sufficient robustness to electro-magnetic noises. The detection accuracy is generally on mN level. They are relatively simple to manufacture and, therefore, they have very low cost. However, they show high susceptibility to humidity and temperature variations and a Wheatstone bridge configuration is required to overcome this problem. Due to their mechanical nature, they express high hysteresis and a non-linear response. Silicon and other semiconductor materials have high piezoresistive responses but they are brittle and fragile [31, 32]. To achieve mechanical flexibility, resistive elements have often the form of conductive rubber, elastomer or organic transistors [33-39]. The sensitivity typically decreases because of tearing off, since the resistance of conductive materials

depends on deformation as well as on its thickness. Furthermore, variations of temperature and moistness may affect and change the properties of conductive elastomer and rubber materials. Finally, piezoresistors suffer from lower repeatability since multiple deformations may prevent the elastic materials to regain their initial form.

Capacitive sensors consist of two conductive plates, separated by a compressible dielectric material (typically the air). They are able to measure applied forces by the variation of capacitance due to the changes in the gap between plates. Besides normal forces, shear forces can be measured with the use of embedded multiple capacitors. Capacitance-to-frequency converters, switched-capacitors circuits or capacitive ac-bridges are usually utilized to detect the capacitive output and convert it in an electrical signal [40-45]. Capacitive technology is very popular among sensing transducers and capacitive sensors are widely utilized in robotic application, especially. These sensors generally exhibit good frequency response, high spatial resolution and large dynamic range. They have low power consumption and are poor sensitive to the changes of environment as temperature and humidity. They are robust and have drift-free measurement capabilities. However, capacitive sensors are quite susceptible and sensitive to noise, field interactions and fringing capacitance and the electronics required to filter out the noise is often relatively complex.

Among these approaches, piezoelectricity has been recognized as a really promising and attractive technology. Piezoelectric force sensors exploit piezoelectric effect that consists of an electrical charge generation, and a voltage potential as a consequence, in some crystalline material, like quartz crystal or ceramics, and polymers due to deformation or strain caused by applied force/pressure. Generated voltage is directly proportional to the force/pressure/strain [46-48]. Sensors based on piezoelectric effect exhibit high frequency response, that is a fundamental parameter for measuring vibrations, high bandwidth, high efficiency, excellent resistance, flexibility, high mechanical strength, good plasticity, high power density, impact resistance and anti-aging. They are very attractive because of their poor or no power consumption and, in same case, low thermal budgets for materials deposition, high integration with standard micromachining techniques, depending on the utilized material and, especially, very low cost. Nevertheless, they are limited to measure dynamic forces and are unable to measure static forces because the charge developed decays with a time constant which depends on the internal impedance and the dielectric constant of piezoelectric film.

CHAPTER II

Contents

Summary

In this chapter the theoretical and qualitative formulation of the piezoelectricity is discussed. The high-order flexoelectric effect is then described, providing a qualitative description of the phenomenon as additional contribution to the well-known piezoelectric effect. A detailed analysis of piezoelectric pressure/force transducers carried out from the recent state of the art is presented, discussing also some examples of interaction between piezoelectricity and flexoelectricity.

The device concept of proposed pressure/force sensor based on piezoelectric/flexoelectric transduction mechanism and the corresponding architecture are finally presented.

ARTIFICIAL TRANSDUCERS DESIGN

In Chapter I, an overview of force/pressure MEMS sensors and corresponding transduction mechanisms was given shortly. Piezoresistivity, capacitive transduction and piezoelectricity are the most commonly used technologies in the implementation of such devices. Among them, piezoelectricity has been recognized as a really promising and attractive technology in both sensing and actuation applications. The use of active and functional materials for mechatronic systems – like piezoelectrics – stands out in the field of high potential smart materials for MEMS and microstructures with new and powerful functionalities.

This chapter provides a brief overview of piezoelectric working principle, physical properties and constitutive models. Thereafter, a review of MEMS force/pressure sensors for tactile sensing application based on piezoelectric transduction mechanism is given.

2.1. TRANSDUCTION PRINCIPLE: PIEZOELECTRICITY

Piezoelectricity refers to a phenomenon of linear electromechanical interaction in particular class of noncentrosymmetric crystals that demonstrate a coupling between their electrical and mechanical states generated by applying mechanical stress to dielectric crystals. Piezoelectrics are dielectric materials which can be polarized, in addition to an electric field, also by the application of mechanical stresses. In Figure 2.1, the electromechanical relationships chart of quantities involved in piezoelectricity is depicted.

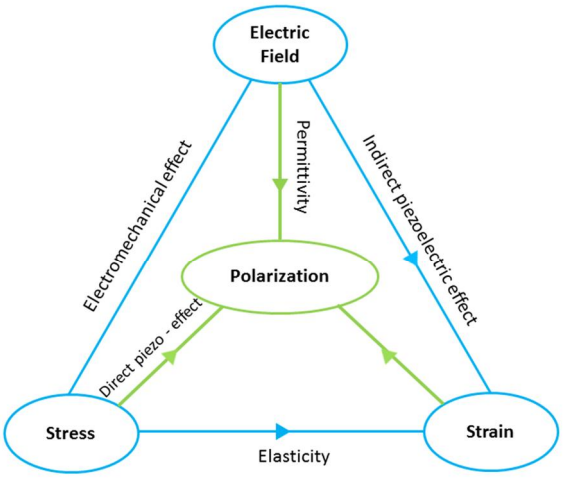

Figure 2.1 Chart of electric and elastic phenomena involved in piezoelectricity (adapted from [49]).

Piezoelectric materials can be classified into polar (which possess a net dipole moment) and nonpolar piezoelectric materials (whose dipolar moments, summed in different directions, give a null total moment).

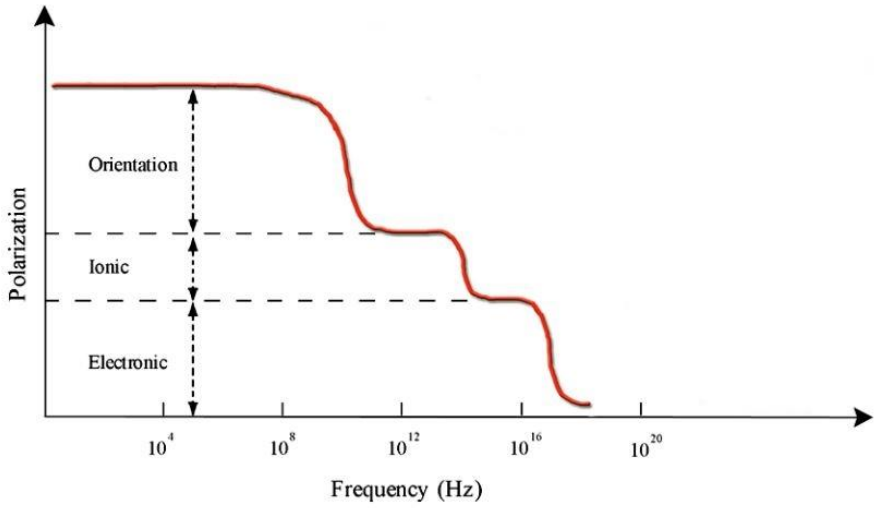

Figure 2.2 Frequency dependence of electronic, ionic and orientation polarization mechanisms (adapted from [49]).

The response of piezoelectric materials to externally applied electric field is crucial to piezoelectricity. When a solid is placed in an externally applied electric field, the medium adapts to this perturbation by dynamically changing the positions of the nuclei and electrons. As a result, an alignment of already existing permanent or induced atomic/molecular dipoles is achieved. This process is called polarization. There are three main types or sources of polarization: electronic, ionic, and dipolar or due to orientation. The degree to which each mechanism contributes to the overall polarization of the material depends on the frequency of applied field, as shown in Figure 2.2.

When piezoelectric materials are subjected to an external electric field, an asymmetric displacement of anions and cations causes a significant net deformation of the crystal lattice. The resulting strain is directly proportional to the applied electric field. The strain can be either extensive or compressive, depending on the polarity of applied field. This effect is generally called indirect piezoelectric effect. Vice versa, when piezoelectric materials are subjected to external strain by applying pressure/stress, the electric dipoles in the crystal get aligned and the crystal develops positive and negative charges on opposite faces, resulting in an electric field across it. This effect is called direct piezoelectric effect [50-52].

In order to better explain piezoelectricity phenomenon, the crystal structure of piezoelectric solids and the symmetry of crystal lattice must be taken into account. Piezoelectricity is determined by the balance between two contributions: positive and negative ions. The condition for the occurrence of piezoelectric effect is a lack of symmetry center regarding positive and negative ions of crystal lattice. That is to say, the existence of polar axes within the crystal structure and the presence of an electrical dipole moment in axis directions caused by the distribution of electrical charge in the chemical bond are essential. The atoms of crystal lattice share a given electronic density through the bonds between them. If the electronic density is spatially non-uniform, a

periodic arrangement of local electric dipoles will be present in the crystal, although the sum of all the individual dipoles at a given moment should be zero because of their instantaneous random orientation.

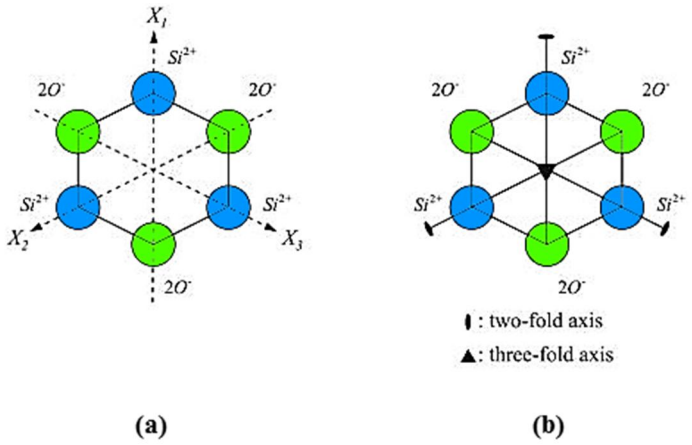

Figure 2.3: Simplified structure cell of α-quartz: a) arrangement of Si- and O-ions with the main crystal axes and b) two- and three-fold axes (adapted from [53]).

In Figure 2.3, an example of the classic structure cell of *α*–quartz is considered. The structure consists of negative charged *O*-ions and positive charged *Si*-ions and has three two-fold polar rotation axes X_1, X_2 and X_3 in the drawing plane and a three-fold rotation axis *Z* perpendicular to the drawing plane. In such a way, the crystal is electrically neutral. When a mechanical stress is applied to the solid, the elastic strain generated in the crystal creates changes in the length and/or direction of the individual atomic bonds. This leads to changes either in magnitude and/or in the direction of dipoles present in the crystal and, therefore, a resulting net polarization of the lattice [53].

The electrical polarization is caused by the displacement of positive and negative ions of the crystal lattice against each other (as depicted in Fig. 2.4a) resulting in an electrical charge on the appropriate crystal surfaces perpendicular to the X_1-axis and thus in an outside electrical polarization voltage. This effect is called direct longitudinal piezoelectric effect. An exposure to compression and tensile stresses acting perpendicularly to the X_1-axis results in an additional electrical polarization with opposite sign in X_1-axis direction (see Fig. 2.4b). This behavior is called direct transversal piezoelectric effect. This leads to the origin of direct piezoelectric effect and its presence or absence in a given crystal is determined by the symmetry of lattice. So, not all materials can be piezoelectric. In crystals, symmetry properties are crucial in determining if and how a material is piezoelectric. For example, a crystal which possesses inversion symmetry (centrosymmetric) cannot be piezoelectric because in this case its polarization, which must change sign when the axes are inverted, should be necessarily zero.

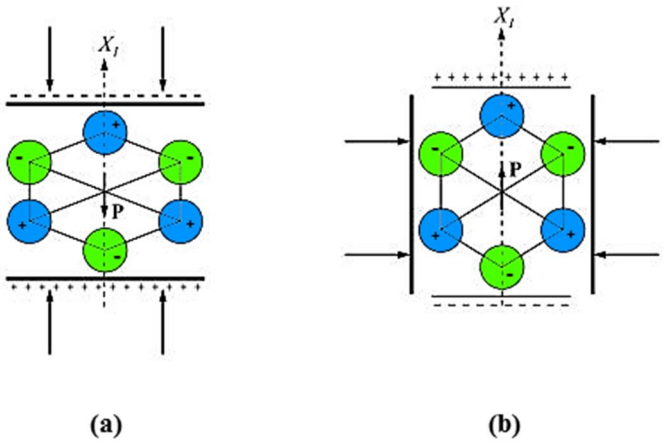

Figure 2.4: a) Direct longitudinal piezoelectric effect and b) direct transversal piezoelectric effect (adapted from [53]).

The basic behavior of piezoelectric materials is shown in Figure 2.5 which depicts the piezoelectric effect in both direct and indirect configurations, respectively. The poling process sets the mechanical and electrical axes of operation and induces piezoelectric properties in the piezoelectric material (Fig. 2.5a). So, when a compressive load is applied to a poled piezoelectric material in direction parallel to poling (see Fig. 2.5b), a positive voltage is generated across the faces because of coupling between electrical and mechanical field.

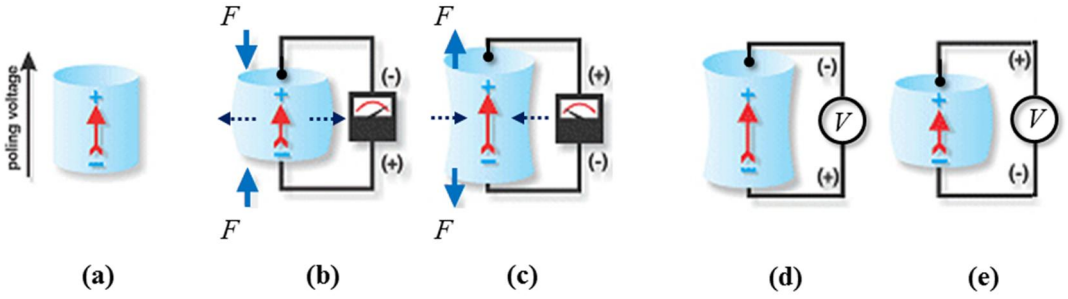

Figure 2.5: a) Polarization process**;** (b-c) direct and (d-e) indirect effect of piezoelectric material showing voltage generation when compressed and shape changes when voltage is applied (adapted from https://www.americanpiezo.com/).

Similarly, when the material is subjected to tensile force, a voltage with reverse polarity is generated (see Fig. 2.5c). This is the direct piezoelectric effect. On the contrary, when an external voltage is applied to the material, it gets extended if the polarity of the voltage is the same as that of the field applied during poling (Fig. 2.5d) and, when the voltage is applied in the reverse direction, the material gets compressed (Fig. 2.5e), according to the indirect piezoelectric effect.

2.2. FLEXOELECTRICITY: A SYNERGISTIC HIGHER-ORDER ELECTROMECHANICAL EFFECT

Some dielectric solids exhibit a linear relationship between the spontaneous electrical polarization and the gradient of mechanical strain. This phenomenon is known as *flexoelectric effect*. The name originates from the Latin word *flexus* that means *'bend'* and it has been adopted pointing out the fact that a strain gradient naturally arises in bent structures. Thus, if the piezoelectric effect is a linear response of the dielectric polarization to a mechanical uniform strain, the flexoelectric effect can be thought as a high-order electromechanical phenomenon that can combine with the piezoelectricity in a synergistic way. The different methods of generation of the two phenomena typically render the flexoelectric effect less significant compared to piezoelectric one at macroscopic scale, especially in structures where mechanical limitations reduce the formation of a large strain gradient.

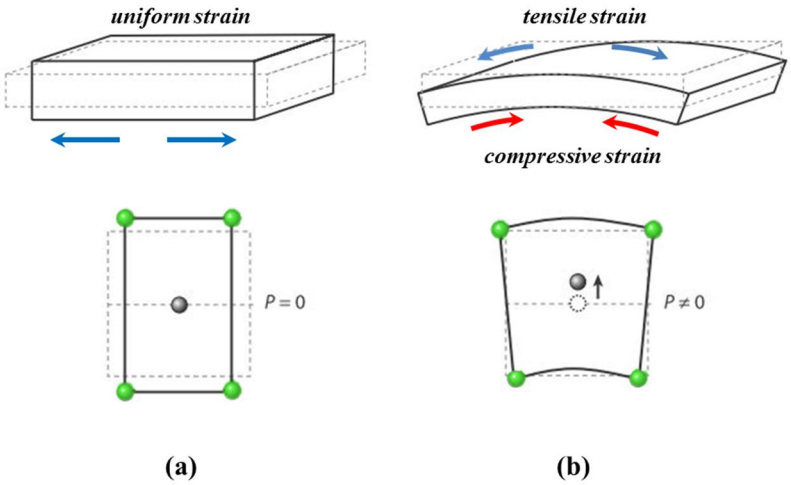

Figure 2.6: (a) Uniform strain, due to uniaxial compression does not break inversion symmetry and hence cannot generate polarization in a centrosymmetric material. (b) Non-zero strain gradient generated by compressive (red arrows) and tensile (blue arrows) strains leads to a flexoelectric-induced polarization *P*. A non-zero dipole moment results from a misalignment of the centers of gravities of the positive and negative ions (adapted from [54]).

The existence of the flexoelectric effect in solids was predicted in liquid crystals starting from the 1960s [55] as a type of piezoelectric effect that differs in the way that it is caused by the spatial derivative of strain. The coupling between polarization and strain gradient exists also in hard materials and can be found in any crystalline material regardless of the atomic bonding configuration, emerging even in centrosymmetric lattices. Moreover, an important feature of the flexoelectricity is that it becomes relatively most significant in materials which possess geometries

in which large strain gradients are achievable. From a microscopic point of view, flexoelectricity is originated by the non-uniform displacement of ions under a strain gradient, which disrupts the inversion symmetry, leading to the formation of a net polarization inside the crystal (see Figure 2.6). When a free-standing slab of material is bent such that the upper and lower part of the slab experiences tensile and compressive strain (Figure 2.6b), respectively, a strain gradient arises in the material, which in turn induces an electrical polarization *P* parallel to the gradient direction. As shown in Figure 2.6b, the non-zero strain gradient in the bent crystal makes the centers of gravity of the negative ions (in green) and the positive ions (in gray) to be not coincident, which results in a non-zero net dipole moment in the directions of the gradient-induced polarization.

According to the macroscopic theoretical formulation previously mentioned, the strain gradient (via the flexoelectric coupling) plays a key role in the generation of the flexoelectric phenomenon: it can work as an electric field, inducing poling, switching, and rotation of polarization, creating a voltage offset of hysteresis loops and smearing the dielectric anomaly at ferroelectric phase transitions.

Even in piezoelectric materials, flexoelectric effects can be exploited by promoting large flexoelectric contributions in order to enhance the properties of materials or even to enable new classes of electromechanically coupled materials of non-uniform shapes. They exhibit large strain gradients such that flexoelectricity can be used to tune electricity generation.

2.3. BIOINSPIRED PIEZOELECTRIC TACTILE SENSORS: STATE OF ART

One of the greatest challenges of bio-inspired technologies in mimicking tactile sensors is the application of flexible active materials in the transducer devices to convert the mechanical pressure or stress into a usable electric signal (voltage and/or current). In the emerging field of soft machines, soft active materials (SAM), able of large deformation, can connect the stimuli to this functionality.

In the recent past, Tiwana et al have summarized the state of art designs and fabrication methods of piezoelectric-based sensors, showing evolutions and trends [56]. More recently, P. Saccomandi et al, Z. Kappassov et al and Y. Wei and Q. Xu have outlined new possible directions of research in dexterous in-hand manipulation [13, 25, 57]. According to these research works, in piezoelectric force/pressure sensors the active material is crucial for the transduction efficiency of the final devices.

Among the available piezoelectric materials, one of the most investigated and widely used is lead zirconate titanate (PZT), the ferroelectric material with the highest piezoelectric coefficient. A way to measure the pressure by active piezo-ceramics like PZT is to use resonant sensors. Based

on the principle of change in piezoelectric resonance frequency with the applied pressure, an example of resonant sensors have been designed and proposed by G. M. Krishna and K. Rajanna [58]. Circularly shaped poled 1 mm-thick PZT substrate has been used to realize the tactile sensor with a resonance frequency of ~1 MHz. An array of electrodes has been deposited on either side of the PZT material. The common areas of PZT material sandwiched between the intersecting rejoins of the electrodes form the matrix of independently excitable resonators at the resonance frequency of the material. Tactile sensors with 3x3, 7x7 and 15x15 array of electrodes have been developed with different electrode dimensions and separation pitch in between. They have showed improved spatial resolution and sensitivity to different extents of applied force/pressure as well as a variation in frequency of 0 – 25kHz from the resonance frequency in a range of applied forces of 5 – 55 N. D. Belavic et al [59] have developed a resonant pressure sensor based on PZT that consists of 16 thick-film elements with lateral dimensions 4.7 x 4.7 mm^2 and a thickness between 50 and 60 µm. The final sensor exhibits response to mechanical deformation in both static and dynamic pressure range from 0 to 70 kPa. A shift around resonance frequency (26 kHz) has been measured, with pressure sensitivity about 2.6 Hz/kPa.

After the discovery of a strong piezoelectricity in polyvinylidene fluoride (PVDF) polymers and copolymers (like poly[(vinylidenefluoride-co-trifluoroethylene] P(VDF–TrFE)) – that exhibit a voltage output response 10 times higher than piezo-ceramics for the same input force and high electromechanical transduction frequency bandwidth (up to 1 kHz) – an increasing interest in such a crystalline ferroelectric polar polymers has encouraged researchers to study the capabilities of these materials in sensing application. R. S. Dahiya et al have experimented tactile sensing chips using CMOS technology [60, 61]. The sensor consists of an active area of 0.9 mm x 0.6 mm, to obtain spatial acuity comparable to that of human fingertips (~1.0 mm). Based on POSFET working principle, it utilizes the contact induced change in the polarization level of piezoelectric (PVDF–TrFE) polymer (and hence the changes in induced channel current of MOS) to detect dynamic contact forces in the range of 0.01 – 3 N. The response of POSFET is linear in the tested range, with sensitivity of 102.4 mV/N. The drawback is the presence of silicon substrate that doesn't make this sensor particularly suitable to adapt to curved surfaces. Still based on PVDF thin film, M. A. Qasaimeh et al have developed a miniaturized tactile sensor capable of measuring force and force position for minimally invasive surgery applications [62]. The sensor has been designed such that it can sense low forces comparable to those produced by pulsating delicate arteries as well as can withstand high forces comparable to grasping forces. A 25-µm-thick double-sided metalized and pre-poled piezoelectric PVDF film, working in the extensional mode, has been sandwiched between supports of the silicon plate and plexiglas layer. When, due to a compressive load, the silicon plate deflects, the glued PVDF is also stretched and a voltage signal is registered. The PVDF sensing element is sensitive in a range of 0.001 – 6 N, when point loads are applied at the center of the element.

A 3D tactile sensing element concept, based on three-dimensional piezoelectric aluminum nitride (AlN) membranes, has been analyzed by T. Polster and M. Hoffmann, who have provided a combination of AlN thin films as smart sensing material with 3D membrane elements in order to realize tactile sensors with sensitivity towards normal to shear forces [63]. Aluminum nitride (AlN) is suitable for sensor applications, because of its relatively good piezoelectricity, exhibited by its c-axis oriented polycrystalline columnar structure. Since its oxidation processes occur only from about 800 °C, it is also suitable for high temperature applications. It does not need to be electrically poled, differently from ferroelectric materials like PZT. It shows high thermal conductivity (200 W/mK), low dielectric constant (~9), high electrical resistivity and high temperature stability (up to 1500°C).

Previous examples of pressure/force sensors are affected by the rigidity of the sensing element and substrate, whereas flexibility and stretchability are mandatory to realize an artificial skin. H.-J. Tseng et al have proposed tactile sensors using sol-gel process to deposit PZT thin-film (from 250 nm to 1 μm thickness) on a flexible stainless steel substrate with high sensitivity about 0.798×10^{-3} V/mN to measure human pulses [64].

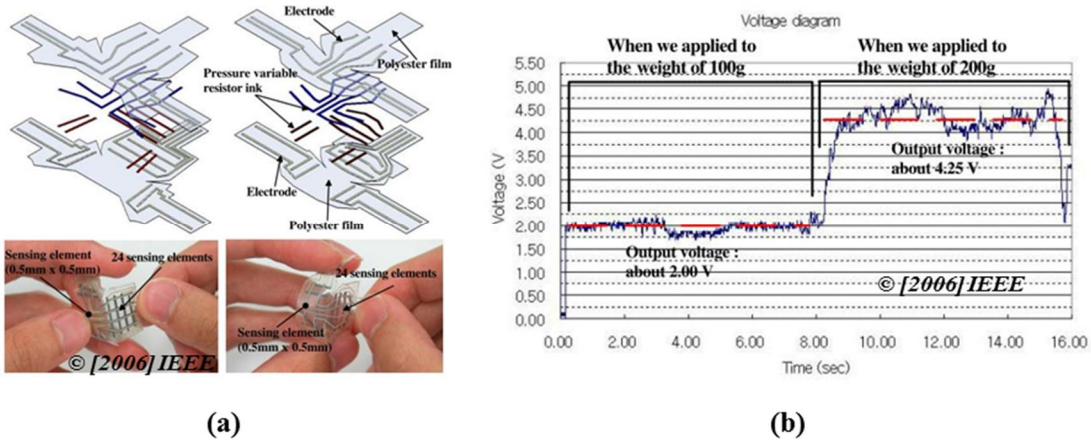

Figure 2.7: B. Choi et al a) fingertip force sensor and b) output voltage diagram when forces of 1 N and 2 N are applied (adapted from [66]).

B. P. Nabar et al [65] have developed a sensing skin for robots made of large area arrays of ordered, vertically aligned, crystalline zinc oxide (ZnO) piezoelectric nanorods on flexible substrates to ensure conformity to non-planar surfaces. Dimensions of a single nanorod array vary from 500 μm x 500 μm (in a single array) to 30 μm x 30 μm (series connected). The sensors array is designed to measure tactile normal pressure in 10 kPa – 200 kPa ranges with 1 mm spatial resolution. A voltage signal in the range of few mV is observed in response to applied pressure.

An anthropomorphic robot hand has been fabricated by B. Choi et al [66]. The hand has a miniaturized fingertip tactile sensor (Figure 2.7) based on (PVDF) film which makes it physically

flexible enough to be deformed into any three-dimensional geometry. The fingertip tactile sensor shows a voltage signal in the order of few volts when a force of 1 to 2 N is applied.

Large area flexible and conformable robotic skin, made of arrays of (PVDF) piezoelectric polymer taxels integrated on flexible PCBs (as displayed in Figure 2.8) has been manufactured by L. Seminara et al. Preliminary results show the linearity and reproducibility of the system response to applied mechanical stimuli from few mN up to 3 N [67, 68].

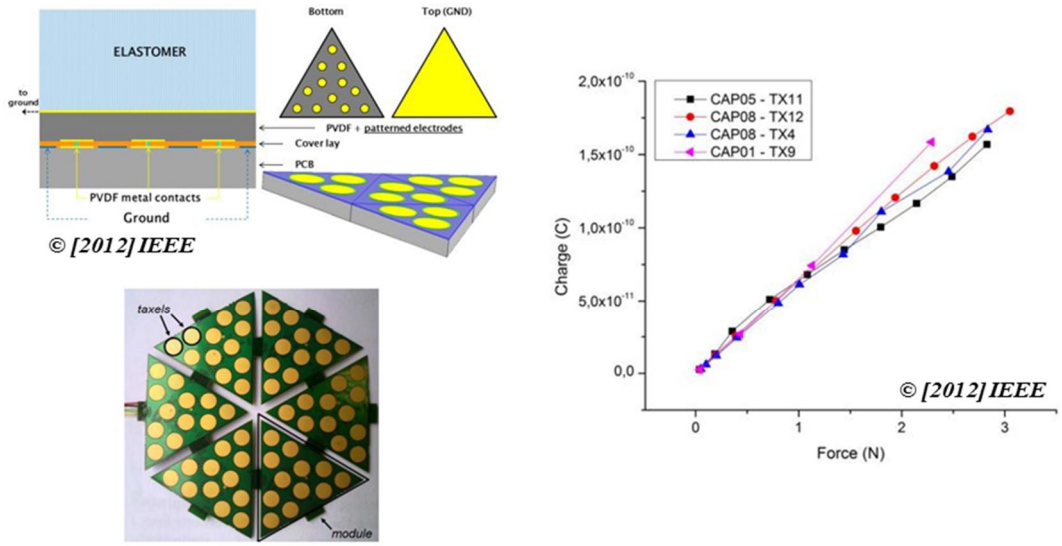

(a) **(b)**

Figure 2.8: Large area robotic skin by L. Seminara et al. a) from top: section of skin module (on left) and (on the right) the PCB substrate containing the PVDF sensors (yellow). Hexagonal patch made up of six triangular PCBs (on bottom); b) charge generated by different PVDF taxels vs applied input force (at a frequency of 6Hz) (adapted from [68]).

A novel flexible tactile piezoelectric sensor, integrated with piezoresistive transducers, has been developed by C. H. Chuang et al [69] for detecting incidents of slippage and contact forces, respectively. The sensor structure is composed of two patterned flexible printed circuits (FPC) sandwiching a (PVDF) film, a foil strain gauge laminated on the bottom FPC, a bump-like structure attached on the top FPC corresponding to the (PVDF) area and the PDMS packaging material. According to experimental results, the sensor can detect contact forces from 0.1 N to 20 N with two-stage linear behavior. The sensitivities of the contact forces are 0.03 mV/N and 0.0057 mV/N for the force ranges of 0.1 – 4 N and 5 – 20 N, respectively.

An improved sensitivity response of aluminum nitride diaphragms used to measure pressure, together with high flexibility, has been proved by M. Akiyama et al [46, 70, 71]. The authors have investigated high sensitive piezoelectric response of c-axis oriented AlN thin films prepared on polyethylene terephthalate (PET) and polyimide films, exploiting the combination of high and low modulus of these materials, respectively. The sensor consisting of the AlN and polymer films is flexible like polymer films and the electrical charge is linearly proportional to the

stress within a range from 0 to 8.5 MPa. The sensor can respond to frequencies from 0.3 to over 100 Hz and has been used to measure human pulse wave form.

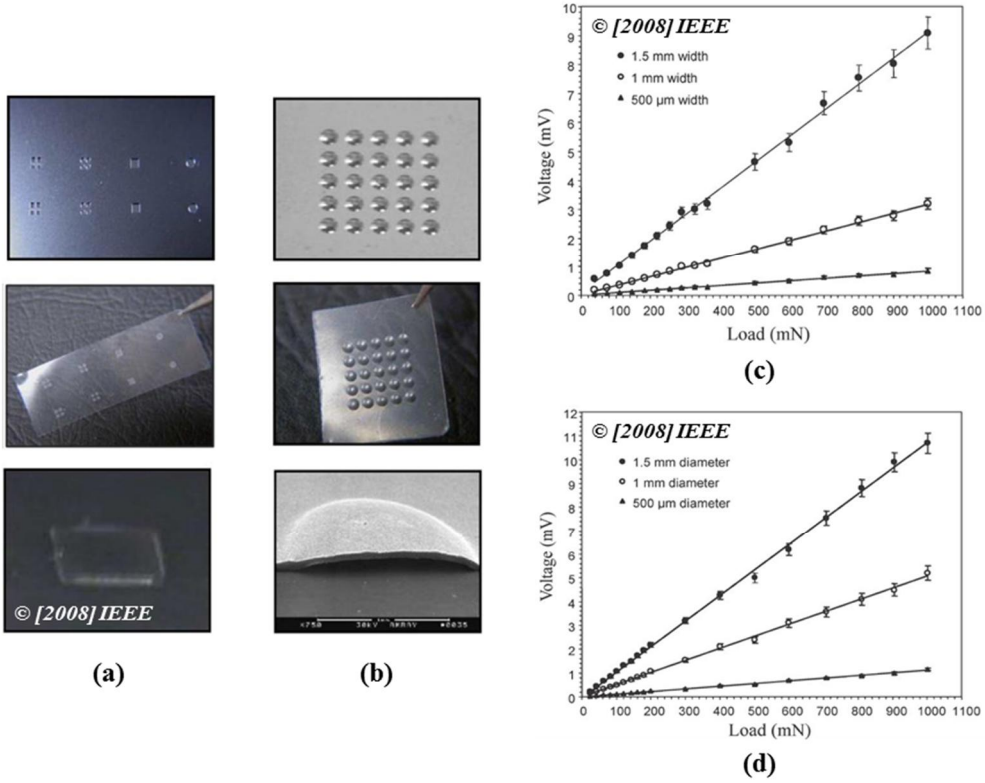

Figure 2.9: Microphotographs of (a) bump shape with enlarged view of the bump (height = 30 μm) and (b) dome shape with a SEM picture of the cross section of the dome (thickness = 30 μm); c) measured peak-to-peak voltage versus added loads for the bump shape and d) dome shape sensors (adapted from [73]).

However, piezoelectric thin-films based on the (d_{33}) mode tend to have only a limited region within which they are capable of generating voltage signal. As demonstrated by C. H. Feng et al [72], current study have addressed attention to development of piezoelectric dome-shaped-diaphragm transducer (DSDT) as three-dimensional structures whose surface area is larger than that of planar devices with the same footprint. As a result, for a given vibration energy input, DSDTs are able of producing greater electrical charge than their planar counterparts. Several examples of such a three-dimensional DSDT can be found in literature. C. Li et al have developed an innovative dome and bump shape element as a sensing component for flexible tactile sensors. The sensor (see Figure 2.9) is made of 30 μm-thick (PVDF-TrFE) film, whereas the dome shape and the square bump shape microstructures have the diameters and widths of 500 μm, 1 mm, and 1,5 mm, respectively [73]. The tactile sensors, developed using these polymer microstructures, can measure as small as 40 mN forces for bump shape sensors (with sensitivities of 0.81, 3.23 and 9.1 mV/N for the bump areas of 0.25, 1, and 2.25 mm^2, respectively) and a force increment of 25 mN

for dome shape sensors (the achieved sensitivities is 1.1, 5.07, and 10.6 mV/N for the different diameters of 500 µm, 1 mm, and 1.5 mm, respectively).

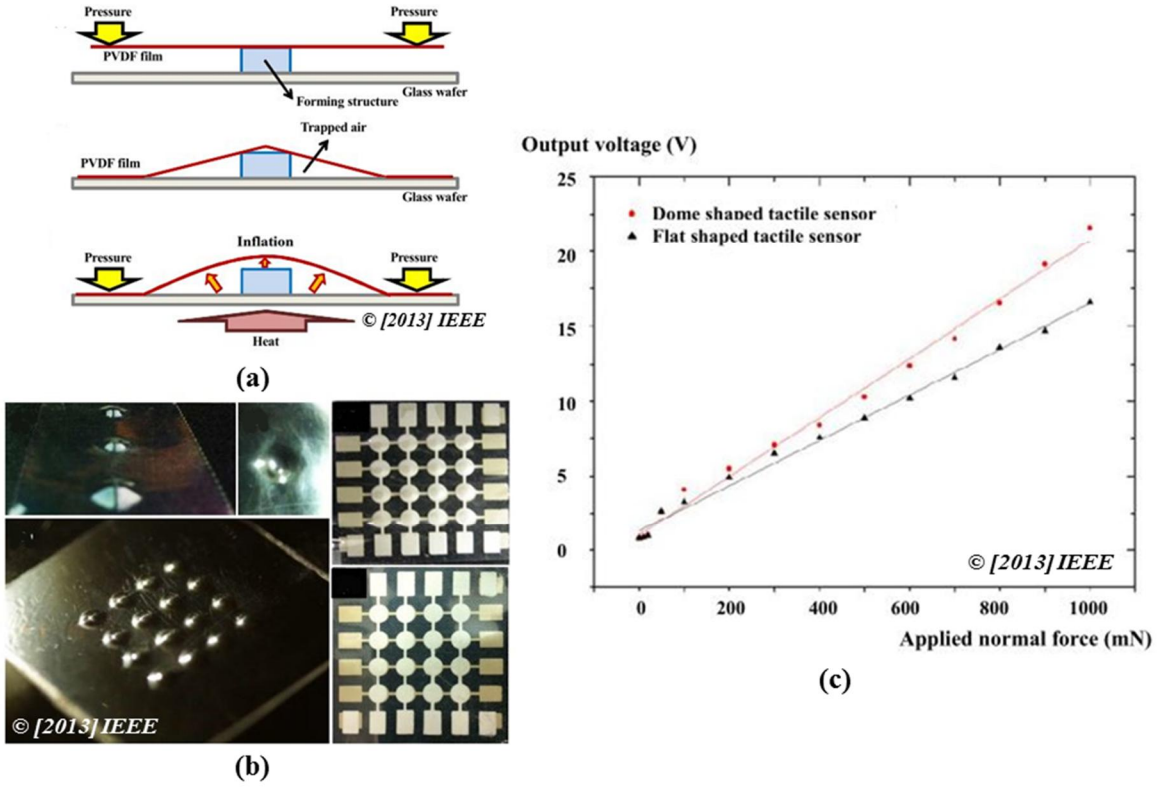

Figure 2.10: a) The process of controlled inflation technique; b) optical photographs of the fabricated dome shape tactile sensors; c) detection of contact force with proposed dome shape tactile sensor and flat shape tactile sensor (Frequency: 5Hz) (adapted from [74]).

Dome-shaped piezoelectric tactile sensors made of 56 µm-thick PVDF and fabricated by inflation technique (see Figure 2.10) have been proposed by M. S. Kim et al [74, 75]. The proposed devices are able to measure forces in a range of few mN up to 1 N. In this force range, the achieved sensitivities are 7.89 mV/mN and 8.83 mV/mN for two dome-shaped sensors (with height h = 0.5 mm and 1.0 mm, respectively). A comparison of the sensitivities of these two sensors with a flat tactile structure (S = 6.02 mV/mN) shows that dome-shaped tactile sensors have higher sensitivity of about 46.4% than the conventional flat tactile sensor.

Table II.2 summarizes the main features of previously mentioned sensors, taking into account materials properties, pressure/force range and flexibility requirements.

Table II.2

Summary of main features of tactile sensors according to materials properties, pressure/force range and flexibility requirements

Authors	Material	Method	Dimension [mm^2]	Thickness [µm]	Flexibility	Operation range	Sensitivity
G. M. Krishna [58]	PZT	Resonant sensor (1 MHz)	176	1000	✗	5-54N	/
D. Belavic [59]	PZT	Resonant sensor (26 kHz)	22	16	✗	0-70kPa	2.6 Hz/kPa
R. S. Dahiya [60, 61]	PVDF-TrFE	POSFET	0.54	2,5	✗	0.01-3N	102.4 mV/N
M. A. Qasaimeh [62]	PVDF	Extensional mode	4	25	✗	0.001-6N	/
H. J. Tseng [64]	PZT	Extensional mode	36	0.250 – 1	✓	Human pulse	0.798 mV/mN
B. P. Nabar [65]	ZnO nanorods	Extensional mode	0.25 0.001	5	✓	10-20kPa	/
C. H. Chuang [69]	PVDF/ Piezo-resistors	Extensional mode	225	28	✓	0.1-4N 5-20N	0.03 mV/N 0.0057 mV/N
M. Akiyama [46, 70, 71]	AlN	Extensional mode	/	1	✓	0-8.5MPa	0.9 kPa
C. Li [73]	PVDF-TrFE	DSDT	0.19 up to 1.76 0.25 up to 2.25	30	✓	0-1N	0.81 to 9.1 mV/N 1.1 to 10.6 mV/N
M. S. Kim [74, 75]	PVDF	DSDT	3.14	56	✓	0-1N	/

2.3.1. ADDITIONAL FLEXOELECTRIC CONTRIBUTION

Though the existence of the flexoelectric effect in solids has been predicted in the past, this phenomenon has drawn limited attention up to the end of the century, especially because of the difficulties in measuring quantitatively its contribution – that, moreover, is expected to be weak. Furthermore, the available theoretical and experimental results are rather contradictory, attesting to a limited understanding of this electromechanical effect. Poor examples of force/pressure and tactile applications exploiting flexoelectric effect can be found in literature so far.

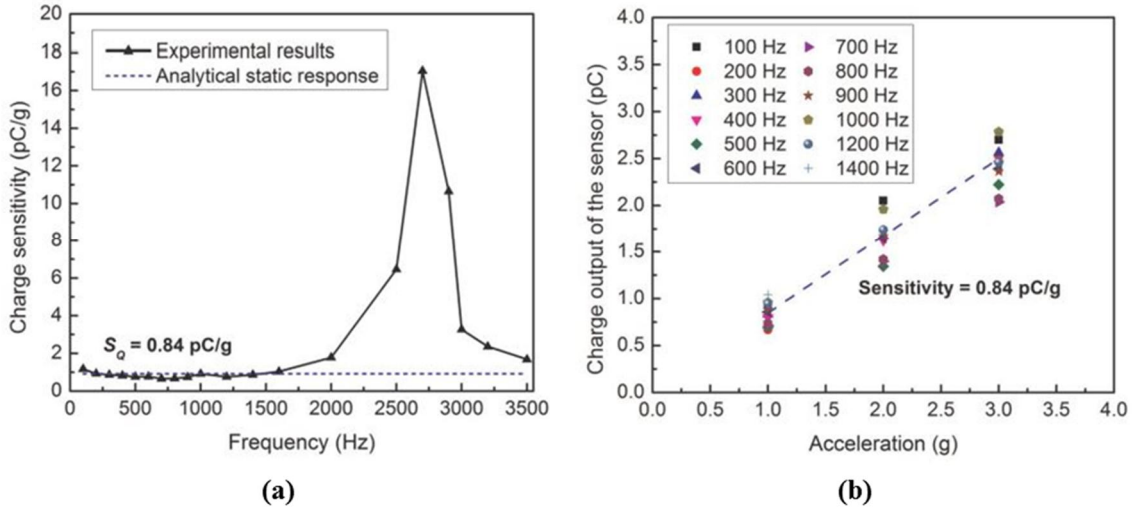

Figure 2.11: a) Comparison of measured frequency response with the analytical solution; c) sensor charge output under different frequencies and acceleration ranges (adapted from [76]).

Nevertheless, the flexoelectric effect looks promising for practical applications, especially in electromechanical sensing. Flexoelectricity suggests an alternative approach toward high performance electromechanical sensors due to the greatly enhanced effective piezoelectricity of miniaturized flexoelectric structures [77]. W. Huang et al [76] have designed a new acceleration sensor using flexoelectric barium strontium titanate ($Ba_{0.65}Sr_{0.3}5TiO_3$ or BST) cantilever for vibration monitoring. Experimental results reveal the prototyped accelerometer, with thickness of 0.1 mm and length and width in millimeters, have a stable sensitivity of 0.84 pC/g in a low frequency range (100 Hz – 1.6 kHz). They have also demonstrated the charge output of the sensor is in the range of 0.5 – 3 pC under different frequencies and acceleration ranges, as shown in Figure 2.11.

A flexoelectric bridge-structured microphone using still bulk BST ceramic has been investigated in the study of S. R. Kwon et al [78] to detect sound pressure emitted from a loud speaker. The 1.5 mm×768 μm×50 μm micro-machined bridge-structured flexoelectric microphone has been designed to show a sensitivity of 0.92 pC/Pa, while its calculated resonance frequency is 98.67 kHz. The flexoelectric microphone has both high sensitivity and broad bandwidth, indicating that flexoelectric microphones are potential candidates for applications in acoustic sensor.

One of the most promising application of flexoelectricity concerns the performance enhancement of some piezoelectric micro- and nano-systems. As reported by S. Petroni et al [79], the strain gradient and the resulting flexoelectric effect in non-ferroelectric aluminum nitride are responsible for an additional polarization, leading to an enhancement of the transduction properties of the used material. Parallel plate capacitors, made of AlN and realized for tactile sensing purpose with a dome shape, present high elasticity under applied stress and sensitivity in the pressure range of 10 kPa to 1 MPa. The static contribution due to the flexoelectric polarization has been

experimentally observed as a capacitance variation ΔC when a load is applied over the dome. The capacitance variation is measured as a function of the pressure, applying loads from ~0.01 N to 0.2 N, and a shift within ±0.04 pF has been measured.

2.4. CHOICE OF PIEZOELECTRIC MATERIAL FOR TACTILE SENSING PURPOSES

As reported in previous paragraph, there is a wide choice of materials and material forms (ceramics: PZT; polycrystalline films: ZnO, AlN; polymers and copolymers: PVDF, PVDF-TrFe) that are actively piezoelectric. In the early stages of MEMS development, piezoelectric materials were rarely used and mostly restricted to ZnO, as it was hard to access deposition techniques that would guarantee repeatable results and fabrication process compatibility. Furthermore, the most common used piezoelectric material was lead zirconate titanate for long time, especially for macroscale application. As MEMS systems move to smaller sizes and increased integration density with increased speed, larger range of motion and more powerful actuating elements, revolutionary advances in actuators, sensors and transducers are required. These advances are enabled by the rapidly growing field of thin-film piezoelectric MEMS. Fabrication process compatibility, complexity and limited availability of repeatable and reliable piezoelectric thin films have limited the incorporation of piezoelectric material like ZnO and PZT as thin films. One of the most important drawback of ZnO and PZT concerns to IC fabrication facilities because of contamination risks in complementary metal oxide semiconductor (CMOS) lines.

Typically, the most common used piezoelectric thin films possess a number of key characteristics that make them very attractive:

- excellent temperature and frequency stability (this is achievable by the deposition of wurtzite-structured films);
- piezoelectric charges develop whenever the device undergoes mechanical excitation. Thus, piezoelectric sensors do not require power themselves (although any associated electronics such as charge or voltage amplifiers, etc., will need to be powered). As a result, piezoelectric MEMS are interesting for low power, low noise and broad dynamic ranges requirement sensors;
- piezoelectric actuators have substantially high energy densities. As example for actuators, the force per unit area increases linearly with the electric field. Moreover, the permittivity of piezoelectric thin films exceeds that of air. As a result, the required driving voltages to achieve a given displacement in these structures is typically modest;

- piezoelectric thin films show good scaling with size. That is to say, the energy density available for actuation remains high, even as device sizes drop, so that useful work can be done even with small volume structures. This decreases the complexity, enables higher integration density and reduces the voltage load on IC electronics.

A comparison of main properties and features of thin-film piezoelectric materials used in MEMS technology is listed in Table II.3 below.

Table II.3

Material properties of common MEMS piezoelectrics.

Parameter	**PZT**	**ZnO**	**AlN**	**β-PVDF**
System class	Hexagonal 6mm	Hexagonal 6mm	Hexagonal 6mm	Orthorhombic mm2
Lattice constants [Å]	a = 5.78 c = 7.10	a = 3.28 c = 5.23	a = 3.11 c = 4.98	a = 8.45 b = 4.88 c = 2.55
Density [kg/m^3]	7600	5606	3255	1800
Young's modulus [GPa]	63 - 68	120 – 201	308 – 348	2 – 3
Poisson ratio	0.35	0.33	0.30	0.34
Piezoelectric constant				
d_{31} [pC/N]	-40 – -94	-2 – -7.5	-1.9	-18 – -20
d_{33} [pC/N]	90 – 290	5.5 – 12.4	4.9	15 – 16
g_{31} [V·m/N]	-0.0091	-0.045	0.031	0.21
g_{33} [V·m/N]	0.0197	0.0109	0.10	0.33
Band gap [eV]	2.67	3.4	6.2	6
Relative permittivity	650 – 1000	9.9 – 10.8	8.5 – 10.5	12
Resistivity [Ω·cm]	> 10^9	>10^7	>10^{14}	>10^{15}
Typical deposition Techniques	Sol-gel process, pulsed laser deposition, sputtering	Sputtering	Sputtering	Drop casting
Ferroelectricity	Yes	No	No	Yes
Poling	Yes	No	No	Yes

According to previous considerations, the selection of piezoelectric material becomes crucial in the design of tactile devices. In MEMS technology, most of the piezoelectric thin films are polycrystalline materials. Among them, aluminum nitride (with chemical formula AlN) can match all previously mentioned requirements.

2.4.1. *C*-AXIS ORIENTED ALUMINUM NITRIDE

In the last decades, the most studied and used non-ferroelectric piezoelectric thin film has been aluminum nitride. It has been widely used especially in BAW (Bulk Acoustic Wave) and SAW (Surface Acoustic Wave) devices. In spite of its piezoelectric properties weaker than ferroelectrics, it shows high propagation velocity of bulk and surface acoustic waves [80-83]. Many other MEMS devices have been demonstrated using AlN as pressure sensors [46], resonators [84-86], filters [87], switches [88, 89], energy harvesters [90, 91], ultrasonic transducers [92, 93], microphones [94], strain sensors [95] and accelerometers [96].

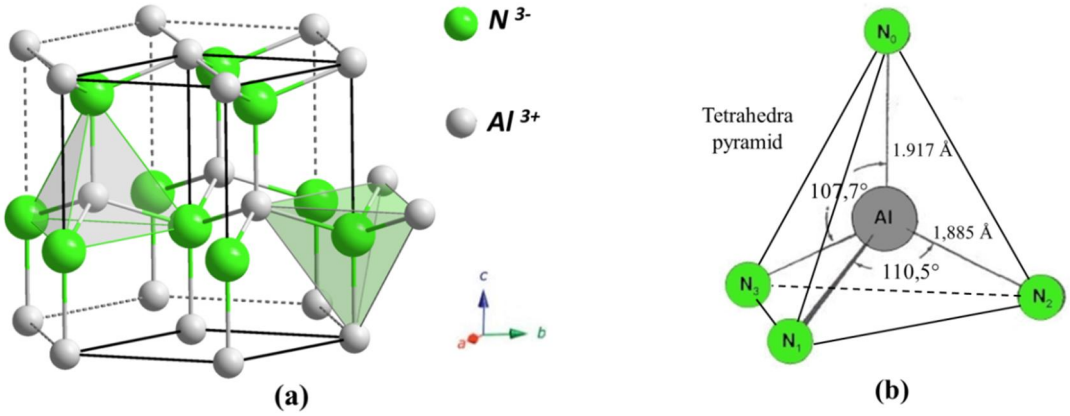

Figure 2.13: a) Wurtzite crystal structure of AlN showing Al atoms (in gray) and N atoms (in green); b) the Al-centered tetrahedral are arranged with one neighbor N atom directly above (parallel to the c-axis) and three neighbors N atoms forming the base of a pyramid.

Aluminum nitride is a class 6mm crystal dielectric that is isotropic in the x-y plane and anisotropic along the z-axis. It is synthesized and used in wurtzite (w-AlN) structured phase which shows piezoelectric response along [0001]. All of the atoms are tetrahedrally coordinated and are arranged in puckered hexagonal rings perpendicular to the crystallographic *c*-axis, as shown in Figure 2.13.

In a single crystal, all of the cations polyhedral are arranged in the same orientation. The relative displacement of center of positive and negative charges within the unit, which is the origin of the piezoelectric d_{33} coefficient in AlN is yielded by the deformation of tetrahedral cell primarily by changing the N–Al–N bond angle, rather than changing the Al–N bond length during the application of a stress parallel to the *c*-axis. Since AlN allows the processing as thin film, it can be used in composite structures where the total elastic properties are often dominated by the other part of structure (i.e. cantilevers and/or membranes), especially in such devices that used to be made out of silicon with enhanced performances.

Poly-crystalline AlN can be obtained by reactive sputter-deposition of pure Aluminum target in N_2 and Ar atmosphere. AlN does not require poling or post-deposition annealing to exhibit

piezoelectric properties, being not a ferroelectric material. AlN does not exhibit conductivity problems and good films can be grown between 100 and 900°C. Moreover, it is a large band gap (6.28 eV) material with large electrical resistivity ($1 \cdot 10^{14}$ Ωcm), high breakdown voltage ($11 \cdot 10^{6}$ V/cm) and low dielectric loss that makes it suitable for transducers, high thermal conductivity (~ 2.85 W/cm·°C) and low thermal expansion coefficients ($\alpha_{AlN} = 4.2 \cdot 10^{-6}$ °C^{-1}).

These coefficients imply low thermal drifts for the devices. The high chemical stability allows AlN to be used in humid environments, which is not possible for piezo-materials like PZT and ZnO. At the same time, it can be etched under standard conditions to allow the production of multiple devices. Finally, AlN does not introduce contaminants into the CMOS micro-technology process that makes it completely compatible with CMOS.

However, the piezoelectric response of AlN polycrystalline thin films depends on their crystal properties and the presence of impurities. A c-axis preferred orientation, low oxygen content (below 1%), type of substrate, crystal morphology (rocking-curve and grain size) and surface roughness are crucial requirements for achieving good piezoelectric response. Moreover, the properties of the substrate and its corresponding surface characteristics have a strong impact on the degree of c-axis orientation and on the polarity of AlN thin films and final microstructure. Nevertheless, AlN thin films can be grown with excellent crystallinity on different substrates including dielectrics, semiconductors and metallic layers as well as on flexible substrates as polymers and polyimides [97-100]. As a consequence, AlN seems to be the most adequate material for the applications analyzed here.

2.5. CURVED PIEZOELECTRIC TRANSDUCER WITH SPHERICALLY-SHAPED DIAPHRAGMS AS TACTILE TECHNOLOGY

The design of proposed technology has been based on the results of functions and properties of tactile units (as listed in Table I.1) and technological requirements as well as performances and fabrication techniques of various sensing devices (as listed in Table I.2 and Table II.2) analyzed in previous sections. Since the overall device is designed to be sufficiently compact to allow integration into an artificial finger or into other body parts, the guideline parameters are to decrease the sizes of individual units and spacing between them to allow high density of elements per given area and high spatial resolution. Furthermore, crucial is the achievement of high sensitivity, allowing detection of small fluctuations in applied pressures, and operating pressure range that is within the range of interest for robotics applications.

A piezoelectric circular diaphragm has been used as sensing element for the proposed force/pressure technology. The most common design concept among the piezoelectric

force/pressure sensors involves flat membranes with patterned electrodes. The sensitivity of the sensor, thus, is mostly determined by the piezoelectric coefficient of used material. Furthermore, it is important to consider that discrete sensing elements arranged in a matrix form have the problems of crosstalk and unstable response. As reported by some recent works [72, 74, 75, 79, 101], by adopting a dome-shaped diaphragm as sensing structure, the proposed device is designed to exploit higher sensitivity than a flat counterpart and minimizes the crosstalk between sensing cells.

When mechanical stress is applied to piezoelectric membrane, an electric voltage is generated, exploiting the piezoelectric effect. The generated electrical signal is proportional to the magnitude of the applied contact force according to the equation 2.10a (assuming the electric charge density D = 0 at initial equilibrium). Since the piezoelectric voltage constant g_{ip} is the induced electric field (along direction i) per applied mechanical stress (along direction p), while all other stresses are zero, the generated electric field can be expressed as:

$$E_n = g_{3n}\sigma_n \tag{2.1}$$

where n = 1, 2 or 3 and σ_n is the mechanical stress. Compared with a conventional flat tactile transducer in which the stress is dispersed all over the membrane, the dome-shaped tactile transducer allows to concentrate the stress in the center of the unit cell, generating a higher voltage due to the increase cell deformation when a contact force is applied.

With the aforementioned considerations in mind, three-dimensional dome-shaped cells have been fabricated on 25μm thick (DuPont™) general purpose Kapton™ substrate laminated on silicon rigid support by 60μm thick silicone adhesive. The rigid silicon substrate is needed during the microfabrication processes to make the technology compliant with common semiconductors facilities. The final design consists of aluminum nitride circular domes with different radii, embedded between two metal electrodes – made of molybdenum. Structuring the layers into circular shape and rounding stray corners is a way to minimize the cracks propagation, together with the residual compressive stress, allowing to prevent cracks generation and to release the crystal strain over the polymer to increase the damping properties. Otherwise, these shapes present an increased toughness due to residual stresses from differential shrinkage of the materials of each layer upon process cooling [102]. Moreover, the combination of metals and semiconductors layers on polymers exploits the flexibility of the polymer and the electrical stability of the semiconductor at the same time. The use of a soft substrate such as kapton polyimide gives different results from those obtained by using a usual hard substrate, due to the residual stresses generated by differential contraction during the post processing cooling down. The crystalline layers release a compressive stress over the polymer indeed, generating three-dimensional domes with reduced stiffness, compared to the semiconductor materials. Since both the sensing layers and the substrate, upon loading, participate to the deformation, the mechanical properties of the spherically shaped

capacitors take into account both the layered structure and the uplift ring-shaped substrate. Besides, the presence of polyimide substrate confers to the final device enough flexibility and conformability to be adapted to curved surfaces.

A thorough discussion on the elastic and electrical properties of the proposed technology will be argued in the next paragraphs.

CHAPTER III

Contents

Summary

In this chapter, the design of proposed pressure/force sensor based on dome-shaped piezoelectric diaphragm transducer is described.

Firstly, a brief introduction of the working principle of the device is given, focusing on the response of the sensor when an external stimulus is applied.

A theoretical analysis of the elastic deformation of the structure due to the aluminum nitride residual stress on polyimide substrate is then given and the calculation of the corresponding stress responsible of the circular diaphragm releasing and generation of dome-shape geometry is provided.

Moreover, finite element method is used to give a quantitative description of the electromechanical response of the device under stress and to study the dynamic behaviour and the related operating resonances both by FEM simulations and by an *ad hoc* theoretical model, the dome-shaped-diaphragm transducers (DSDT) working like a piezoelectric actuator for ultrasounds emission.

DOME-SHAPED TRANSDUCERS DESIGN AND MODELING

The proposed technology is based on three-dimensional AlN piezoelectric dome-shaped-diaphragm transducers (DSDTs). The piezoelectric properties of the aluminum nitride thin film allow exploiting the duality of the device both as actuator and sensor. As actuator, it finds its major use in the field of tactile systems based on ultrasonic transducers (some examples are reported in Chapter I). As sensor it can be used to directly convert force/pressure impulsive dynamic and long static stimuli in electrical processing signals.

Moreover, the choice of soft and flexible materials as polymer-based substrate (Kapton™) and soft piezoelectric thin-film confers to the final device the ability of bending and adapt to curved surfaces.

3.1. AlN/POLYIMIDE-BASED DSDT TRANSDUCER

In this study, AlN circular tactile transducers, with a thickness of 1 μm on a 25 μm-thick Kapton™ and realized by standard micromachining process, are presented. The unit cell consists of flexible piezoelectric circular plate made of *c*-axis highly-oriented AlN. The membrane is embedded between molybdenum metal electrodes in order to collect the charges generated by direct piezoelectric effect or to provide the electrical field for the generation of a mechanical displacement by means of reverse piezoelectric effect. The thickness of the electrodes is 150 nm for the common ground and 300 nm for the top electrode, respectively.

The stress release of the active layers (AlN and, marginally, molybdenum) generates three-dimensional uplifted circular domes with structural stiffness well below the stiffness of composing materials. The deposition of AlN crystalline film on a polymeric substrate, such as polyimide, manifests a natural organization in dome structure which is lifted up after release from the substrate surface. This effect is due to the compressive residual stress difference of AlN over the polyimide.

The sensing mechanism of the transducer mainly relies on the dome shape; when a normal force is applied on the top of the dome, a mechanical stress occurs in the AlN thin layer that becomes electrically polarized due to both piezoelectric and flexoelectric effects (these effects are debated in details in section A.1 and A.2 of Appendix A). According to the synergistic interaction of these effects, the total induced electric polarization P_k is described by the equation:

$$P_k = e_{kij} S_{ij} + \mu_{klij} \frac{\partial S_{kl}}{\partial x_j} \tag{3.1}$$

where e_{kij} is the appropriate piezoelectric stress coefficient along the axis of the applied strain S_{ij} in the relevant direction specified by *i* and *j* indexes, μ_{klij} is the flexoelectric constant, $\partial S_{kl}/\partial x_j$ is the strain gradient and x_j is the position coordinate.

A schematic of the working principle of the transducer as force/pressure sensor for tactile application is shown in Figure 3.1. When an external stimulus, i.e. a force *F*, is applied on the domes, the bending of the structure is transferred to the aluminum nitride thin film and causes the generation of positive and negative charges on its opposite faces. The charges are then collected by the metal electrodes as output voltage signal.

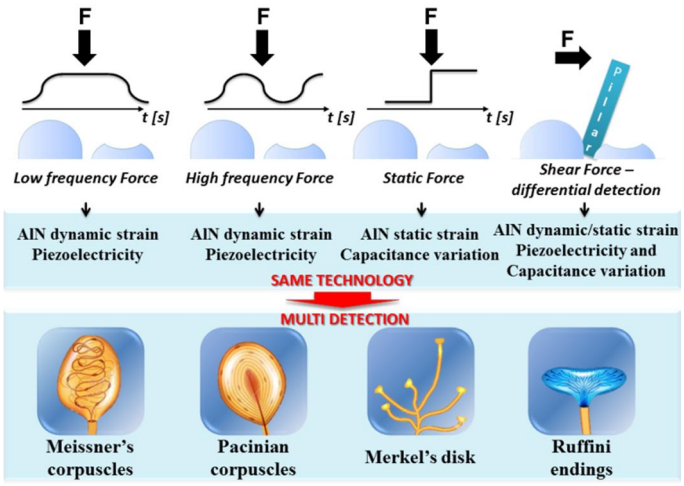

Figure 3.1: Schematic of the working principle of the proposed technology as force/pressure sensor for tactile applications.

In this way, the device is able to detect both low and high frequency dynamic impulsive forces that are applied in a perpendicular direction to the device surface. Moreover, it allows also the detection of long static perpendicular stimuli as a capacitance variation ΔC at different forces amplitude, exploiting the dielectric properties of the Mo/AlN/Mo stack on polyimide substrate and the steady deformation of the convex structure. Furthermore, the detection of shear forces (e.g. due to the slippage of objects) is also allowed by positioning the dome in a cross-layout design and collecting the differential output signal – e.g. from a pair of domes. In this way, multi detection of different stimuli is made possible, mimicking the behaviour of human tactile sensing cell by only one technology.

An overview of the final device is displayed in Figure 3.2 where the tactile flexible skin is thought to have quartet of domes placed in a cross-layout configuration array. A polymer-based cover and pillar are figured in order to apply normal and shear forces/pressures to the quartet below.

The device can be used also as piezoelectric ultrasonic transducer, whose electromechanical behaviour can be modelled assuming that the circular elements behave as a mechanically fully-clamped homogeneous plate resonator.

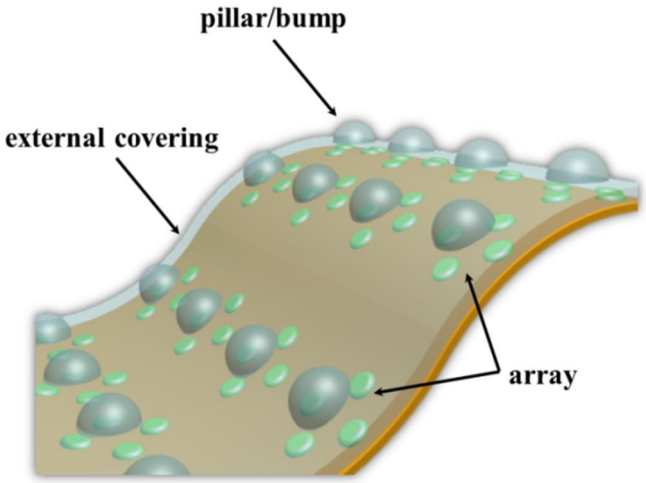

Figure 3.2: Schematic of a final tactile skin based on micro-domes transducers.

3.2. MODELLING OF CURVED PIEZOELECTRIC DIAPHRAGMS

In bio-inspired tactile systems, an efficient artificial tactile skin requires flexibility, stretchability and robust technology as well as it must be able to provide a large amount of information. Proper analysis, based on FEM simulations and theoretical models, is fundamental for a complete understanding of the operation principle of curved DSDTs and for the related design optimization.

3.2.1. MODELING OF ELASTIC DEFORMATION DUE TO RESIDUAL STRESSES

A multi-layered structure is subjected to residual stresses which arise because of mismatch in coefficient of thermal expansion between layers when the system is cooled down to room temperature or it is subjected to temperature changes during its application; otherwise it depends on mismatch of lattice constants between the substrate and the epitaxially grown films. This last effect can be modelled as an intrinsic stress that reflects the internal structure of a material during its deposition. It mainly depends on some parameters as deposition rate and temperature, pressure in the deposition chamber, incorporation of impurities during the film growth, grain structure, fabrication process defects, etc. In most cases, intrinsic stress is non-uniform through the depth and it is therefore responsible of stress gradient. The study of the stress due to AlN on the polyimide substrate and responsible of the three-dimensional dome-shape structure is shown below.

An accurate analysis of residual stresses in multi-layered structures has been performed by Stoney [103], who has gathered a simple solution to relate the stress in a bilayer film to the radius

of curvature R_c of the system. According to this formulation, the residual stress can be calculated as:

$$\sigma = \frac{E_s\, t_s}{6 t_f R_c} \tag{3.2}$$

where E is the Young's modulus and t states the thickness (the subscripts s and f refer to the substrate and deposited film, respectively). The Stoney's model assumes the film thickness to be infinitesimal compared to the substrate thickness. Actually, the accuracy of Stoney's equation has been improved by including higher order terms of film thickness [104-107].

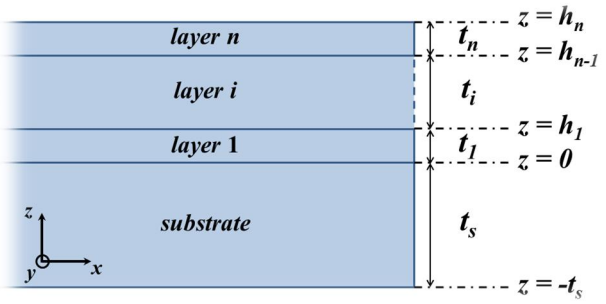

Figure 3.3: Schematic of the cross section of a multi-layered structure with *n* layers deposited on a substrate.

The assumptions of the Stoney's equations can be adjusted to explain the generation of residual stress that is responsible of the generation of spherically shaped circular piezoelectric cell, still made of *n* layers. In order to analytically model the elastic deformation of the multi-layered circular shell, it is assumed to behave as a mechanically fully-clamped homogeneous plate. The cross section of the corresponding multilayer structure is displayed in Figure 3.3.

According to the schematic, *n* layers of film with individual thickness t_i – the *i* index ranging from 1 to *n* – are deposited on the substrate, whose thickness is supposed to be t_s. Being the layer 1 immediately adjacent to the substrate, the height of each layer is related to the thickness by the following relation

$$h_i = \sum_{k=1}^{i} t_k \qquad (i = 1,\ldots., \mathrm{n}) \tag{3.3}$$

The strain distribution along the longitudinal (x and y) direction of the layers in the system can be decomposed into a uniform and a bending component, as:

$$\xi = \xi_{unif} + \frac{z - t_{bend}}{R_c} \qquad z \in [-t_s, h_n] \tag{3.4}$$

where ξ_{unif} is the uniform strain component and t_{bend} defines the location of the bending axis where the bending strain component is zero (*neutral axis*). In case of a multilayer obtained by deposition and cooling down processes, the normal stresses in the substrate and films can be related to the strains by the equations:

$$\sigma_s = E_s(\xi - \alpha_s \Delta T) \qquad -t_s \leq z \leq 0 \tag{3.5a}$$

$$\sigma_i = E_i(\xi - \alpha_i \Delta T) \qquad i = 1,\ldots,n \tag{3.5b}$$

where α_s and α_i are the coefficients of thermal expansion of the substrate and *i*-th film and ΔT is the temperature variation. E_i is the biaxial Young's modulus of the *i*-th layer, defined as $E_i = E_i'/(1 - \nu_i)$, E_i' and ν_i being the Young's modulus and the Poisson's ratio, respectively.

In order to determine the strain/stress distribution in the multilayer, some boundary conditions must be taken. It is assumed that the resultant forces due to uniform strain component and to the bending strain component are zero. Due to internal stresses, mismatch forces arise at film/substrate interface. Each set of forces can be replaced by the static equivalent combination of force and moment, supposing that the bending moment with respect to the neutral axis is in equilibrium with the applied moment per unit width *M*. By the previous hypothesis, the terms of equation 3.4 can be expressed as:

$$\xi_{unif} = \frac{(E_s t_s \alpha_s + \sum_{i=1}^{n} E_i t_i \alpha_i)\Delta T}{E_s t_s + \sum_{i=1}^{n} E_i t_i} \tag{3.6a}$$

$$t_{bend} = \frac{-E_s t_s^2 + \sum_{i=1}^{n} E_i t_i (2h_{i-1} + t_i)}{2\left(E_s t_s + \sum_{i=1}^{n} E_i t_i\right)} \tag{3.6b}$$

$$\frac{1}{R_c} = \frac{3\left[E_s\left(\xi_{unif} - \alpha_s \Delta T\right) t_s^2 - \sum_{i=1}^{n} E_i t_i \left(\xi_{unif} - \alpha_i \Delta T\right)(2h_{i-1} + t_i)\right] + 6M}{E_s t_s^2 (2t_s + 3t_{bend}) + \sum_{i=1}^{n} E_i t_i \left[6h_{i-1}^2 + 6h_{i-1} t_i + 2t_i^2 - 3t_{bend}(2h_{i-1} + t_i)\right]} \tag{3.6c}$$

When the thickness ratio between the films and the substrate is smaller than 10%, the average stress, $\bar{\sigma}$, through the film thickness defined as

$$\bar{\sigma} = \frac{1}{t_i} \int_0^{t_i} \sigma_i dz \tag{3.7}$$

is often considered. When the stress distribution along the films cannot be ignored, a first-order approximation can be derived, such that the stresses on the substrate and the *i*-th film can be expressed as:

$$\sigma_s = \frac{2}{t_s^2}\left\{3z + 2t_s - \frac{2}{E_s}\sum_{j=1}^{n} E_j t_j\right\}\sum_{i=1}^{n} E_i t_i(\alpha_i - \alpha_s \Delta T) \tag{3.8a}$$

$$\sigma_i = E_i\left\{\alpha_s - \alpha_i + 4\sum_{j=1}^{n}\frac{E_j t_j(\alpha_j - \alpha_s)}{E_s t_s}\right\}\Delta T \tag{3.8b}$$

which take into account a modification of the stress distribution and the shift of neutral axis as well as the influence of other films on residual stress of each layer. Thus, the average residual stress in the *i*-th film can be calculated by replacing the equation 3.8b in 3.7.

This analytical model can be used to calculate the stress generated by AlN on kapton polyimide. Since the thickness of the metal electrodes is smaller compared to the thickness of piezoelectric film and structural substrate, the tetra-layered structure (Mo/AlN/Mo/Kapton) can be approached to a bilayer system made just of polyimide substrate and aluminum nitride layers (for convenience of notation, the subscripts *kpt* and *AlN* are used to rename the substrate and the piezoelectric film, respectively).

When the first-order approximation is taken, the calculation of the residual average stress of AlN on polyimide can be estimated by the equations 3.7 and 3.8b that become

$$\bar{\sigma}_{AlN} = -\frac{E'_{kpt} t_{kpt}^2}{6 t_{AlN} R_c}\left(1 + \frac{t_{AlN}}{t_{kpt}}\right)^{-1} \tag{3.9}$$

without loss of generality, being the ratio t_{AlN}/t_{kpt} equal to 3.9%. This equation can be used to evaluate the dependence of geometrical features of the three-dimensional structures on residual stress. The study on the effects of the residual stress due to the aluminum nitride deposited on the polyimide substrate will be expounded in the next section of this dissertation.

3.2.2. FEM QUALITATIVE ANALYSIS OF DSDT AS SENSOR

Finite element method (FEM) simulations have been implemented in order to understand the electromechanical behaviour of the DSDTs. The general-purpose software platform COMSOL Multiphysics® (Comsol Inc., Burlington, MA) has been used to create the geometry and to perform

the simulations in the stationary and frequency domains, such that both the responses of the device as piezoelectric actuator and sensor have been investigated.

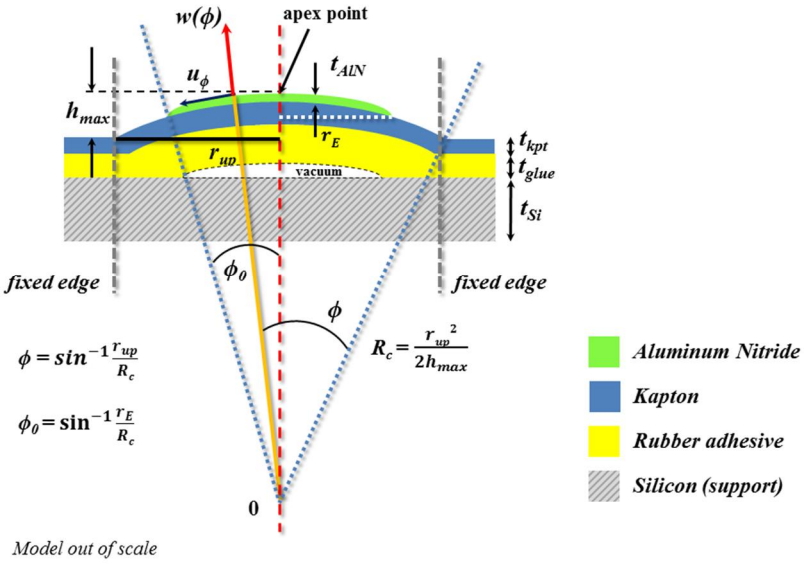

Figure 3.4: Cross section of the axisymmetric curved DSDT with clamped boundary conditions. *w(ϕ)* and u_ϕ are the radial and tangential displacements of a point with angular position ϕ, respectively.

To properly build the geometry, some assumptions have been taken, as schematized in Figure 3.4. The curved DSDT is composed of an AlN smaller shell whose thickness is t_{AlN}, nominal radius r_E and azimuthal angle $\phi_0 = \sin^{-1}(r_E/R_c)$. The shell has been built on a larger curved structural membrane – made of kapton and adhesive glue bilayer substrate – in order to artificially model the pre-stressed structure without adding intrinsic stresses. The outer radius of the structural membrane is r_{up} and the corresponding radius of curvature is $R_c = r_{up}^2/(2h_{max})$. The azimuthal angle of larger diaphragm is $\phi = \sin^{-1}(r_{up}/R_c)$. This angle is used to impose the mechanical clamps on outer borders and to fully fix it (as shown in Figures 3.4 and Figure 3.5).

The exploited physics for FEM simulations have been the structural solid mechanics and the electrostatics to simulate the piezoelectric effect. The flexoelectric effect has been taken into account and has been added to the piezoelectric multi-physics as a measured offset.

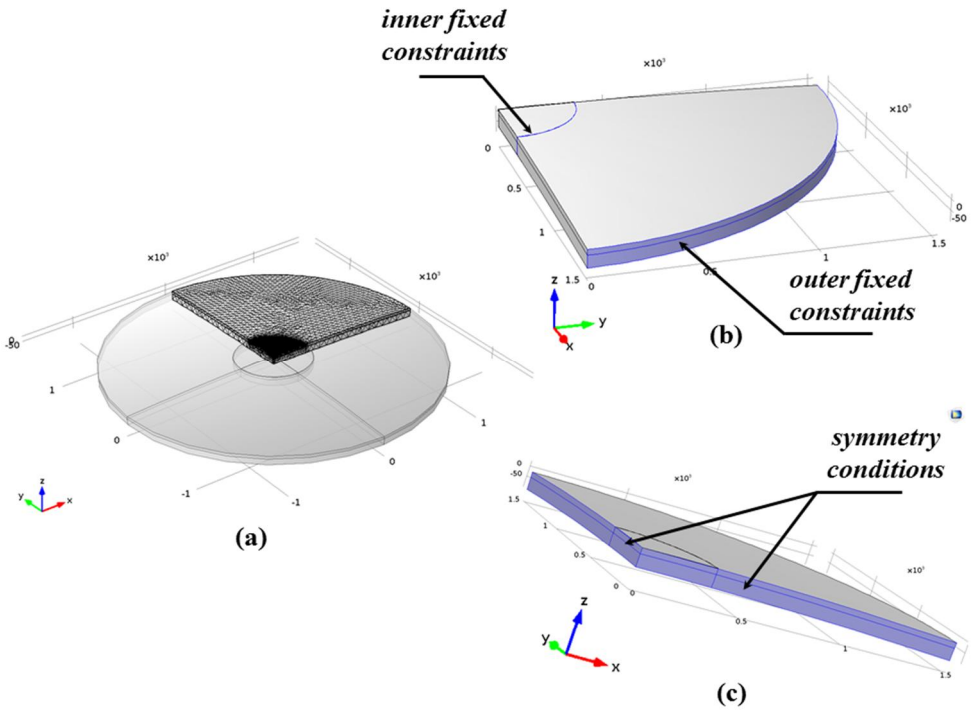

Figure 3.5: a) COMSOL model of curved DSDT with clamped and symmetry boundary conditions. The DSDT is composed of the outer large membrane made of structural kapton and silicon adhesive layers with nominal radius r_{up} and an inner active aluminum nitride membrane with nominal radius r_E. The radius of curvature of the total shell is R_c; b) and c) boundary conditions including fixed constraints and symmetry edges.

The geometry has been built by a 2D axial symmetry space dimension – exploiting the symmetry of a circular diaphragm – in which the central axis (the z-axis as shown in Figure 3.5) corresponds to the centre of dome-shaped transducer. A standard free triangular mesh has been set up as finite element geometry discretization (see Figure 3.5a).

Symmetry conditions have been also imposed (see Figure 3.5c); they allow simulating just a quarter of the total circular diaphragm, decreasing the complexity of the model and speeding up the mathematical solution.

The FEM simulation has been performed applying a uniform impulsive load. Silicon substrate has been included in the structure as rigid fixed support. Since vacuum is supposed to be between the silicon support and the adjacent adhesive layer, contact pairs at the interface have been set (see Figure 3.6a).

These contact pairs define boundaries where the parts can come into contact but cannot penetrate each other under deformation. The uniform force has been finally applied just on the piezoelectric portion of the total shell through the boundary surface load. Fixed constraints have been also defined to fasten the fixed sides of the silicon support. On the contrary, since the thickness of the metal electrodes and their contribution to the vibration as a consequence, is negligible compared to the thickness of the structural substrates and the piezoelectric thin film, they haven't been taken into account in the final geometry. From the solving point of view, this

simplification allows to considerably reduce the calculation complexity and the number of elements and nodes after meshing.

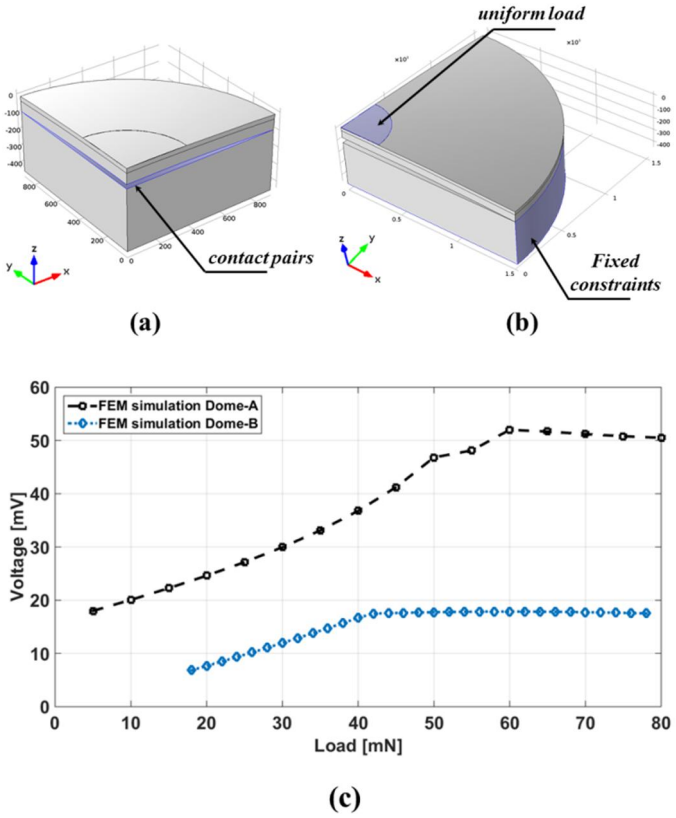

Figure 3.6: a) and b) COMSOL model of curved DSDT with boundary conditions, including the silicon rigid support and c) comparison of the voltage output from the simulated representative Dome-A and Dome-B diaphragms.

A stationary study has been performed to solve the electromechanical analysis when the impulsive load is applied. Two exemplary models of DSDT, hereafter labelled Dome-A and Dome-B, have been simulated. The Dome-A has an uplifted radius r_{up_A}= 1530 µm and the corresponding radius of curvature R_{c_A} = 27.2 mm, being the maximum height of dome h_{max_A} = 43 µm (this last value coming from experimental measurements). On the other hand, the uplifted radius of Dome-B is r_{up_B} = 1210 µm and the corresponding radius of curvature and maximum height are R_{c_B} = 22.2 mm and h_{max_B} = 33 µm, respectively. In both the cases, the piezoelectric membrane has a thickness of 1 µm and a nominal radius r_E= 350 µm, respectively. Isotropic properties have been used for the structural materials (silicon support, rubber adhesive and polyimide substrate), whereas anisotropic properties have been set for the piezoelectric thin film. A detailed list of the material properties used in FEM simulations is reported in Table III.2 – the elastic and the piezoelectric coupling matrices of the aluminum nitride are reported, instead, in Table A.2 of Appendix A.

Table III.2

Material properties of structural kapton and silicon adhesive and piezoelectric AlN used in analysis and simulations.

Parameter	Description	Rubber adhesive	Kapton HN	AlN	Unit
$\boldsymbol{\rho}$	*Density*	1100	1420	3300	kg/m^3
$\boldsymbol{E}$	*Young's modulus*	0.73	2.5	348	*GPa*
$\boldsymbol{\upsilon}$	*Poisson's ratio*	0.47	0.34	0.3	/
$\boldsymbol{\varepsilon}$	*Dielectric constant*	2.9	3.4	9	/
$\boldsymbol{d_{31}}$	*Piezoelectric charge constant*	/	/	2.20	*pm/V*

The normalized output voltage at the peak versus the applied impulsive force provides a qualitative understanding of the device voltage response (see Figure 3.6c). The simulations results show the domes are firstly pushed downwards, with slight compression in polyimide substrate tape, until the released structure is flattened on the silicon substrate. In this region, the stress is transferred to the piezoelectric film, generating the voltage signal according to the voltage/stress relation (see equation 2.1 in section 2.5 of Chapter II). For increasing forces, the constant flattening causes the signal saturation. This evaluation suggests the uplifted area is determinant for the dynamic range of the transducer that easily deforms under impulsive loading.

3.2.3. FEM ANALYSIS OF DYNAMIC RESPONSE OF DSDT AS ACTUATOR

FEM study has been also performed to simulate the frequency response of the curved shell, exploring the indirect piezoelectric effect. In these simulations, the silicon substrate has been neglected. This assumption is allowed assuming the kapton/AlN uplifted shell as an ideally fully-clamped diaphragm, fixed on the outer edges.

In addition, a zero uniform normal pressure p has been initially supposed (both in receive and transmission), such that no boundary load conditions have been applied.

The dynamic response and the radial displacement amplitude of the curved shell have been calculated around resonance frequency of the first vibrational mode.

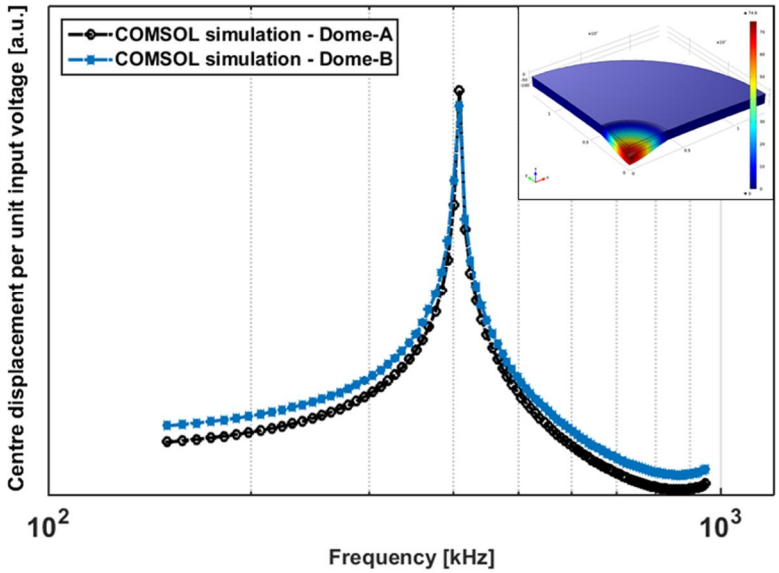

Figure 3.7: Comparison of the centre displacement of Dome-A and Dome-B per unit input voltage versus the frequency coming from COMSOL simulation. A shape-mode representation of the investigated (0,1) mode of resonance is depicted.

To do that, the membranes have been driven by applying a test *AC* voltage signal of 3 volts amplitude. In the plot of Figure 3.7, the comparison of the centre displacement of the curved DSDTs per unit input voltage versus the excitation frequency, for the DOME-A and DOME-B diaphragms is shown. Since the voltage driven piezoelectric region of the shell has the same radius in both the DOME-A and DOME-B, the results suggest the resonance frequency is around 408.6 kHz and it doesn't depend on the maximum height and radius of curvature. However, a slight variation of the centre displacement per unit input voltage has been achieved, the Dome-A having an increase of displacement about 24.4% compared to Dome-B. The variation of the centre displacement and the maximum height has been investigated as a function of the radius of curvature and the corresponding relationships are reported in Figure 3.8a. Finally, the effects of the shell curvature on the displacement have been studied with respect to maximum height, keeping all the other geometrical parameters still unchanged (see Figure 3.8b).

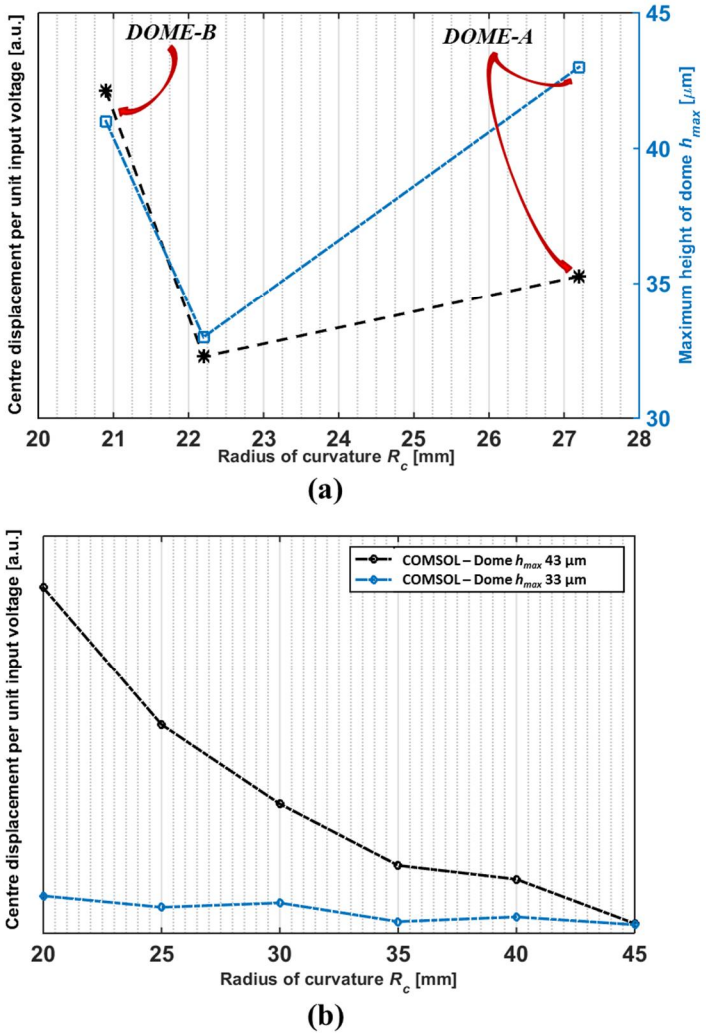

Figure 3.8: a) variation of the centre displacement per unit voltage and height of the dome as a function of the radius of curvature; b) effect of the shell curvature on the displacement when the height of the dome is kept still constant.

This last study show the centre displacement gradually decreases as the curvature becomes large and it gets closer to a common value when both the domes approach a planar circular plate (corresponding to a large radius of curvature). This result suggests that curved diaphragms have an improved electromechanical coupling with higher mechanical deformation per unit energy compared with the conventional unimorph plate structures [108, 109]. The improvement of electromechanical coupling is mainly due to the fact that dome-shaped transducers exploit in-plane piezoelectric strain, which leads to large out-of-plane deflection because of their spherical curvature and fully-clamped or ideally fully-clamped periphery.

3.2.4. ANALYTICAL MODEL OF DYNAMIC RESPONSE OF DSDT AS ACTUATOR

An additional theoretical model of the DSDTs, together with FEM analysis, can be used to predict the dynamic response of the device due to the strain mismatch between the layers resulting from the voltage-induced piezoelectric stress. The Love's first approximation theory is appropriate to geometrical and dynamical characterize the elastokinetic deformation of thin spherical shells [110, 111]. Since the transverse normal at curved diaphragm remains still normal to the deformed middle surface, the transverse shear strains can be approached to zero and all nonlinear terms can be neglected. The transverse normal strain can be supposed even negligible. If (r, θ, ϕ) are the spherical coordinate system defined by the transformation $x = (R_c + \phi)\sin\phi\cos\theta$, $y = (R_c + \phi)\sin\phi\sin\theta$ and $z = (R_c + \phi)\cos\phi$ (R_c being the radius of curvature) thus $\varepsilon_{r\theta} \approx 0$, $\varepsilon_{r\phi} \approx 0$ and $\varepsilon_{rr} \approx 0$. The total strain of spherical shell ε_{ij} in the i- and j-directions is the sum of membrane and flexural strains ε_{ij}^0 and ε_{ij}^1, respectively:

$$\varepsilon_{ij} = \varepsilon_{ij}^0 + \gamma\varepsilon_{ij}^1 \qquad \text{where } i, j \in \{\theta, \phi\} \tag{3.10}$$

where γ is the radial position measured from the centre of the diaphragm [112, 113]. The strains relations come from the theory of Love's first approximation [114]. The transverse shear stresses $\sigma_{r\theta}$ and $\sigma_{r\theta}$ are still negligible as well as the transverse normal stress is small compared with the other normal stresses ($\sigma_{r\theta} \approx 0$). If an external electric field E_r is applied along the polarization direction, the transverse piezoelectric charge constants $d_{r\theta}$ and $d_{r\phi}$can be assumed to be equal and with a magnitude of d_{31}.

For a multi-layered structure made of polymer substrate and aluminum nitride with electrodes – as in the proposed technology – different densities, Young's moduli and Poisson's ratio must be taken into account. Moreover, the piezoelectric coefficient d_{31} is zero in non-piezoelectric films. However, displacements are identical for all of the layers because of the thin layer condition. Let the piezoelectric medium be also modelled as an isotropic material, whose mechanical properties are described by the Young's modulus E_p and the Poisson's ratio ν_p.

In order to include the vibrational contribution of each layers in the multi-layered structure, the average density ρ_{av}, Young's modulus E_{av}, Poisson's ratio ν_{av}, total thickness $d = \sum_{i=1}^{n} t_i$ and thickness of each layer t_i are used:

$$\rho_{av} = \frac{\sum_{i=1}^{n} \rho_i t_i}{\sum_{i=1}^{n} t_i} \tag{3.11a}$$

$$E_{av} = \frac{\sum_{i=1}^{n} E_i t_i}{\sum_{i=1}^{n} t_i} \tag{3.11b}$$

$$\nu_{av} = \frac{\sum_{i=1}^{n} \nu_i t_i}{\sum_{i=1}^{n} t_i} \tag{3.11c}$$

The motion of the DSDT in both transmit and receive modes is rotationally symmetric around the z-axis, such that axisymmetric conditions can be employed ($\partial/\partial\theta = 0$). From the Love's approximation, the dynamic stress equations become:

$$\frac{\partial(\sin\phi N'_{\phi\phi})}{\partial\phi} + \frac{\partial(N_{\theta\phi})}{\partial\theta} - \cos\phi N'_{\theta\theta} + \sin\phi\, Q_{\phi\phi} = \rho_{av} dR_c \sin\phi \frac{\partial^2 u_\phi}{\partial t^2} \tag{3.12a}$$

$$\frac{\partial(N'_{\theta\theta})}{\partial\theta} + \frac{\partial(\sin\phi\, N_{\theta\phi})}{\partial\phi} + \cos\phi N_{\theta\phi} + \sin\phi\, Q_{\theta\theta} = \rho_{av} dR_c \sin\phi \frac{\partial^2 u_\theta}{\partial t^2} \tag{3.12b}$$

$$\frac{\partial(\sin\phi Q_{\phi\phi})}{\partial\phi} + \frac{\partial(Q_{\theta\theta})}{\partial\theta} - \cos\phi\left(N'_{\theta\theta} + N'_{\phi\phi}\right) = \rho_{av} dR_c \sin\phi \frac{\partial^2 w}{\partial t^2} - \sin\phi \frac{2E_p d_{31} V}{1-\nu_p} - R_c \sin\phi\, p \tag{3.12c}$$

$$\frac{\partial(\sin\phi M_{\phi\phi})}{\partial\phi} + \frac{\partial(M_{\theta\phi})}{\partial\theta} - \cos\phi M_{\theta\theta} - R_c \sin\phi\, Q_{\phi\phi} = 0 \tag{3.12d}$$

$$\frac{\partial(\sin\phi M_{\theta\phi})}{\partial\phi} + \frac{\partial(M_{\theta\theta})}{\partial\theta} + \cos\phi M_{\theta\phi} - R_c \sin\phi\, Q_{\theta\theta} = 0 \tag{3.12e}$$

where $N_{\theta\theta}$, $N_{\phi\phi}$ and $N_{\theta\phi}$ are the stress resultants, $M_{\theta\theta}$, $M_{\phi\phi}$ and $M_{\theta\phi}$ are the stress couples, p is the received/transmitted pressure perpendicular to the curvature of shell, V is the applied voltage signal, $Q_{\theta\theta}$ and $Q_{\phi\phi}$are the transverse shear stress resultants and $N'_{\theta\theta}$ and $N'_{\phi\phi}$are modified stress resultant [110, 111] (see Figure 3.9).

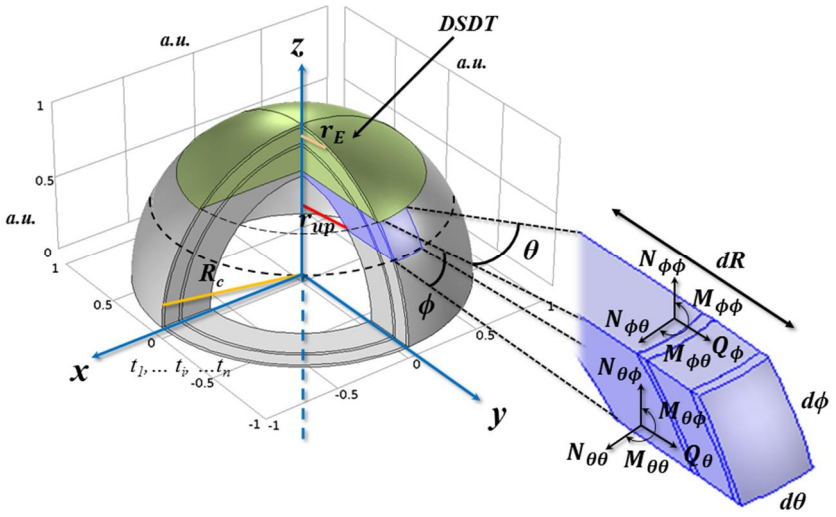

Figure 3.9: Curved DSDT with radius $\boldsymbol{r_E}$ and radius of curvature $\boldsymbol{R_c}$ in spherical coordinate. The stress couples and the stress resultants are also displayed.

Finally, u_ϕ, u_θ and w are the displacement vector components in ϕ-, θ- and r-directions, respectively.

As proposed by [110] and [111], two differential equations in $F(\phi, t)$ and radial displacement w can be defined, where F is a specific stress function such that:

$$\left[R_c^2\nabla^2 F + (1-\nu_{av}) - \frac{\rho_{av}(1-\nu_{av}^2)R_c^2}{E_{av}}\frac{\partial^2}{\partial t^2}\right]F + \left[(1-\nu_{av})\frac{D}{R_c}\left(\nabla^2 + \frac{2}{R_c^2}\right) - \frac{E_{av}d}{R_c}\right]w = 0 \tag{3.13a}$$

$$\left[R_c^2\left(\nabla^2 + \frac{2}{R_c^2}\right) + \frac{\rho_{av}(1+\nu_{av})R_c^2}{E_{av}}\left(\frac{d^2}{12}\nabla^2 - 2\right)\frac{\partial^2}{\partial t^2}\right]F + \left[DR_c\left(\nabla^2 + \frac{2}{R_c^2}\right)\left(\nabla^2 + \frac{2}{R_c^2}\right) + \rho_{av}dR_c\frac{\partial^2}{\partial t^2}\right]w = R_c p + \frac{2E_p d_{31}V}{1-\nu_p} \tag{3.13b}$$

In previous equation, D is the flexural rigidity of the multi-layered shell, expressed as $D = (E_{av}d^3)/[12(1-\nu_{av}^2)]$. The harmonic solutions of the previous differential equations in F and w are in the form:

$$\begin{Bmatrix} w \\ F \end{Bmatrix} = Re\begin{Bmatrix} w' e^{j\omega t} \\ F' e^{j\omega t} \end{Bmatrix} \tag{3.14}$$

where ω is the operation frequency, whereas w' and F' are the magnitude of the radial displacement and stress function. By substituting F in previous equations 3.13, the equation of vibrational motion of the curved shell in the most general form is:

$$\nabla^6 w' + \beta_1 \nabla^4 w' + \beta_2 \nabla^2 w' + \beta_3 w' = -\beta_4 R_c p - \beta_4 \frac{2E_p d_{31} V}{(1 - \upsilon_p)} \tag{3.15}$$

where

$$\beta_1 = \frac{1}{R_c^2}\{4 + (1 - \nu_{av}^2)\Omega^2\} \tag{3.16a}$$

$$\beta_2 = \frac{12(1 - \nu_{av}^2)}{d^2 R_c^2}(1 - \Omega^2) \tag{3.16b}$$

$$\beta_3 = \frac{12(1 - \nu_{av}^2)}{d^2 R_c^4}\{2 + (1 + 3\nu)\Omega^2 - (1 - \nu^2)\Omega^2\} \tag{3.16c}$$

$$\beta_4 = \frac{1}{D R_c^3}\{(1 - \nu_{av}^2) + (1 - \nu_{av}^2)\Omega^2\} \tag{3.16d}$$

The term Ω^2 depends on the operating frequency and materials properties, as follows:

$$\Omega^2 = \frac{\eta \rho_{av} \omega^2 R_c^2}{E_{av}} \tag{3.17}$$

where η is a corrective parameter that takes into account the presence of multi-layers.

The general solution of equation 3.15 can be found by using the Legendre functions of degree n_α, with α = 1, 2 and 3, such that

$$w'_\alpha = \sum_{\alpha=1}^{3} A_\alpha P_{n_\alpha}(\cos\phi) + B_\alpha Q_{n_\alpha}(\cos\phi) \tag{3.18}$$

where P_{n_α} and Q_{n_α} denote the Legendre functions of first and second kind, respectively. The degrees of Legendre functions are calculated as reported in [110]. The functions Q_{n_α} has a singular character when the angular position from the shell axis ϕ reaches the apex point ϕ = 0. In order to keep the regularity of the equation 3.18, the coefficients B_α must be set equal to zero.

The specific solution of equation 3.15 depends on both the radial load and the applied voltage, according to the following expression:

$$w'_{sp} = -\frac{\frac{1}{D_p}(1-\nu_p) + (1-\nu_p^2)\Omega^2}{\frac{dE_{av}}{D}(2 + (1+3\nu_{av})\Omega^2 + (\nu_{av}^2-1)\Omega^4)} R_c \left\{ R_c p_r - \frac{2E_p d_{31} V}{(1-\nu_p)} \right\} \tag{3.19}$$

where $D_p = \left(E_p d^3\right)/\left[12\left(1-\nu_p^2\right)\right]$. The final solution is the superposition of equations 3.18 and 3.19.

The coefficients A_α can be calculated imposing the boundary conditions, as shown in the cross section of Figure 3.9. The curved shell is supposed to be ideally clamped on its edges, such that it cannot translate in the *r*- and ϕ- directions or rotate around the ϕ-axis. In other words,

$$w'|_{\phi=\phi_0} = 0 \tag{3.20a}$$

$$u'_\phi\big|_{\phi=\phi_0} = 0 \tag{3.20b}$$

$$\left.\frac{dw'}{d\phi}\right|_{\phi=\phi_0} = 0 \tag{3.20c}$$

where $\phi_0 = \sin^{-1}\left({}^{r_{up}}/_{R_c}\right)$ is the azimuthal angle at the edge of the spherical shell with radius r_{up}. According to the previous boundary conditions and the magnitude of specific solution w'_{sp}, the coefficients A_α, α = 1,2,3, are as follow:

$$A_1 = -\frac{1}{c_1}(A_2 c_2 + A_3 c_3) \tag{3.21a}$$

$$A_2 = A_3\left(\frac{c_3 b_1 - c_1 b_3}{b_2 c_1 - c_2 b_1}\right) \tag{3.21b}$$

$$A_3 = -\frac{w'_{sp}}{\left[\left[\left(\frac{c_1 b_3 - c_3 b_1}{b_2 c_1 - c_2 b_1}\right)\frac{c_2}{c_1} - \frac{c_3}{c_1}\right] a_1 + \frac{c_3 b_1 - c_1 b_3}{b_2 c_1 - c_2 b_1} a_2 + a_3\right]} \tag{3.21c}$$

where, for i = 1,2,3,

$$a_i = P_{l_i}(\cos\phi_0) \tag{3.22a}$$

$$b_i = (l_i + 1)\left\{\csc\phi_0\, P_{l_i+1}(\cos\phi_0) - \cot\phi_0\, P_{l_i}(\cos\phi_0)\right\} \tag{3.22b}$$

$$c_i = \frac{\left[\frac{\lambda_i - 2}{12(1-\nu_{av})}\left(\frac{d}{R_c}\right)^2 + 1\right]}{[-\lambda_i + (1-\nu_{av}) + (1-\nu_{av}^2)\Omega^2]} b_i \tag{3.22c}$$

The model, coded in MATLAB, has been used to analyse the clamped curved Dome-A DSDT. As shown in Figure 3.10, the theoretically calculated resonant frequency is 384.9 kHz whereas the FEM predicted resonant frequency is 408.6 kHz (see section 3.2.3). These frequency values match quite well, being the difference equal to 6.1%. This small percentage difference is probably due to the fact that AlN has been modelled as an isotropic material in the theoretical model (as explained even in [111]). Figure 3.10 shows also the trend of the centre displacement per unit input voltage of the shells as a function of the radius of curvature. Since the different approach to analytically model the system, the predicted displacement differs from the FEM analysis (blue curve in the graph), but the trend is kept still unchanged.

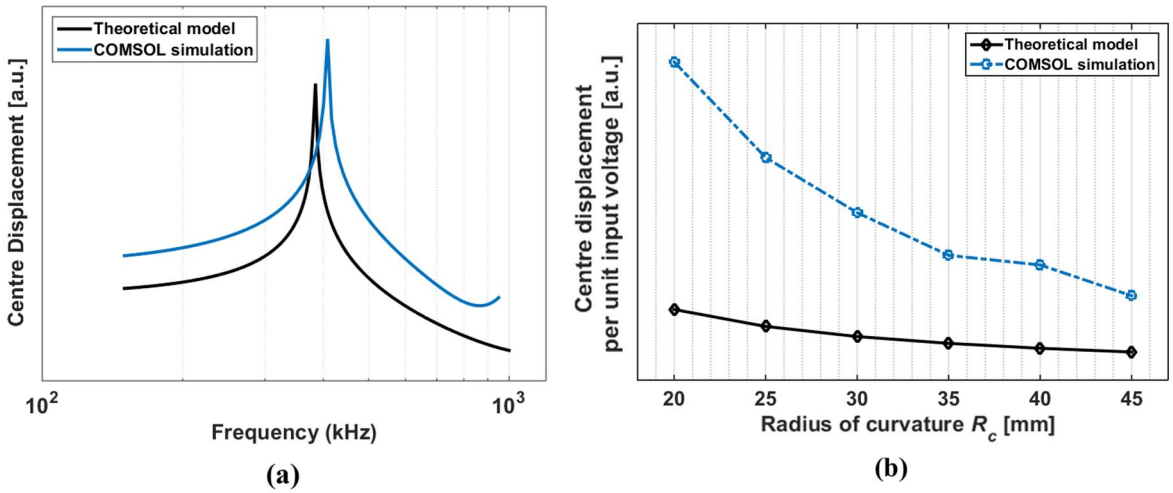

Figure 3.10: a) Comparison of the radial displacement per unit input voltage of the DOME-A with nominal radius r_E= 350 µm, maximum height h_{max} = 43 µm and radius of curvature R_c= 27.2 mm as a function of the frequency, from theoretical and FEM calculation; b) the centre displacement per unit input voltage is compared as a function of the radius of curvature for a representative dome with 43 µm of maximum height.

.

Even from the theoretical analysis, the resonance of the diaphragms doesn't depend on the maximum height and radius of curvature but it depends rather on the voltage driven AlN piezoelectric region, whose radius is equal to r_E, as already proved by FEM analysis.

CHAPTER IV

Contents

Summary

In this chapter the fabrication of piezoelectric DSDTs, based on highly oriented *c*-axis aluminum nitride, is described. After a brief introduction on the design features, a comprehensive description of the fabrication protocol is given. The microfabrication steps and the lithographic masks are described in details, underlying the simplicity of the fabrication protocol.

An exhaustive electromechanical characterization of the device is then carried out, showing the device allows an enhanced transduction response, as actuator as well as force sensor, when the piezoelectric cells are patterned in circular dome-shaped geometries.

The capabilities of the devices as actuator are then depicted and the results of experimental measurements and results on resonance frequencies and out-of-plain displacements, when low voltage is used to drive the cells, are described.

The detection of dynamic and static load is finally illustrated, in order to test the device as force/pressure loads sensor, exploiting both piezoelectric and flexoelectric capabilities of the aluminum nitride material.

DSDT MICROFABRICATION AND EXPERIMENTAL CHARACTERIZATION

4.1. MICRO-FABRICATION OF DSDT PROTOTYPES

Standard microfabrication techniques have been employed to fabricate the array of DSDTs. The overall microfabrication process involves deposition of metal and piezoelectric films, photolithography and plasma-based dry etching to pattern thin films with the desired features.

The DSDT devices have been designed and developed according to FEM and theoretical analysis, previously described in Chapter III and following the typical requirements of force/pressure systems for tactile applications. Therefore, based on a suitable fabrication protocol, the photolithographic masks have been properly drawn. The protocol has been thought and created to have the minimum number of steps, reducing, in this way, the complexity of the microfabrication process as a whole. Figure 4.1 shows the complete design of three photolithographic masks that have been used to fabricate a 2x2 array of DSDTs. Starting from the as grown material as in Figure 4.1a, a Mo/AlN/Mo three-layer stack directly deposited on polyimide substrate by all in one process, the following steps are included in the photolithographic mask: 1) the definition of the AlN circular membranes by an etching of the aluminum nitride, together with top metallization used also as hard masking, until the lower metal layer is reached (Figure 4.1b); 2) the patterning of bottom metal common electrode (Figure 4.1c); 3) the realization of top electrodes by additional metal deposition and lift-off (Figure 4.1d).

The bottom electrode has been patterned as circular common ground with a radius of 1 mm in order to incorporate the most part of the quartet of domes, placing the external edge of each circular membrane close to the ground border, allowing a top electrode fabrication without short circuit with the ground electrode. Four pads with square shape and a surface of 1 mm^2, 90° out-of-phase placed, have been included to easily connect to bottom electrode with external connections and wires (reducing the complexity of the wiring itself). Metal stripes with length 2.4 mm and width 500 μm, respectively, connect the square pads to the common circular ground.

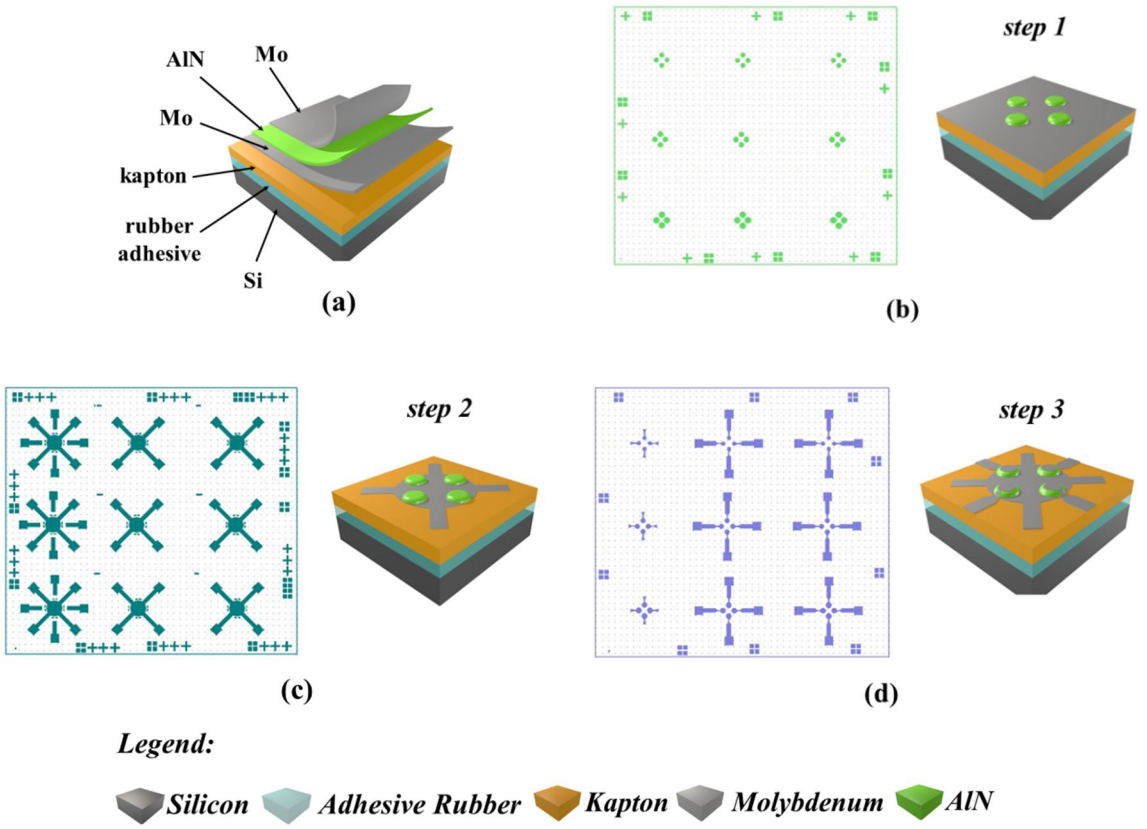

Figure 4.1: Photolithographic masks needed to realize the array of DSDTs and fundamental process steps of the developed microfabrication protocol.

Top electrodes have been designed with a circular region whose radius is equal to the AlN membrane. This portion of the top electrodes is needed to embed the AlN cell. Pads and connection metal stripes, still 90° out-of-phase placed, have been included, the length and the width being still 2.4 mm and 500 μm, respectively. Moreover, their position has been designed in order to avoid overlapping with bottom metallization, exploiting the direction defined by the membrane edges close to the ground border – top and bottom electrodes have been 45° out-of-phase placed. The final device consists of four DSDTs with a nominal radius of r_E = 350 μm placed in cross-layout configuration (hereafter labelled DOME–A, –B, –C and –D) such that it acquires a star shape that makes the overall quartet to be conformable to curved surfaces, leaving the active region well connected anyway. A detailed description of the microfabrication protocol will be given in the next paragraph.

4.1.1. MATERIALS PROPERTIES

4.1.1.1. Aluminum Nitride Texture

A fundamental step of the microfabrication protocol is the deposition of the aluminum nitride thin film. The stacked structure Mo/AlN grown on polyimide kapton has been deposited by sputtering in highly-oriented texture (as reported in previous works [79, 100, 115-118], the sputtering deposition recipe has been conveniently optimized) perpendicular to the substrate regardless of the underlying amorphous state.

SEM inspection of the sputtered layers, as displayed in Figure 4.2a, have revealed the perpendicular orientation of AlN texture and a suggestive continuity through the single nanograin.

X-ray diffraction spectrum have shown peaks at about 36° due to the reflections (0002) of the aluminum nitride and at about 41° due to the reflections (110) of the molybdenum, as reported in the graph of Figure 4.2b. The full width at half maximum (FWHM) of the rocking curves, that is 0.52° and 0.54° for the molybdenum and the aluminum nitride, respectively, are also reported (in the inset). From the last, it is possible to infer that AlN thin film has been grown highly-oriented in wurtzite phase, allowing the piezoelectricity of the material. Moreover, a very good adhesion of the polycrystalline structure to the polymer substrate has been achieved.

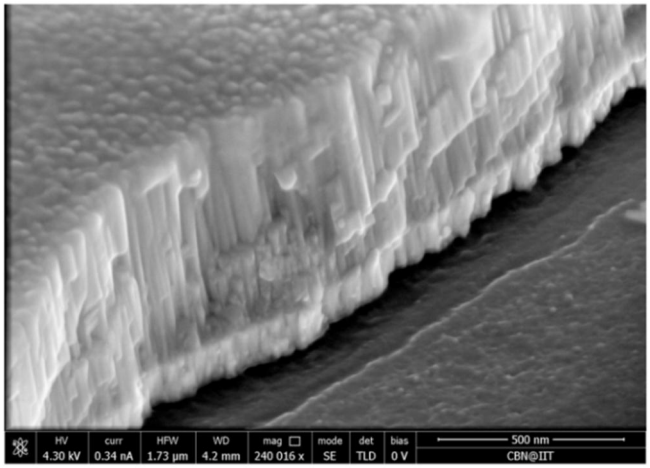

(a)

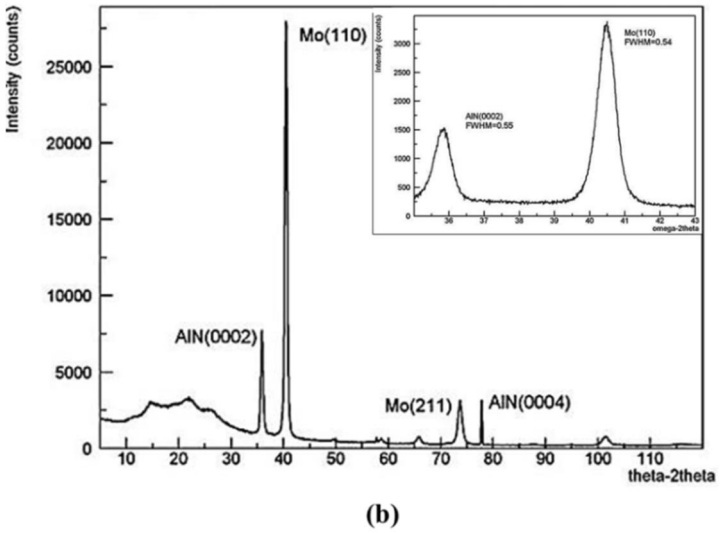

Figure 4.2: a) SEM image of bottom Mo and AlN films deposited on kapton substrate showing the typical columnar structure; b) X-Ray diffraction spectra θ –2θ with 5° < θ > 120° for the structure Mo(120 nm)/AlN(700 nm); in the inset the rocking curve of the AlN (0002) peak has a full width at half maximum (FWHM) of 0.55 (adapted from [79]).

4.1.1.2. Electrodes

In previous paragraphs, the relevance to obtain high piezoelectric coefficient of aluminum nitride material by the synthesis of *c*-axis oriented thin film has been highlighted. Such orientation is advantageous – especially when the piezoelectric thin film is sandwiched between two metal electrodes – as long as the substrate does not impose any other atom arrangement for lowering the interface energy of the nuclei. One of the common used deposition methods of AlN is the reactive sputtering from an aluminum target in nitrogen-containing plasma, sustained either by radio frequency (RF) power or by direct current (dc) power. These methods can produce polycrystalline AlN thin films on many different substrates and at a moderate temperature. The deposited films may exhibit a perfect *c*-axis orientation and piezoelectric activity. Despite the influence of sputtering conditions have a strong impact on the microstructure of AlN thin films and on the degree of *c*-axis orientation and polarity, the condition of the substrate surfaces is another factor of utmost and not secondary importance. Recent investigations have been conducted to observe the effects of thin films made of textured platinum, titanium, aluminum and copper even on dielectric layers, such as silicon dioxide (SiO_2), on crystal orientation and residual stress in polycrystalline AlN [98, 119, 120]. These works have indicated that both the substrate and the sputtering process conditions significantly influence the growth and the properties of piezoelectric thin films. The quality of the electrodes surface is especially responsible for the nucleation of the hexagonal structure of AlN and thus for the subsequent textured growth along the (0002) direction. Such that,

a stable nucleation surface with a hexagonal symmetry may promote the growth of very high quality aluminum nitride thin films, despite a large lattice mismatch.

In some applications, additional features such as low resistivity, small density and high conductivity are required. As material with relatively small density and high conductivity, while high acoustic impedance is still held, molybdenum (Mo) is considered as the optimal compromise. Molybdenum is a body cubic centred (bcc) refractory metal and it naturally grows with (110) texture. The problem as AlN substrate is that the hexagonal symmetry is lost. However, an optimal fabrication of Mo electrodes for the deposition of highly *c*-axis oriented AlN thin films is possible [115, 121, 122]. Since the residual stress in AlN thin films depends on the ion bombardment, optimal Mo substrates allow properly calibrating the substrate bias in order to tune film structural and functional properties.

Thanks to the previous mentioned properties, molybdenum has been selected as really promising material for the technology that has been analysed in this dissertation.

4.1.1.3. Flexible Substrate

MEMS tactile transducers are usually based on inorganic materials such as metals or semiconductor, like silicon. The most relevant drawback of Si-based devices for tactile application is that they are typically rigid and brittle and not suitable for large deformations and coverage of curved three-dimensional surfaces. In order to overcome the current limits of silicon-based MEMS devices and enable components such as piezoelectric transducers to address the requirements of flexible electronic devices – ability to bend, expand as well as adapt on irregular surfaces – a proper selection of the substrate is then compulsory. The use of soft piezoelectrics such as aluminum nitride has opened up new perspective in the integration of such piezoelectric materials on soft and flexible substrates. One of the most appropriate polymer substrate is Kapton™ which exhibits high mechanical and chemical resistance and wide operating temperature range (−269 °C to +400 °C), allowing it to be processed with the standard CMOS technology. Thanks to the mechanical properties and dimensional stability, substrates made of kapton films minimize the stress at the interface during high temperature thin film deposition and processing. Furthermore, kapton films offer some additional and desirable characteristics, such as high electrical insulating properties and toughness and mechanical resistance. The last make the final device robust enough to sustain large cyclic deformations without damages.

4.1.2. MICRO-FABRICATION PROTOCOL

In Table IV.1, the main steps of typical micro-fabrication protocol of DSDT membranes are illustrated. Piezoelectric DSDTs, consisting of flexible piezoelectric AlN membranes, embedded between molybdenum electrodes, have been fabricated by standard micromachining techniques on 25 μm thick general purpose Kapton HN™ (DuPont™) flexible substrate. The kapton substrate with silicone based adhesive has been laminated on n-type <100> silicon wafer support (with thickness of 545 μm) by ~60 μm thick rubber adhesive (see step n° 1 of Table IV.1) while heated on hotplate at 50 °C. Before gluing the polyimide substrate, the silicon wafer has been rinsed by submersing it in consecutive baths of acetone, isopropyl alcohol (IPA) and deionized (DI) water.

Moreover, to ensure the removal of dust particles and excess moistures, the wafer has been dried by constant nitrogen flow for some seconds. After an accurate cleaning of the laminated substrate exploiting the same baths of acetone, IPA and DI water, the stack structure has been sputtered in DC mode sputtering tool for large area samples (LLSEVO-Oerlikon) in a single run to minimize as much as possible contaminations (step n° 2 of Table IV.1). Molybdenum bottom electrode, with a thickness of 120 - 150 nm, has been deposited from high-purity Mo target (whose purity is 99.999%) at room temperature in a pure argon atmosphere with Ar flow of 16 sccm and dc power of 0.5 kW; the grow rate of the deposition has been 0.8 nm/s (the process time has been ~190'' to reach the thickness of 150 nm) when the working pressure has been set to $1.2 \cdot 10^{-3}$ mbar, while the residual pressure of the chamber before starting the etching process has been kept to $3.7 \cdot 10^{-7}$ mbar. The Mo target has been pre-sputtered in pure Ar atmosphere for 10 min under the same pressure and power conditions to have stable plasma during the actual sputtering. The aluminum nitride piezoelectric film of ~1 μm-thick has been deposited through reactive sputtering from Al target (purity 99.999%) with a ratio Ar/N_2 of 0.75 (12 sccm of Ar and 15.9 sccm of N_2) and power of 2.25 kW, at a grow rate of 0.72 nm/s (the process time has taken 1380''). The working pressure has been stabilized at $1.3 \cdot 10^{-3}$ mbar, whereas the residual pressure has been equal to $2.5 \cdot 10^{-7}$mbar.

Table IV.1

Fabrication protocol of the DSDT prototypes.

1. Kapton tape lamination on silicon wafer at 50°C and wet/dry cleaning.

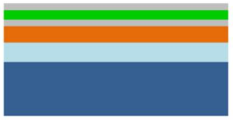

2. Deposition via sputtering of the stack Mo/AlN/Mo on kapton in single run.

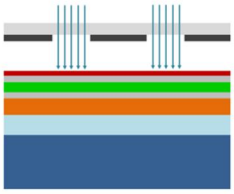

3. Photolithography of the positive mask and resist development.

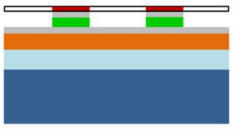

4. $SiCl_4$ dry etching of the top Mo and AlN and patterning of circular shapes.

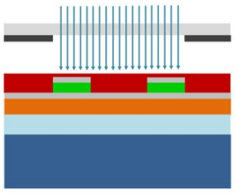

5. Photolithography of the second positive mask and resist development.

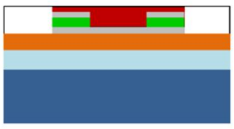

6. H_2O_2 wet etching of the bottom Mo and patterning of the common ground.

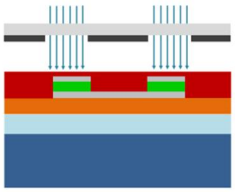

7. Photolithography of the third negative mask with resist tone inversion and development.

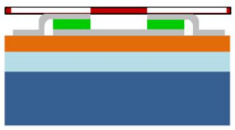

8. Deposition via sputtering of the top Mo.

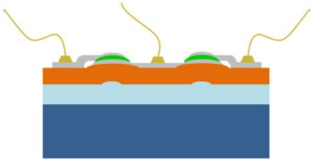

9. Removal via lift-off of resist and patterning of top electrodes. Wiring and parylene C coating for isolation.

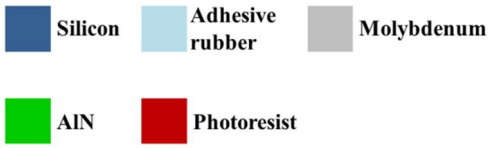

(Mastronardi V. et al. [123, 124])

Finally, the top Mo thin metallization, with a thickness of 300 nm, has been deposited at room temperature via DC sputtering, after cooling down the deposition chamber (whose

temperature has increased during previous AlN deposition till 250-300 °C) using the same deposition conditions of bottom electrode.

(a) (b)

Figure 4.3: a) Karl Suss mask aligner used during photolithography; b) ICP tool for the inductively coupled plasma etching of the metal and piezoelectric thin films.

After rinsing the sample, AZ5214E image reversal resist for high resolution has been used as soft positive tone mask during etching process (step n° 3). The positive resist has been deposited by spin coating, keeping the substrate in rotation for 40" at 2000 rpm in order to uniformly spread it on the wafer surface; double drop deposition and double spinning have ensured the proper thickness of the photoresist (about 2.3 – 2.5 μm) in order to withstand the etching process. The resist has been cured on hotplate by soft bake at 90 °C for 120'' and it has been exposed for 55'' with UV light source – the wavelength of the UV light being 365 nm – using a Karl Suss mask aligner (MA6, SUSS MicroTec AG). In this way, the total provided dose has been 660 mJ/cm^2, being the exposure intensity of the UV lamp equal to 12 mW/cm^2. The photolithographic process has been delivered by keeping the photolithographic mask in soft contact with the surface of the sample (with a separation gap of 250 μm for the alignment). The equipment used for the photolithography is displayed in Figure 4.3a. Finally, a bath in AZ726 MIF developer for 50'' at room temperature has allowed developing the photoresist.

Afterwards Mo and AlN layers have been etched in circular shape by inductively coupled plasma process (STS ICP, SPTS Technologies, Orbotech company), having the chlorine-based gas mixture the following parameters: $SiCl_4$ 20 sccm/N_2 25 sccm/Ar 7 sccm. The platen power has been 45 W (to promote the anisotropy of the etching), with a temperature of 10°C that has guaranteed the appropriate verticality of the etching, whereas the coil power has been 100 W (step n° 4). A pressure of $13.3 \cdot 10^{-3}$ mbar has been used. Typical etching time, required to complete the removal of the first two layers of Mo and AlN, has been about 180 – 200 seconds (this time has been optimized in order to avoid the removal of the bottom metallization). A conditioning of

etching chamber with the same chlorine-based gas mixture for 300'' has been carried out to contribute to a chemically stable etch environment and make etch conditions as reproducible as possible.

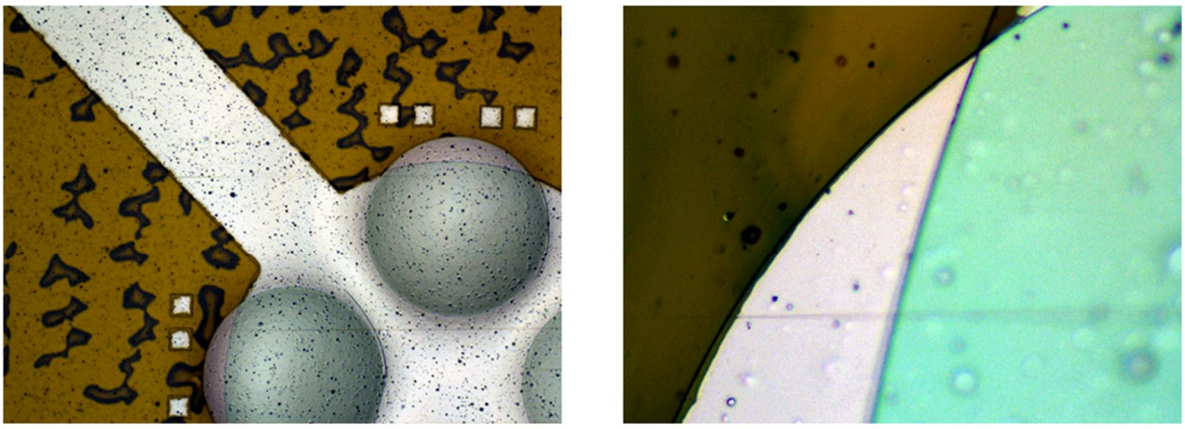

(a) (b)

Figure 4.4: a) Optical image of the circular domes after dry etching of top Mo and AlN layers and wet etching of common ground; b) magnification of dome section in which the under etching of the metallization is distinctly visible (the resist has not been still removed).

The equipment used for etching processes is displayed in Figure 4.3b. The chlorine based etching is not selective with regard to the photoresist, such that to avoid etching the AlN layer, top molybdenum has been used as hard masking, although a small portion of top molybdenum is removed (as already shown in Figure 4.1, steps 2 and 3), reducing its final thickness. A subsequent deposition of the top metallization is then needed to achieve the required thickness for the final top electrode.

The Mo bottom common electrode has been patterned, after second masking photolithography (steps n° 5 and 6 of Table IV.1) exploiting the same AZ resist, through a wet etching with hydrogen peroxide solution (H_2O_2 – 30%) for longer time than required to deliberately over etch the metal film under the AlN circular region and to prevent short-circuiting between bottom and top metallization. An optical image of domes in representative sample, after patterning of circular geometries and bottom metallization as common ground electrode, is depicted in Figure 4.4.

The releasing of the total compressive residual stress of AlN (and, partially, Mo) on kapton generates a visible dome-shape structures (Figure 4.4a). Moreover, from this picture, it is clearly visible the under etching of the bottom metal electrode (see Figure 4.4b). Afterwards, the sample have been rinsed again and dried with nitrogen flow. Then, in order to define the top electrodes, lift-off metallization patterning has followed.

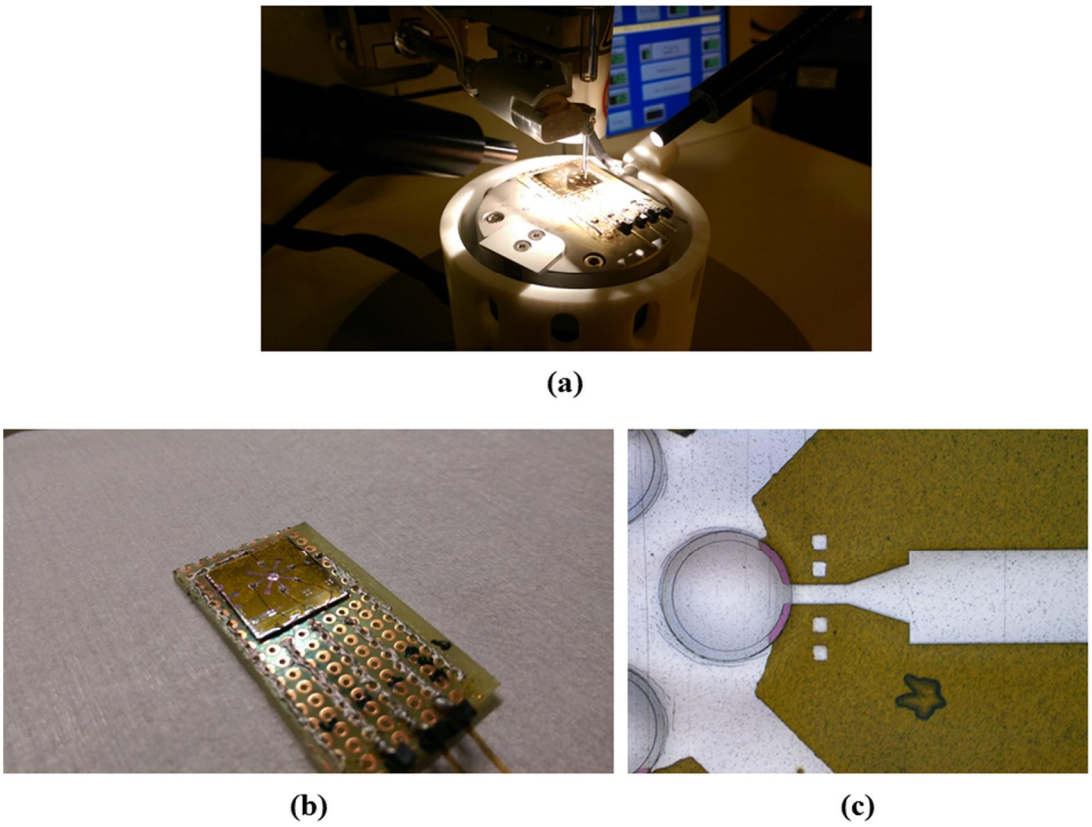

Figure 4.5: a) Assembling and bonding of the prototype on a perforated board b) Final prototype containing the quartet of dome; c) single DSDT cell with metal connections.

The already described AZ negative tone resist [123, 124] (steps n° 7 and 8 of Table IV.1) deposition and patterning has been repeated. In order to invert the tone of the photoresist, a post bake at 100 °C for 120'' has been carried out, followed by a final exposure without masking for 150''. The total provided dose has been then 1800 mJ/cm^2. The process, just mentioned, is extremely simple and, especially, compatible with the common microfabrication tools used in semiconductors foundries [79, 100]. Then, a 250 – 300 nm-thick molybdenum top metallization has been deposited by sputtering (from high-purity Mo target) at room temperature and the lift-off in acetone bath successfully followed.

Finally, the sample containing four elementary piezoelectric curved diaphragms of radius equal to 350 µm has been bonded to a testing platform with plated holes where connectors have been soldered for the electrical characterizations. Wire bonder (TPT Wire Bonder GmbH & Co. KG) and conductive silver paste have been used to connect the electrical pads to the perforated circuit board. The representative final prototype, after the assembly on the perforated circuit board and containing an array of 2x2 domes (placed at centre of the sample), is displayed in Figure 4.5. The magnification (Figure 4.5c) shows the single DSDT cell with top and bottom metal connections. In order to prevent external mechanical damages and to electrically isolate the piezoelectric transducers, a final parylene C coating of 1 µm has been deposited via Room-Temperature CVD deposition. The conformal nature of the parylene C coating, deposited by CVD,

allows enhancing the electrical and mechanical isolation of the device. Moreover, connection vias have been opened in the parylene C coating, in order to guarantee electrical connections to the perforated circuit board.

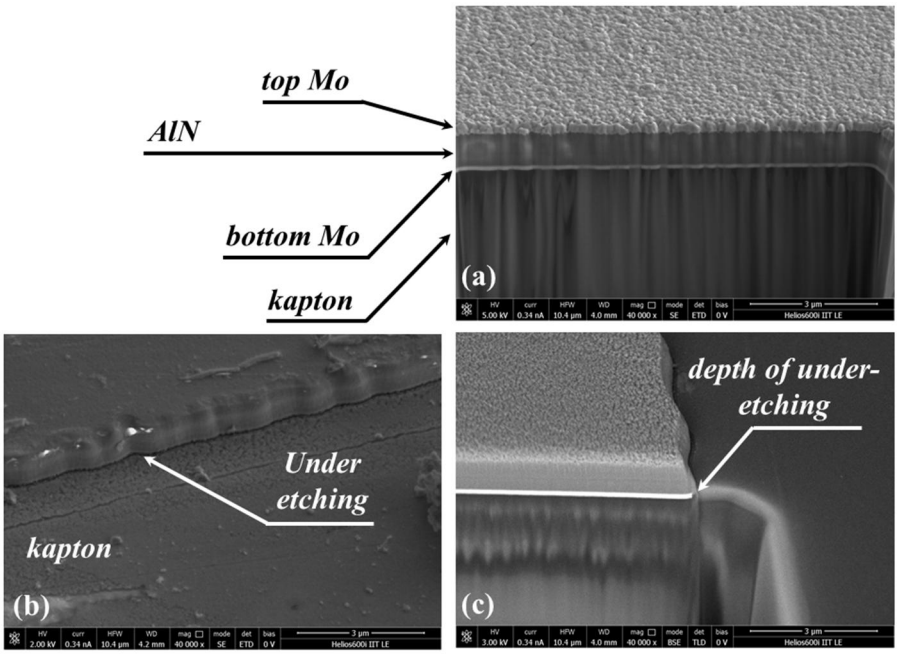

Figure 4.6: Scanning electron microscopy (SEM) image of (a) Mo/AlN/Mo stacked layers deposited on kapton substrate; (b) front view and (c) cross-section of the undercut of molybdenum common ground.

Displacement versus applied voltage response, achieved by piezoresponse force microscopy, has shown an averaged effective piezoelectric strain coefficient d_{33} of 4.7±0.1 pm/V, whereas the piezoelectric strain coefficient d_{31} has been assumed to be 2.35 pm/V [122].

Additional SEM images of the layers deposited on kapton, showing the undercut of the molybdenum metallization performed by H_2O_2 wet etching are displayed in Figure 4.6. The undercut has been estimated about 110 nm.

Finally, profile inspection has been performed to know the maximum height of the dome after the natural stress relaxation. 2D and 3D profile scanning has been performed by Dektak XT™ stylus profiler (Bruker corp.). The profilometry shows that the compressive stress is released in curved domes and an up-lifted annular region around, as shown in Figure 4.7. These measurements suggest a different detachment of the dome from the silicon substrate. As a consequence, different empty space has been supposed to be between polyimide and silicon substrate, with a larger annular region for the higher domes and a smaller annular region for the lower domes.

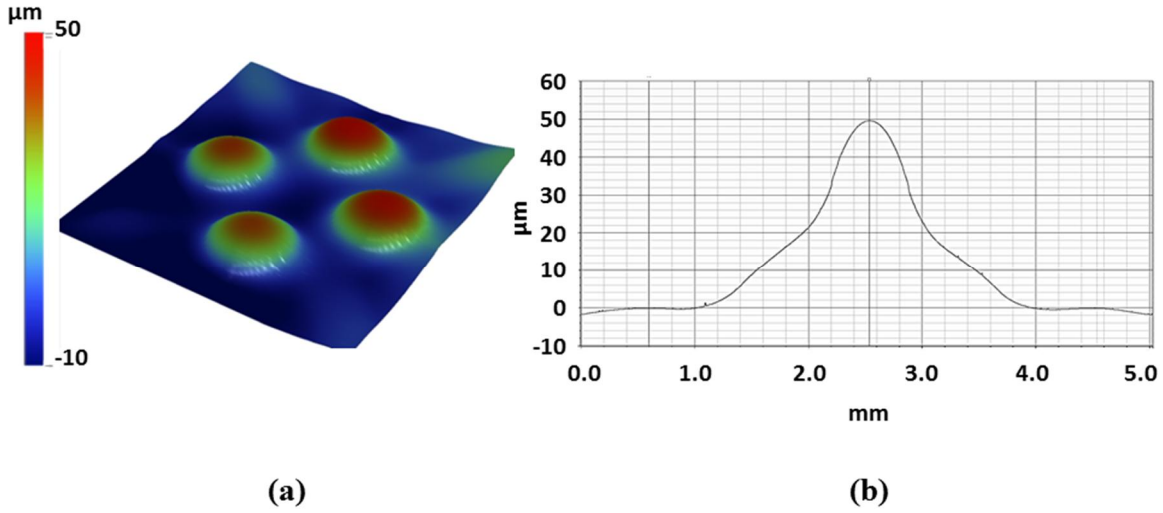

Figure 4.7: 3D profile mapping of the 2x2 array of domes and b) 2D profile of the single DSDT.

4.2. EFFECTS OF AlN RESIDUAL STRESS

The modelling of the elastic deformation generated by the residual stress of the AlN on the substrate below has been used to study and evaluate the dependence of geometrical features of the three-dimensional DSDT on residual stress. For this purpose, representative domes which differentiate in terms of nominal radius and extension of the uplifted region as well as radius of curvature have been analysed. Domes obtained from dissimilar microfabrication processes (even if the conditions of films growths have been kept unchanged) and with nominal radius r_E = 250, 275, 300 and 350 µm have been investigated (for the purpose of this study, the domes are called with the label DOME followed by the value of the nominal radius). The radius of curvature of these domes has been estimated by experimentally measuring the maximum height h_{max}. The corresponding geometrical parameters of all the representative domes of both the processes are reported in the Table IV.2 as well as the results of the calculation.

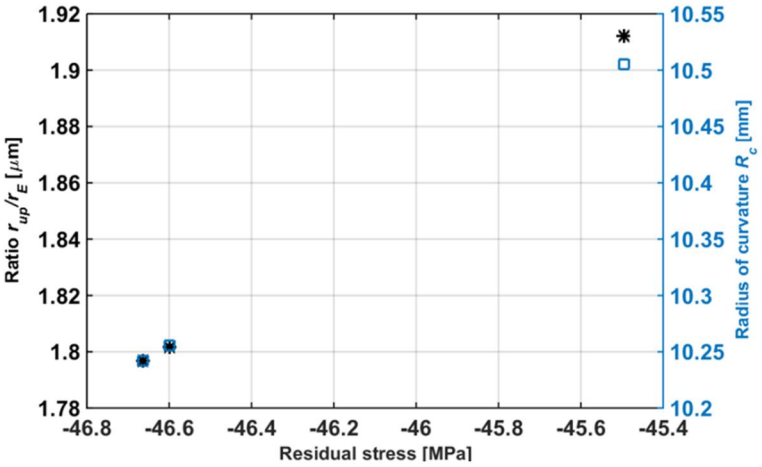

(a)

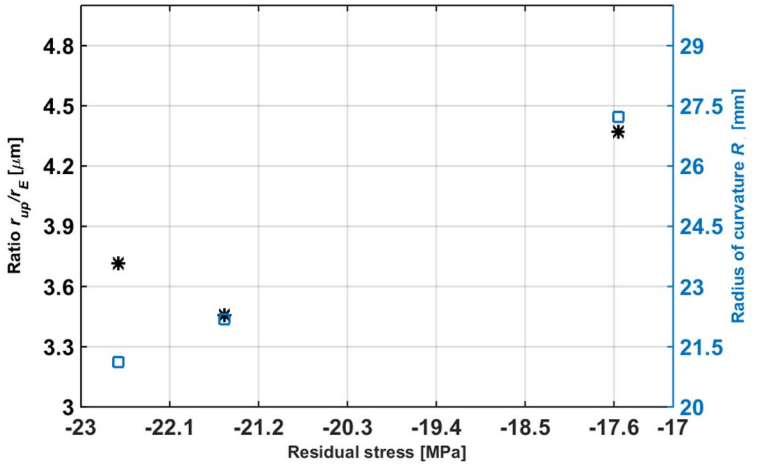

(b)

Figure 4.8: The geometrical ratio r_{up}/r_E and the radius of curvature are studied with respect to the residual stress for curved membranes with nominal radius a) 250, 275, 300 μm and b) 350 μm, respectively.

These results are also displayed in the graphs of Figure 4.8a and b, where the geometrical ratio r_{up}/r_E and the radius of curvature are plotted as a function of the average residual stress – according to the classical convention, the minus sign of $\bar{\sigma}_{AlN}$ points out a compressive stress.

An average residual stress of the AlN has been estimated, when the first-order approximation is taken [124], and it amounts to -46.3 ± 0.66 MPa for the sample whose process conditions have produced smaller domes and -20.5 ± 2.6 MPa for the sample whose process conditions have produced larger domes. Since the release of domes is not totally controlled during the microfabrication processes, the samples have shown, as in the Figure 4.8, different deformations, underlying a dependence of the geometrical features of the three-dimensional structures on residual stress.

Table IV.2

Geometrical parameters of the domes after the partial release and corresponding residual average stresses $\bar{\sigma}_{AlN}$

Sample label	Nominal radius r_E [µm]	Uplifted radius r_{up} [µm]	Maximum height h_{max} [µm]	Radius of curvature R_c [mm]	Residual stress T_{res} [MPa]
DOME250	250	382	6.9	10.5	-45.5
DOME275	275	404	8.0	10.2	-46.7
DOME300	300	450	9.9	10.3	-46.6
		1530	43	27.2	-17.6
DOME350	350	1300	40	21.1	-22.6
		1210	33	22.2	-21.5

4.3. DSDTs ELECTRICAL CHARACTERIZATION

Electrical characterization has been performed to determine capacitance, impedance of the DSDTs and the relative dielectric constant of sputtered AlN piezoelectric film.

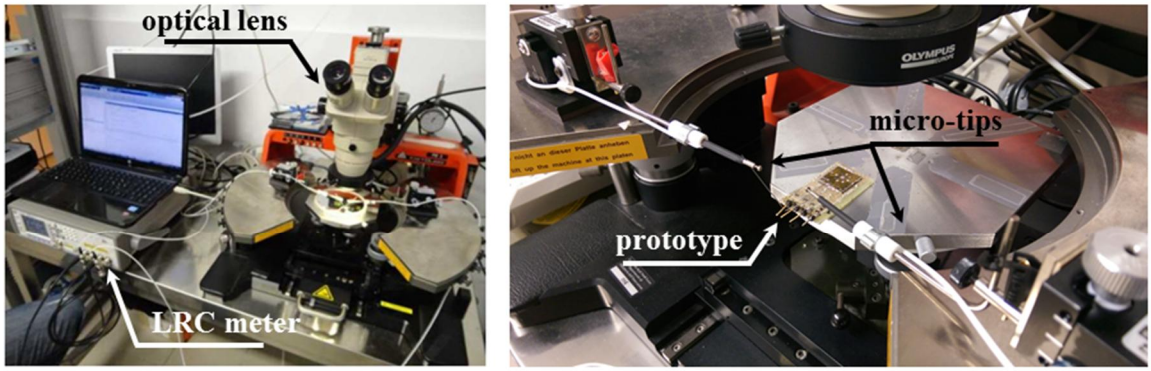

Figure 4.9: a) The DUT has been placed on a probe station and b) a proper connection has been achieved by using high resolution micro-manipulated tips.

Embedded between metal electrodes, the three-layered stack can be assumed to be a metal-insulator-metal (MIM) structure. For this reason, capacitance measurements have been performed by precision LCR meter E4980A (Agilent Technologies) at a testing frequency of 1kHz and by applying a source AC voltage with 3 volts of amplitude, the DSDT working like a parallel plate

capacitor. The measurement tool has been set in parallel circuit mode, which is the mostly used configuration when a measurement of small capacitance values is required.

The capacitance has been measured for each individual DSDT, having the aluminum nitride cells a nominal radius of 350 μm. To this aim, micro-tips have been used to electrically connect the prototype to the measurement tool. An accurate control of micro-tips position has been achieved by using high resolution micro-manipulators, whereas the prototype has been placed on a probe station (PM5, Karl Suss), as displayed in Figure 4.9. The measured average capacitance of parallel plate capacitors based on AlN piezoelectric film is 38.9 ± 1.0 pF, from which the dielectric constant has been calculated. Considering that the measured thickness of the micromachined membranes is equal to ~1 μm and the circular surface area, $A = \pi r_E^2$, is equal to 0.384 mm^2, the corresponding measured dielectric constant of the aluminum nitride has been estimated about ε_{AlN} = 10.2 ± 0.34 at 1 kHz and applying 3 volts as supply voltage, which is consistent with typical values reported in the literature [125-127].

The dielectric constant is an important parameter for the characterization of the piezoelectric thin film. Indeed, the output voltage generation of the device as a sensor is inversely proportional to the open circuit capacitance C_{oc} as well as the capability to translate an electrical input signal in mechanical displacement as an actuator (electrically charged) relies on the amount of energy stored in the piezo actuator that is directly proportional to C_{oc} [128].

Electrical impedance and resistance of the DSDTs have been also measured exploiting the same AC voltage signal with 3 volts amplitude and frequency of 1 kHz. Table IV.3 summarizes the electrical characterization of the representative prototype (in the table the domes are labelled DOME-A, B, C and D).

Table IV.3

Measured electrical properties of the domes with 350 μm of nominal radius at 1 kHz and applying an *AC* voltage signal with 3 volts of amplitude

DSDT label	Capacitance C_{oc}[pF]	Impedance *I* [MΩ]	Phase ϕ [°]	Re(*I*) [kΩ]	Im(*I*) [MΩ]
DOME-A	38.35	4.15	-89.21	57.3	-4.15
DOME-B	38.31	4.15	-89.51	35.4	-4.15
DOME-C	37.93	4.19	-89.45	39.9	-4.19
DOME-D	37.89	4.20	-89.45	39.7	-4.20

4.4. DSDT-LIKE AS ACTUATOR: RESONANCE FREQUENCY AND DISPLACEMENT MEASUREMENTS

In order to investigate the mechanical behaviour of the curved circular transducers, a characterization of the flexural deflection modes of the membranes has been performed. To this aim, the natural frequency of vibrations and the corresponding displacements have been measured by a Laser Doppler Vibrometer (LVD Polytec MSA-500 Micro System Analyser) applying a suitable oscillating voltage.

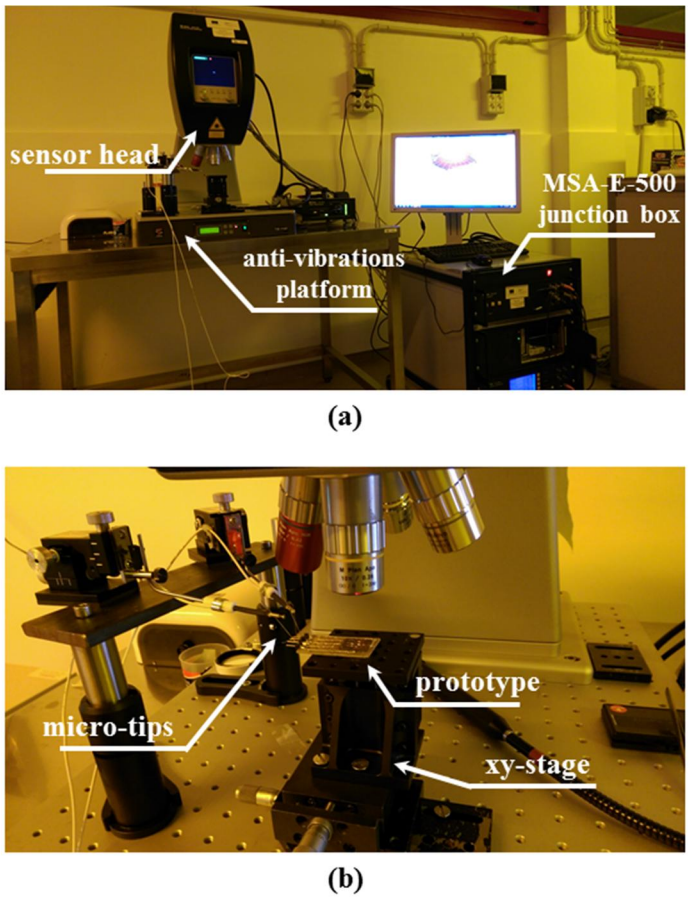

Figure 4.10 a) Laser Doppler Vibrometer (MSA-500 Micro System Analyser) equipment used to monitor the out-of-plane displacement of the DSDTs; b) typical measurement set-up.

The LDV analyser uses a Helium Neon (HeNe) laser source at 633 nm, with a micron-sized laser spot. It is mainly used to measure, through non-contact method, three-dimensional shapes and motions of microstructures, in static and dynamic configurations. The laser beam is focused on the surface to be investigated and Doppler Effect is exploited to calculate the velocity of the vibrations by detecting the frequency shift of back scattered light from the moving surfaces. Knowing the wavelength of the beam, the vibrometer is able to determine, by measuring the

Doppler frequency shift, the component of the velocity (or the acceleration) which lies along the axis of the laser beam generated by hit object. An appropriate interpolation technique allows the vibrometer to calculate the displacement with a resolution in the order of picometers. Therefore, LDV is suitable for the purpose of electromechanical characterization of piezoelectric transducers.

The DSDT membranes have been fixed on an anti-vibration platform and an x/y stage in order to move the prototype in plane directions. The sensor head with optimized microscope optics and a suitable magnifying lens has been used to drive the focused laser and to hit the DSDT target. Figure 4.10 shows the prototype, fixed on the stage mover, and the LDV MSA-500 tool used for the experimental evaluation of the dynamic response.

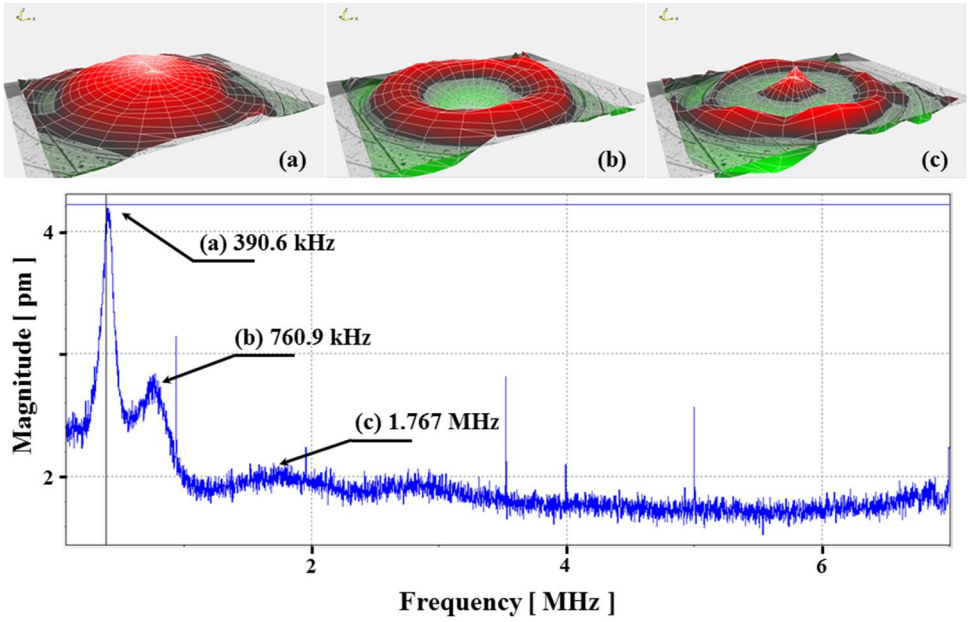

Figure 4.11: Frequency spectrum of driven DOME-A when a periodic chirp signal of $3V_{pp}$ amplitude is applied. The first three mode-shape functions are displayed at frequencies a) $f_{0,1}$= 390.6 kHz, b) $f_{0,2}$= 760.9 kHz and c) $f_{0,3}$= 1.767 MHz.

The DSDTs have been periodically driven with a sine signal exploiting the reverse piezoelectric effect by applying an external electrical excitation with voltage amplitude of $3V_{pp}$, while the corresponding out-of-plane displacement of the circular active region has been measured in air. The differential fibre optic interferometer (Polytec OFV-552) has been used to focus on the device two different laser beams: the measuring and the reference laser. The reference laser beam has been directed on a part of the chip surface that is supposed to be unable to move and far enough from the actuated piezoelectric DSDT. The measuring laser beam, instead, has been directed on the piezoelectric driven dome. The corresponding differential signal, obtained as subtraction of the measured and the reference back scattered laser, allows removing potential spurious displacement due to ground noises. A circular grid, made of proper spaced points, has been used to scan the

surface of the piezoelectric domes. The analog input voltage signal has been provided by an integrated signal generator, remotely controlled by the MSA-E-500 junction box.

The resonance frequency of the transducer has been studied by monitoring the out-of-plane displacement profile amplitude in a frequency range from few Hz up to 7 MHz. The resonances of DSDTs with nominal radius r_E = 350 µm have been identified and the corresponding operational deflection shapes have been reconstructed. The LDV measurement results, illustrated in Figure 4.11, show that the fundamental (0, 1) mode (still analysed in Chapter III by FEM simulations and theoretical model) has a most intense peak at resonance frequency of about 390 kHz – DOME-A and DOME-B have been used as reference for the experimental evaluation. For the DOME-B the peak of resonance is about 420 kHz. Moreover, the capability of the LDV to detect very small vibrations has allowed measuring the displacement at higher order resonance frequencies, such that the mode-shape functions (0, 2) and (0, 3) have been also detected (as in Figure 4.11b and c) and the corresponding three-dimensional shape has been recreated.

Furthermore, the three-dimensional recreation of the out-of-plane deflections shows that the operational deflection shape corresponding to the first mode of resonance has a Gaussian-like shape where the maximum displacement is achieved at membrane centre. The significant amplitude of displacement at mechanical resonance frequency is an effect of the piezoelectric film characteristics. When an alternating electric field is applied along the axis of the piezoelectric crystal, it expands and contracts (along this axis). If the frequency of the applied electric field approaches the natural frequency of the longitudinal vibrational mode of the crystal and matches with it, the amplitude of the mechanical vibration of the membrane become more significant. In Table IV.4 FEM, theoretical and experimental values of resonance frequency are resumed and compared, focusing on the fundamental resonant mode (0, 1).

We also explored the effects of driving the resonant membranes with a voltage that increase from 1 V_{pp} to 10 V_{pp} with 1 V_{pp} increment.

Table IV.4

Comparison of the FEM, thepretical and measured resonance frequencies of the (0, 1) mode

DSDT label	FEM calculation [kHz]	Theoretical calculation [kHz]	Exp. measurements [kHz]	Exp./FEM differential error [%]	Exp./Theoretical differential error [%]
DOME-A	408.6	384.9	390.6	4.6	1.5
DOME-B	408.6	384.9	420.0	2.8	8.3

The displacement has been measured by performing a single scan point, with the laser beam focused on the centre of the DSDT membrane and by applying a sinusoidal voltage (still

generated by the LDV junction box (MSA-E-500-M4)) at the measured resonance frequency of the first vibrational mode (0,1). The measured displacement for the DOME-A and DOME-B is shown in Figure 4.12. The maximum displacement achieved by the membrane is reported and it amounts to 2.00 nm for the DOME-A and 1.5 nm for the DOME-B, when the drive voltage is 10 V_{pp}. Despite the DSDT micromembranes are not free standing and are still attached on the silicon support – the membrane has been assumed to behave as a fully-clamped diaphragm – the actuation is quite efficient. Moreover, measurements show that the amplitude of the displacement increases linearly with the actuation voltage; up to 10 V_{pp}, no deviation from linearity is observed.

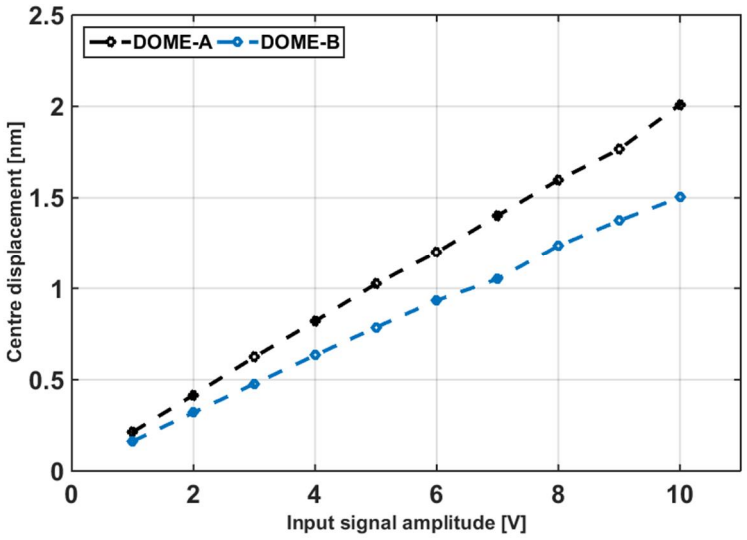

Figure 4.12: Centre displacement peak amplitude at resonance frequency $f_{0,1}$ for the DOME-A and DOME-B, measured as a function of the drive voltage amplitude.

4.5. DSDT-LIKE AS SENSOR: STATIC AND DYNAMIC IMPULSIVE FORCES MEASUREMENTS

Being developed for tactile sensing purpose, the proposed technology has been tested in order to explore the electromechanical response of the device when impulsive dynamic and/or long static forces are applied. The study on the impulsive dynamic and long static stimuli detection has been performed by using the XYZTEC Condor EZ push and pull system (XYZTEC, Netherlands) and connecting the transducer electrical terminals to the Tektronix MDO4000 oscilloscope (Tektronix Inc.).

The condor system consists of an x/y stage basis and a moving (upward and downward) z stage. A revolving measuring unit (RMU) is mounted on the z stage and an object work-holder is mounted on the x/y stage to firmly fix the device under test. Load has been applied with a stainless

steel cylindrical straight rod, whose diameter is 1 mm. The rod has been mounted on the RMU which has been moved downward, with well-known approach velocity, up to push on the single DSDT. The steel pushing probe is directly connected to a force gauge to simultaneously measure the applied impulsive force (expressed in kgf). The force gauge is able to detect reaction forces from 0.49 mN to 490 mN. Figure 4.13 shows the apparatus to apply the load and to evaluate the output voltage response of the DSDT transducers. The picture also includes the measurement equipment (the oscilloscope for the voltage response measurement will be replaced with the LCR meter for capacitance measurement, as illustrated in this section).

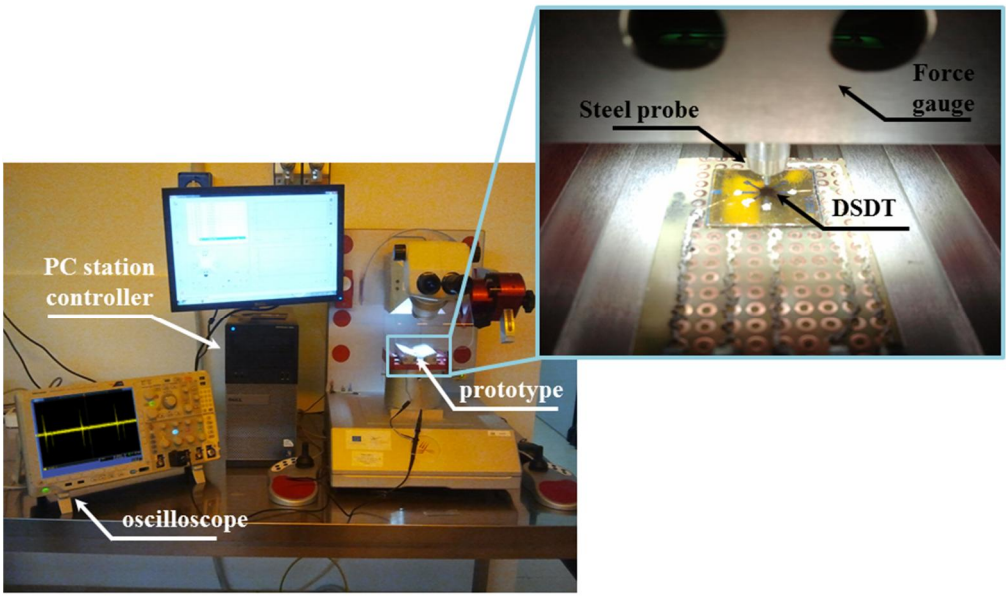

Figure 4.13: The apparatus to evaluate the output response of the transducers. The peak voltage is measured with the oscilloscope, whereas the capacitance variation is measured with a precision LCR-meter (not in picture).

Before starting the load test, the frame stiffness has been measured. As the experimental measuring setup is not infinitely stiff, some of the displacement that occurs during the tests can be due to the deformation of the tool. The measurement of the frame stiffness has been than carried out using a highly thick steel plate that has compliance several orders of magnitude higher than the tool. The steel rectangular plate has the following size: l = 10 cm, w = 5 cm and t = 5 mm, where l, w and t are the length, the width and the thickness of the plate, respectively. This plate being extremely stiff, it has been supposed that the forced deformation occurs in the frame system and not in the plate, allowing determining the compliance of the test setup. The RMU has been moved with an approach velocity of 80 μm/sec, whereas it has been held on the plate for 1 sec (the resolution of the RMU motion has been set as 1 μm). The initial non-linearity, which typically arises from the slack in the system, has been removed approximating the linear part of the frame calibration curve by a linear regression. The x-intercept value of the corresponding linear fit has been extracted and it has been subtracted to the measurement curve. From this initial frame

calibration, a stiffness value of 55.6 N/mm has been measured. Being this value supposed to be much higher than the device's stiffness, it can be assumed that the reported deformation occurs in the dome-shaped structures and not in the measurement set-up. Once the compliance of the frame has been known, the measurements have been corrected taking into account the deformation occurring inside the tool during the load test. For this purpose, the compliance of the tool has been subtracted from the measured deformation of the domes, considering that the tool deformation is equal to the applied load multiplied by the compliance of the system. The actual deformation of the DUT becomes

$$\delta_{DOME} = \delta_{meas} - F \cdot C_T \tag{4.1}$$

where δ_{DOME} is the deformation of the DSDT, δ_{meas} is the measured deformation and $F \cdot C_T$ is the deformation of the frame, being F the applied load and C_T the compliance of the frame, respectively.

Two representative dome-shaped devices, DOME-A and DOME-B, distinguished from different releasing height, have been electrically characterized. The relationship between the electromechanical response and the individual stiffness of each dome due to the different shape has been than investigated. Load has been applied by the same setup used for the calibration of the frame system. In Figure 4.14, the electrical characterization results are plotted; the output voltage at the peak is reported as a function of the applied forces, both for Dome-A and Dome-B transducers. Each data point is the average of three measurements with the same force and penetration depth, collected at a frequency of 0.3 Hz – with approach velocity of the pushing probe of 600 μm/s and hold time of 200 msec. The electromechanical behaviour of both the domes is similar and it is due to the combination of piezoelectric and flexoelectric effects. For Dome-A, an offset of 18 mV in the measured voltage has been observed. The Dome-A shows an increase of generated voltage in a dynamic range of [0–60 mN], while Dome-B dynamic range is characterized by a linear increase up to 40 mN, starting from the minimum detected force of 20 mN; a lower offset has been observed. For higher applied forces, both devices start to saturate when the force reaches the threshold value of ~60 mN for Dome-A and ~40 mN for Dome-B, respectively. The voltage range generated from Dome-A shows a maximum value of ~50 mV and from Dome-B ~25 mV; a sensitivity of approximately 480 mV/N and 445 mV/N in the linear dynamic range before saturation is observed, respectively.

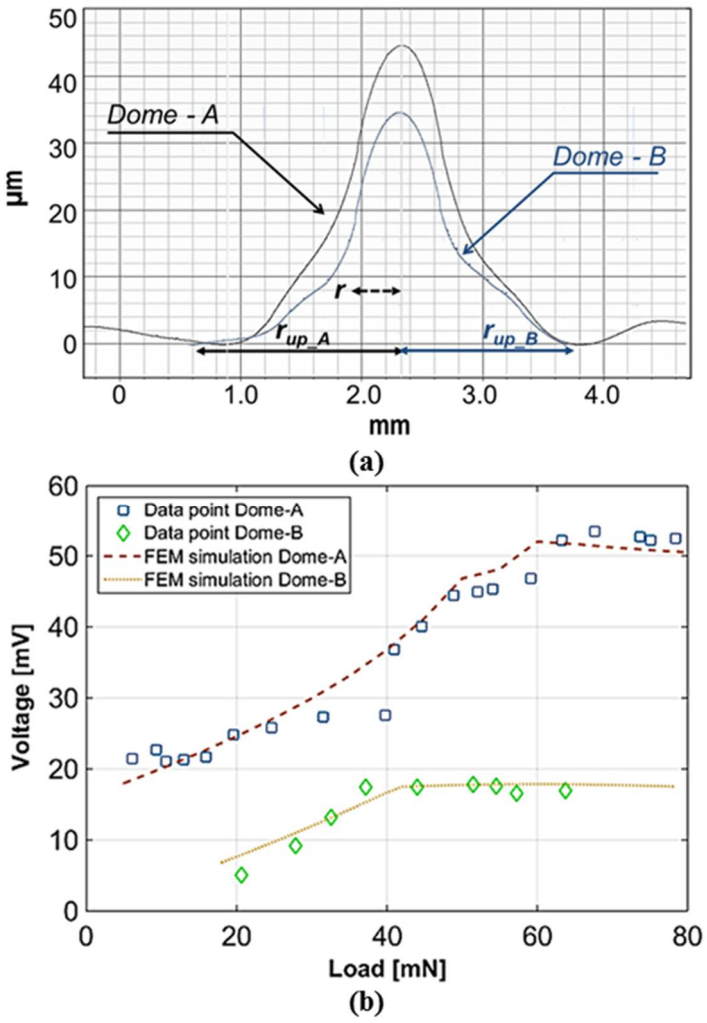

Figure 4.14: (a) 2D profile of Dome-A and Dome-B; r_E, r_{up}, and maximum height h_{max} are listed in Table IV.4. (b) Measured voltage output for Dome-A and Dome-B. Data points refer to measured values and dot lines are the FEM simulation results.

The minimum force detected is ~1.2 mN. In Figure 4.14b, the measured output voltage is compared with the FEM results superimposing the normalized calculated voltage to the measured signal. From a qualitative point of view, the measured results match well with the FEM simulations (see section 3.2.2 of Chapter III).

The detection of long static stimuli has been experimentally observed as capacitance decrease ΔC at increasing forces (the setup has been kept unchanged). The capacitance variation ΔC has been collected by the precision LCR-meter (Agilent E4980A). The results are reported in Figure 4.15 as the modulus of ΔC, with an initial measured capacitance of 43.9 pF for Dome-A and 41.6 pF for Dome-B, when no load is applied (a slight increase of about 5,5 – 3.3 pF from the initial capacitance has been detected after first load testing cycle, see section 4.3). For each point, the displacement of the z-axis stage has been slowly increased with a step resolution of 1 µm up to a total depth of 25 µm. Each data point is the average of three measurements with the same force

and penetration depth. The approach velocity of the probe, held on the sensing element for 1 sec, is 10 µm/s.

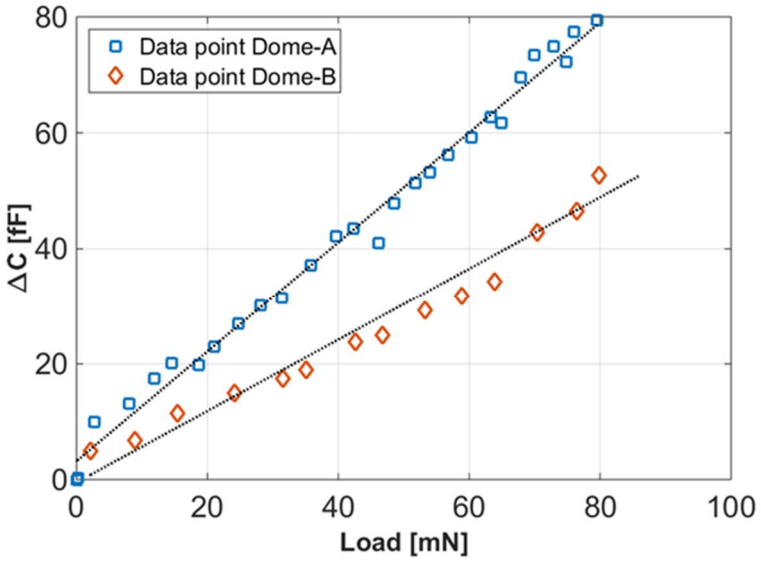

Figure 4.15: Relationship between applied force and capacitance decrease ΔC for the long static stimuli detection.

The capacitance variation has been observed for the whole interval of application of the stress and it does not decay with time; therefore, static forces detection is possible in the same system, making the AlN thin film in dome structure a multifunctional material. The DSDTs have shown a significant response to long static stimuli in the force range up to 80 mN, in which the achieved sensitivity in static sensing mode has been evaluated as 950 fF/N for Dome-A and 620 fF/N for Dome-B.

The shape and the mechanical stiffness of the structure are the reference parameters useful for explaining the electromechanical response of the transducers. The dome structural stiffness, considered as resistance to bending of the tetra-layered domes, has been measured through the XYZTEC push tester. In this test, the z-axis stage has been moved down with a velocity of 10 µm/s. Stiffness k_s as a structure property has been, therefore, assessed as the slope of the load-deformation curve and it has been extracted as the slope of the linearly fitted load-depth curve of loading, up to 80 mN. In this deformation region, results show a stiffness of $k_{sA} \simeq 3.5$ N/mm for Domes–A and $k_{sB} \simeq 9.7$ N/mm for Dome–B. Despite extreme flexibility, the Mo/AlN/Mo multi-layered structure results to be robust even after several cycles of bending by virtue of peculiar mechanical properties derived from the combination of materials with different elasticity. Table IV.4 summarizes the geometrical parameters, the measured stiffness and the normal stress sensitivity. The low value of k_s, compared to the stiffness of bulk materials included in the structure, is not only due to the fabricated tetra-layered structure but also due to the part of the surrounding polymer that is uplifted by the differential shrinkage. Therefore, the structure

compliance can be split in the sum of two contributions with the central area treated as a fixed membrane and the outer area as an annular membrane, fixed in the outer edge and guided in the inner edge. The overall displacement can be expressed considering the compliance as the series of both contributions [129]

$$y = F\left(\frac{r_E^2}{16\pi k_i} + c\frac{r_{up}^2}{k_{up}}\right) \tag{4.2}$$

where *k* is the bending stiffness, according to the simple membrane model

$$k = \frac{Et^3}{12(1-\nu^2)} \tag{4.3}$$

with the subscripts *i* for the inner part and *up* for the uplifted region; *F* is the applied load, *c* is a correction parameter adjusted to the ratio r_{up}/r_E. Despite the simplicity of the model, the values of modelled stiffness, namely, k_{sA_model} = 3.1 N/mm and k_{sB_model} = 8.2 N/mm, are in reasonable agreement with the measurements of both A and B systems ($\Delta k_A \simeq 13\%$ and $\Delta k_B \simeq 18\%$), as still summarized in Table IV.5.

Table IV.5

Measured geometrical parameters r_E, r_{up} and h_{max}, measured stiffness k_s and dynamic (SI_d) and static (SI_s) normal stress sensitivity.

DSDT	Radius r_E [µm]	Uplifted radius r_{up} [mm]	Maximum height h_{max} [µm]	Stiffness k_s [N/mm]	Dynamic stress sensitivity SI_d [mV/N]	Static stress sensitivity SI_s[fF/N]
DOME–A	350	1.53	43	3.50	480	950
DOME–B	350	1.21	33	9.70	445	620

The effect of the uplifted area size is clear from equation (4.2): the larger the radius of the outer area, the lower the stiffness of the dome as a whole allowing an electromechanical response of the piezo-cells Dome–A at low forces (6–20mN), as shown in Figure 4.14b. In the same range, due to the higher stiffness of Dome–B, no electromechanical response (both piezo- and flexo-polarization) is measured while load is applied. Analogously, the stiffer Dome–B shows a lower capacitance variation with respect to Dome–A (Figure 4.15).

According to the previous results, it can be asserted that the fabricated DSDT cells exhibit enhanced transduction response within a full scale range of 80 mN (~200 kPa) both for dynamic

and static load. No additional power supply is required to provide the electrical readout signals in dynamic sensing mode whereas low DC voltage source (3 V) is sufficient as supply for reading a significant capacitance variation. These properties make the proposed technology suitable candidate when low power consumption is demanding.

CHAPTER V

CONCLUSIONS AND OUTLOOKS

Artificial tactile systems for pressure and force measurements are important in many applications as automated assembling, minimal invasive medical procedures (MIS) for the evaluation of tissues stiffness and damages, prosthetic and orthotic devices where artificial skin restores the loss of tactile sensations. Similarly, humanoid robots need tactile interface for a safe interaction with humans in assisting activities. Equipping robots with specific sensors and transducers is a way to confer them sufficient autonomy to perform advanced tasks in unstructured environments.

In this thesis, flexible piezoelectric MEMS transducers based on aluminum nitride piezoelectric thin film grown on polyimide soft substrate by standard micromachining process and developed for tactile sensing purposes have been proposed. The devices are based on Mo/AlN/Mo/kapton tetra-layered structures, where AlN is the active piezoelectric material. The transducers are designed with bio-inspired approach to mimic the ability of human mechanoreceptors and to be sensitive to periodic impulsive mechanical stimuli, with sufficient sensitivity in a wide pressure range, up to 200 kPa, suitable for object manipulation. Moreover, the dielectric properties of the Mo/AlN/Mo stack, which behaves as a capacitor, allows to measure long static mechanical stimuli by a steady deformation of the convex structure. With together an appropriate arrangement of the single DSDT in 2x2 array configuration, the final device may be tailored for the replication of the ability of tactile mechanoreceptors in a multi-detection system by exploiting the same technology.

The individual transducer consists of circular micro-cells, namely dome-shaped diaphragm transducer or quite simply DSDT, with a nominal radius of 350 μm and made of polycrystalline highly *c*-axis textured aluminum nitride. The release of compressive stress by crystalline layers and active materials over polymer substrate generates uplifted domes with a natural three-dimensional bowed structure whose structural stiffness is well below the stiffness of composing materials, allowing an enhanced transduction response.

The design, the fabrication and the characterization of the innovative force/pressure delivery and sensing DSDT is described in this dissertation. On the basis of thorough Finite Element Method (FEM) study, the fabrication process is developed and measurements are also achieved for characterization purposes. Exploiting the dual capability of the piezoelectric aluminum nitride material, the curved membranes extend the range of applications from

force/pressure tactile sensing applications to piezoelectric micro-actuators. For these reasons, a characterization of the device both as sensor and actuator is performed.

An analytical model of the elastic deformation of the DSDTs has been used to study and evaluate the dependence of geometrical features of the three-dimensional bowed structure on aluminum nitride residual stress $\bar{\sigma}_{AlN}$ on the substrate. Representative domes exhibit different bowed structures such that higher value of $\bar{\sigma}_{AlN}$ of about -46.3 ± 0.66 MPa produces smaller domes and lower value of $\bar{\sigma}_{AlN}$ of about -20.5 ± 2.6 MPa produces larger domes.

As confirmed by FEM simulations, the uplifted area is determinant for low stiffness, for the dynamic range of the transducer that easily deforms under loading and for an enhancement of the actuation. The resonances of the individual curved diaphragms have been analysed and a qualitative study of the displacement, induced by the applied electric field, is carried out. This last analysis revels the voltage driven curved diaphragms have an improved electromechanical coupling with higher mechanical deformation per unit energy compared with the conventional plate structures. The improvement of electromechanical coupling is mainly due to the fact that dome-shaped transducers exploit in-plane piezoelectric strain, which leads to large out-of-plane deflection because of their spherical curvature and fully-clamped or ideally fully-clamped peripheries.

Standard micromachining techniques are used to fabricate the prototype, namely optical photolithography and dry and wet etching processes. A $SiCl_4$–based plasma is used during the etching process to pattern and shape the thin films with the desired geometries. A conformal layer of Parylene C is deposited as insulation covering film to reduce mechanical damages and to electrically isolate the device under test.

SEM and optical inspections on the morphological and structural properties of the piezoelectric thin film are performed, proving its crystalline structure and the quality of the adhesion on polymeric substrates.

Electrical characterization has been performed to determine capacitance and impedance of the metal-insulator-metal DSDT structures and the relative dielectric constant of sputtered AlN. From experimental measurements the dielectric constant ε_{AlN} = 10.2 ± 0.34 at 1 kHz is determined. This measure is consistent with typical values reported in literature.

As actuator, the transducers are characterized by investigating the flexural deflection modes and by monitoring the out-of-plane displacement profile amplitude of voltage driven membranes in a frequency range from few Hz up to 7 MHz. The resonances of DSDTs with nominal radius r_E = 350 µm are identified and the corresponding operational deflection shapes are reconstructed. The LDV measurement results show that the fundamental (0, 1) mode has a most intense peak at resonance frequency of about 390 kHz - 420 kHz. The effects of driving the resonant curved membranes with a voltage that increase from 1 V_{pp} to 10 V_{pp} with 1 V_{pp} increment are investigated. The maximum displacement ranges from 1.5 nm up to 2.0 nm for the larger dome, when the drive voltage is 10 V_{pp}. Despite the DSDT micromembranes are not free standing and are

still attached on the silicon support the actuation is quite efficient. Moreover, measurements show that the amplitude of the displacement increases linearly with the actuation voltage; up to 10 V_{pp}, no deviation from linearity is observed.

As force sensor, the transducers are used to detect dynamic contact forces, by exploiting the combination of both piezoelectric and flexoelectric effect in the range up to 60 mN before saturation as well as static contact forces (up to 1 s of applied mechanical load) by capacitance decrease in a range up to 80 mN. Furthermore, the estimated sensitivity to normal stress in dynamic sensing mode is up to 480 mV/N and in static sensing mode is up to 950 fF/N. The minimum force detected is ~1.2 mN.

Finally, the dome structural stiffness, considered as resistance to bending of the tetra-layered domes, is measured in a deformation loading range up to 80 mN. Low stiffness of ~3.5 N/mm for larger dome and ~9.7 N/mm for smaller dome are not only due to the fabricated tetra-layered structure but also to the part of the surrounding polymer that is uplifted by the differential shrinkage. This values are in reasonable agreement with the modelled stiffness, with a differential error of 13% and 18%, respectively.

According to the previous results, it can be assert that the fabricated DSDT cells exhibit good transduction response within a full scale range of 80 mN (~200 kPa) both for dynamic and static load. These results are encouraging and the technology is well suited to realize large area tactile sensors for robotics applications.

APPENDIX A

A.1 PIEZOELECTRIC EFFECT: MATHEMATICAL FORMULATION

Some basic mathematical formulation can describe the electromechanical properties of piezoelectric materials. Under ideal case, piezoelectric materials have a linear profile at low electric fields and at low mechanical stress levels [130]. According to the linear theory of piezoelectricity, the density of generated fixed charge in a piezoelectric material is proportional to the external stress. Owing to the anisotropic nature of piezoelectric materials, it is defined as the magnitude of the piezoelectric polarization vector P_{pe} [in C/m^2 units], which is equal to the fixed charge density produced after stress application as a result of piezoelectric effect: P_{pe} is proportional to the stress T [in N/m^2 units] to which piezoelectric material is subjected by the piezoelectric strain tensor [d] [in C/N units] or, alternatively, it is proportional to applied strain S [dimensionless] by the piezoelectric stress tensor [e] [in C/m^2 units]. If the indices i, j, k and l represent the three-dimensional Cartesian coordinates system of x, y and z, these relationships can be summarized as in the following equations (expressed in Stress-Charge and Strain-Charge forms and where the Einstein summation convention is valid):

$$\{P_{pe}\} = [d]\{T\} \Rightarrow P_{pe,k} = d_{kij}T_{ij} \qquad (\textit{Stress-Charge form}) \qquad \text{(A.1a)}$$

$$\{P_{pe}\} = [e]\{S\} \Rightarrow P_{pe,k} = e_{kij}S_{ij} \qquad (\textit{Strain-Charge form}) \qquad \text{(A.1b)}$$

(the '*pe*' subscript specifies the quantities generated by piezoelectric effect). In a similar manner, the reverse piezoelectric effect can be formulated by the following relationships (in both Stress-Electric field and Strain-Electric field forms and where the Einstein summation convention is valid):

$$\{T_{pe}\} = [e]^t\{E\} \Rightarrow T_{pe,ij} = e_{ijk}E_k \qquad (\textit{Stress–Electric field form}) \qquad \text{(A.2a)}$$

$$\{S_{pe}\} = [d]^t\{E\} \Rightarrow S_{pe,ij} = d_{ijk}E_k \qquad (\textit{Strain–Electric field form}) \qquad \text{(A.2b)}$$

where S_{pe} is the mechanical strain produced by the applied electric field E [in V/m units] according to reverse piezoelectric effect.

A.1.1 ELASTIC CONTRIBUTION

The piezoelectric phenomenon causes an increase of the material's stiffness. When the piezoelectric material is subjected to a strain *S*, two effects can arise: the strain will generate an elastic stress T_e that is proportional to *S* by the elastic constant tensor [c] and a piezoelectric polarization P_{pe}, according to the equation (A.1b). As a consequence, an electric field, internal to the material, will be generated by the polarization. This electric field E_{pe} is given by:

$$\{E_{pe}\} = \frac{\{P_{pe}\}}{[\varepsilon]} = \frac{[e]\{S\}}{[\varepsilon]} \Rightarrow E_{pe,ij} = \frac{P_{pe,k}}{\varepsilon_{ijk}} = \frac{e_{kij}S_{ij}}{\varepsilon_{ijk}} \tag{A.3}$$

where [ε] is the dielectric constant matrix of the material. The stress T_{pe} produced by the electric field E_{pe} and by the elastic origin is against the material's deformation. Consequently, according to the elasticity theory expressed by the generalized Hooke's Law, the stress generated by the strain *S* is:

$$\{T_e\} = [c]\{S\} \Rightarrow T_{ij} = c_{ijkl}S_{kl} \tag{A.4a}$$

or inversely

$$\{S_e\} = [s]\{T\} \Rightarrow S_{ij} = s_{ijkl}T_{kl} \tag{A.4b}$$

where [c] [in N/m^2 units] is the piezoelectrically stiffened constant matrix and [s] [in m^2/N units] is its reverse matrix, that is the compliance coefficients matrix.

A.1.2. DIELECTRIC CONTRIBUTION

Since piezoelectric materials are dielectrics, when an external electric field *E* is applied between the electrodes, an electric displacement is created toward them, generating an increase of surface charge density. The magnitude of this electric displacement is *D* = [ε]E. Moreover, the material is also piezoelectric; the electric field will produce a positive or negative strain (as in A.2b) – depending on the direction of the external electric field with respect to the poling field – and the material will undergo expansion or compression. The expansion or compression of material generates a voltage having opposite polarity to the external applied field. Consequently, the surface charge density increases if the direction of applied external field is opposite to that of the poling

field. The strain, due to the reverse piezoelectric origin, results in polarization and the surface charge density increases. Furthermore, if the electric field is kept constant, the additional polarization, due to piezoelectric effect, increases the electric displacement of free charges toward the electrodes. Therefore, the resulting electrical displacement is

$$\{D_d\} = (\varepsilon_0 + \chi)\{E\} + \{P_{pe}\} = [\varepsilon]\{E\} \Rightarrow D_{d,k} = (\varepsilon_0 + \chi)E_k + P_{pe,k} \quad \text{(A.5)}$$

where ε_0 is the vacuum dielectric permittivity ($\varepsilon_0 = 8.85\times10^{12}$ F/m), χ is the dielectric susceptibility of the material and $[\varepsilon]$ [in F/m units] is the effective dielectric constant matrix.

A.1.3. PIEZOELECTRIC LINEAR CONSTITUTIVE EQUATIONS

Although in practice piezoelectric materials exhibit nonlinear characteristics such as hysteresis, creep and other nonlinearities, piezoelectric constitutive equations can be found by assuming linear elasticity (stress-strain) and permittivity (dielectric displacement-electric field) relationships. By a cross-coupling between the elastic variables – stress *T* and strain *S* – and the dielectric variables – electric charge density *D* and electric field *E* – defined by the equations A.1 – A.5, the describing electromechanical equations for a linear piezoelectric material can be written as

$$\begin{cases} \{S\} = \{S_e\} + \{S_{pe}\} = [s]\{T\} + [d]^t\{E\} \\ \{D\} = \{P_{pe}\} + \{D_d\} = [d]\{T\} + [\varepsilon]\{E\} \end{cases} \quad \text{(\textit{Stress–Charge form})} \quad \text{(A.6a)}$$

$$\begin{cases} \{T\} = \{T_e\} + \{T_{pe}\} = [c]\{S\} + [e]^t\{E\} \\ \{D\} = \{P_{pe}\} + \{D_d\} = [e]\{S\} + [\varepsilon]\{E\} \end{cases} \quad \text{(\textit{Strain–Charge form})} \quad \text{(A.6b)}$$

A.1.4. MATRIX COMPRESSED NOTATION OF CONSTITUTIVE EQUATIONS

In order to determine the solution of piezoelectric (or elastic) problems, the arrays of material coefficients for particular symmetry of the material have to be known. So, for the sake of symmetry of strain and stress tensors, the compressed matrix notation turns out to be more useful than the consistent tensor notation.

Table A.1

Correlation between matrix indices and tensor double indices in abbreviated notation of subscripts

	xx	***yy***	***zz***	***yz* or *zy***	***zx* or *xz***	***xy* or *yx***
ij* or *kl	11	22	33	23 or 32	31 or 13	12 or 21
p* or *q	1	2	3	4	5	6

Thus, the tensor double indices (*ij*) and (*kl*) can be replaced by the matrix indices *p* and *q*, as specified in Table A.1 [53]. By virtue of the matrix indices, the linear constitutive equations can be expressed in compressed notation as:

$$\begin{cases} S_p = s_{pq}^E T_q + d_{pk} E_k \\ D_i = d_{iq} T_q + \varepsilon_{ik}^T E_k \end{cases} \quad \text{(Stress–Charge form)} \tag{A.7a}$$

$$\begin{cases} T_p = c_{pq}^E S_q - e_{pk} E_k \\ D_i = e_{iq} S_q + \varepsilon_{ik}^S E_k \end{cases} \quad \text{(Strain–Charge form)} \tag{A.7b}$$

In the last equations, the superscripts state that those quantities are measured at constant stress ($T = 0$), constant strain ($S = 0$) and constant electric filed ($E = 0$). The above equations can be re-written in a form which is often used for applications that involve sensing, by considering the matrices of coupling coefficients $[g]$ and $[q]$ for stress-voltage and strain-voltage forms, respectively:

$$[g] = [\varepsilon^T][d] \tag{A.8a}$$

$$[q] = [\varepsilon^T][e] \tag{A.8b}$$

Considering previous equation (A.8) and (A.9), the linear constitutive equations become as follow:

(*Stress–Voltage form*)

$$\begin{cases} \{S\} = [s]\{T\} + [g]^t\{E\} \\ \{D\} = [g]\{T\} + [\varepsilon]\{E\} \end{cases} \Rightarrow \begin{cases} S_p = s_{pq}^D T_q + g_{pk} D_k \\ E_i = -g_{iq} T_q + \varepsilon_{ik}^{-1} D_j \end{cases} \tag{A.9a}$$

(*Strain–Voltage form*)

$$\begin{cases} \{T\} = [c]\{S\} + [q]^t\{D\} \\ \{E\} = [q]\{S\} + [\varepsilon]\{D\} \end{cases} \Rightarrow \begin{cases} T_p = c_{pq}^D S_q - q_{pk} D_k \\ E_i = -q_{iq} S_q + \varepsilon_{ik}^{-1} D_k \end{cases} \tag{A.9b}$$

Since they are described by two indices, the matrices of individual elastic, piezoelectric and dielectric constants for any anisotropic material without symmetry center can be now written as following:

- *Elastic compliance matrix*

$$s_{pq}^{E} = \begin{pmatrix} s_{11} & s_{12} & s_{13} & s_{14} & s_{15} & s_{16} \\ s_{21} & s_{22} & s_{23} & s_{24} & s_{25} & s_{26} \\ s_{31} & s_{32} & s_{33} & s_{34} & s_{35} & s_{36} \\ s_{41} & s_{42} & s_{43} & s_{44} & s_{45} & s_{46} \\ s_{51} & s_{52} & s_{53} & s_{54} & s_{55} & s_{55} \\ s_{61} & s_{62} & s_{63} & s_{64} & s_{65} & s_{66} \end{pmatrix} \tag{A.10}$$

- *Elastic stiffness matrix*

$$c_{pq}^{E} = \begin{pmatrix} c_{11} & c_{12} & c_{13} & c_{14} & c_{15} & c_{16} \\ c_{21} & c_{22} & c_{23} & c_{24} & c_{25} & c_{26} \\ c_{31} & c_{32} & c_{33} & c_{34} & c_{35} & c_{36} \\ c_{41} & c_{42} & c_{43} & c_{44} & c_{45} & c_{46} \\ c_{51} & c_{52} & c_{53} & c_{54} & c_{55} & c_{56} \\ c_{61} & c_{62} & c_{63} & c_{64} & c_{65} & c_{66} \end{pmatrix} \tag{A.11}$$

- *Piezoelectric strain coefficient matrix*

$$d_{iq} = \begin{pmatrix} d_{11} & d_{12} & d_{13} & d_{14} & d_{15} & d_{16} \\ d_{21} & d_{22} & d_{23} & d_{24} & d_{25} & d_{26} \\ d_{31} & d_{32} & d_{33} & d_{34} & d_{35} & d_{36} \end{pmatrix} \tag{A.12}$$

- *Piezoelectric stress constant matrix*

$$e_{ip} = \begin{pmatrix} e_{11} & e_{12} & e_{13} & e_{14} & e_{15} & e_{16} \\ e_{21} & e_{22} & e_{23} & e_{24} & e_{25} & e_{26} \\ e_{31} & e_{32} & e_{33} & e_{34} & e_{35} & e_{36} \end{pmatrix} \tag{A.13}$$

- *Permittivity matrix*

$$\varepsilon_{ik}^{E} = \begin{pmatrix} \varepsilon_{11} & \varepsilon_{12} & \varepsilon_{13} \\ \varepsilon_{21} & \varepsilon_{22} & \varepsilon_{23} \\ \varepsilon_{31} & \varepsilon_{32} & \varepsilon_{33} \end{pmatrix} \tag{A.14}$$

The matrix general forms A.10 – A.14 turn out to be very useful since they allow the simplification of more complex constitutive equations. To be more precise, processing conditions and particular crystal symmetry of piezoelectric material determine which components of dielectric

constant and piezoelectric and elastic compliance tensors are non-zero and unique. For instance, in the case of transversely isotropic materials, the material's elastic properties are invariant with respect to rotation of any angle about a given axis and the total number of compliance coefficients reduces to 5.

A.2 FLEXOELECTRIC EFFECT: MATHEMATICAL FORMULATION

The flexoelectric effect can be mathematically introduced via the constitutive equation for the electric polarization *P* [77, 131, 132]. Let's consider a continuum framework of crystalline dielectric material. The linear polarization response *P* to a strain field *S* is typically expressed as in A.1b $P_{pe,k} = e_{kij}S_{ij}$. In crystalline centrosymmetric dielectrics, where piezoelectricity is absent and $e_{kij} = 0$, a non-uniform strain can locally break the inversion symmetry of the unit cell, resulting in an induced dipole moment. In such a case, the bulk contribution to the polarization as a response to an applied macroscopic strain gradient is as following:

$$\{P_{fe}\} = [\mu]\{\nabla S\} \Rightarrow P_{fe,k} = \mu_{klij}\frac{\partial S_{kl}}{\partial x_j} \tag{A.15}$$

where P_{fe} is the flexoelectric polarization induced by the strain gradient, $[\mu]$ is the flexoelectric tensor matrix (μ_{klij} is the flexoelectric constant), *S* is the strain, $\partial S_{kl}/\partial x_j$ is the spatial strain gradient and x_j is the position coordinate, respectively.

The phenomenological fourth-order tensor $[\mu]$ introduced in A.15 is known as the flexoelectric tensor and the associated phenomenon wherein a macroscopic strain gradient induces a linear polarization response in a dielectric is termed flexoelectricity. The flexoelectric tensor $[\mu]$, being a tensor of even order, is nonzero for crystals of any symmetry (including those amorphous), in contrast to the piezoelectric tensor, e_{kij}, which is a third rank tensor and allowed only in non-centrosymmetric media. Since in most general case, a polarization can result from both flexoelectric and piezoelectric effects, the polarization response to an applied deformation in a dielectric may be rewritten as (hereafter the Einstein summation convention is adopted):

$$P_k = e_{kij}S_{ij} + \mu_{klij}\frac{\partial S_{kl}}{\partial x_j} \tag{A.16}$$

According to the previous equation, the piezoelectric effect associates the mechanical stress with the polarization, while the flexoelectric effect relates the strain gradient to the polarization.

Analogous to the piezoelectric effect, an equivalent converse flexoelectric effect can be observed. The converse effect describes the linear coupling between the induced elastic stress and the applied electric field gradient and is typically expressed in the following form:

$$\{T_{fe}\} = [\mu]\{\nabla E\} \Rightarrow T_{fe,k} = \mu_{klij}\frac{\partial E_{kl}}{\partial x_j} \tag{A.17}$$

Here, T_{ij} and $\partial E_{kl}/\partial x_j$ are the induced elastic stress and electric field gradient, respectively.

The flexoelectric constants μ_{klij} were estimated by Sh. M. Kogan [55] and A. K. Tagantsev [133], who predicted this coefficients scale with the dielectric susceptibility of the material and they are in the order of e/a where e is the electronic charge and a the lattice parameter, according to the equation

$$\mu_{klij} = \chi_{ij}\gamma_{kl}\frac{e}{a} \tag{A.18}$$

where χ_{ij} is the susceptibility of the dielectric and γ_{kl} is a constant material parameter tensor.

The magnitude of the flexoelectric effect in a material is assessed by the flexoelectric coefficients. Especially from cantilevered beam based bending experiments for different ferroelectrics, flexoelectric constants – transverse and longitudinal – have been first investigated by Cross [134-136]. For ordinary dielectric materials, the electromechanical coupling associated to the flexoelectric effect has a magnitude of about 10^2 pC/m, while high-performance piezoelectric crystals possess piezoelectric coefficients on the order of 10^2 pC/N. From a qualitative point of view, these coupling coefficients are of the same magnitude, but they differ in units. That is, without introducing permanent plastic deformation to a material, large strain gradients cannot be imparted in the macroscopic materials. By contrast, it is comparatively less difficult to apply reasonable amounts of homogenous stress to the materials. Therefore, the observation of the flexoelectric contribution becomes more difficult than the piezoelectric response. No shear flexoelectric coefficients have been measured directly so far.

The proper notation of the flexoelectric coefficient in matrix form is typically found considering that flexoelectric coefficient is an asymmetrical tensor, due to the gradient term of its definition. Compared with the electrostrictive constant and the elastic constant, it has more non-zero independent components. Exploiting the compressed matrix notation as reported in Table A.1, the most general form of the flexoelectric tensor 6x6 matrix can be written as:

$$\mu_{pq} = \begin{bmatrix} \mu_{11} & \mu_{12} & \mu_{13} & \mu_{14} & \mu_{15} & \mu_{16} \\ \mu_{21} & \mu_{22} & \mu_{23} & \mu_{24} & \mu_{25} & \mu_{26} \\ \mu_{31} & \mu_{32} & \mu_{33} & \mu_{34} & \mu_{35} & \mu_{36} \\ \mu_{41} & \mu_{42} & \mu_{43} & \mu_{44} & \mu_{45} & \mu_{46} \\ \mu_{51} & \mu_{52} & \mu_{53} & \mu_{54} & \mu_{55} & \mu_{56} \\ \mu_{61} & \mu_{62} & \mu_{63} & \mu_{64} & \mu_{65} & \mu_{66} \end{bmatrix} \quad \text{(A.19)}$$

As in the case of piezoelectric constitutive tensor matrices, the total number of flexoelectric coefficients can be decreased by exploiting the symmetry of the material.

A.3 FUNDAMENTAL MATRICES OF ALUMINUM NITRIDE

Exploiting the symmetry of wurtzite-type-structure the anisotropic properties of AlN in matrix annotation can be expressed as summarized in Table A.2 and Table A.3.

Table A.2

Anisotropic material properties of Aluminum Nitride (at 300 K)

Parameter	*Description*	*Value*	*Unit*
$[s_{pq}^{E}]$	*Elastic stiffness matrix*	$\begin{bmatrix} s_{11} & s_{12} & s_{13} & 0 & 0 & 0 \\ s_{12} & s_{22} & s_{23} & 0 & 0 & 0 \\ s_{13} & s_{23} & s_{33} & 0 & 0 & 0 \\ 0 & 0 & 0 & s_{44} & 0 & 0 \\ 0 & 0 & 0 & 0 & s_{44} & 0 \\ 0 & 0 & 0 & 0 & 0 & 2(s_{11}-s_{12}) \end{bmatrix}$ $= \begin{bmatrix} 2.85\cdot10^{-3} & -8.99\cdot10^{-4} & -3.82\cdot10^{-4} & 0 & 0 & 0 \\ -8.99\cdot10^{-4} & 3.11\cdot10^{-3} & -9.64\cdot10^{-4} & 0 & 0 & 0 \\ -3.82\cdot10^{-4} & -9.64\cdot10^{-4} & 3.03\cdot10^{-3} & 0 & 0 & 0 \\ 0 & 0 & 0 & 8\cdot10^{-3} & 0 & 0 \\ 0 & 0 & 0 & 0 & 8\cdot10^{-3} & 0 \\ 0 & 0 & 0 & 0 & 0 & 7.5\cdot10^{-3} \end{bmatrix}$	*1/GPa*

$[c_{pq}^{E}]$	*Elastic stiffness matrix*	$\begin{bmatrix} c_{11} & c_{12} & c_{13} & 0 & 0 & 0 \\ c_{12} & c_{11} & c_{23} & 0 & 0 & 0 \\ c_{13} & c_{23} & c_{33} & 0 & 0 & 0 \\ 0 & 0 & 0 & c_{44} & 0 & 0 \\ 0 & 0 & 0 & 0 & c_{44} & 0 \\ 0 & 0 & 0 & 0 & 0 & \frac{1}{2}(c_{11}-c_{12}) \end{bmatrix} = \begin{bmatrix} 410 & 149 & 99 & 0 & 0 & 0 \\ 149 & 410 & 149 & 0 & 0 & 0 \\ 99 & 149 & 389 & 0 & 0 & 0 \\ 0 & 0 & 0 & 125 & 0 & 0 \\ 0 & 0 & 0 & 0 & 125 & 0 \\ 0 & 0 & 0 & 0 & 0 & 130.5 \end{bmatrix}$	*GPa*
$[d_{iq}]$	*Piezoelectric strain coefficient matrix*	$\begin{bmatrix} 0 & 0 & 0 & 0 & d_{15} & 0 \\ 0 & 0 & 0 & d_{15} & 0 & 0 \\ d_{31} & d_{32} & d_{33} & 0 & 0 & 0 \end{bmatrix} = \begin{bmatrix} 0 & 0 & 0 & 0 & -3.84 & 0 \\ 0 & 0 & 0 & -3.84 & 0 & 0 \\ -1.73 & -2.78 & 5.49 & 0 & 0 & 0 \end{bmatrix}$	*pC/N*
$[e_{ip}]$	*Piezoelectric stress constant matrix*	$\begin{bmatrix} 0 & 0 & 0 & 0 & e_{24} & 0 \\ 0 & 0 & 0 & e_{24} & 0 & 0 \\ e_{31} & e_{31} & e_{33} & 0 & 0 & 0 \end{bmatrix} = \begin{bmatrix} 0 & 0 & 0 & 0 & -0.48 & 0 \\ 0 & 0 & 0 & -0.48 & 0 & 0 \\ -0.58 & -0.58 & 1.55 & 0 & 0 & 0 \end{bmatrix}$	*C/m²*
$[\varepsilon_{ik}^{E}]$	*Permittivity matrix*	$\begin{bmatrix} \varepsilon_{11} & 0 & 0 \\ 0 & \varepsilon_{22} & 0 \\ 0 & 0 & \varepsilon_{33} \end{bmatrix} = \begin{bmatrix} 8 & 0 & 0 \\ 0 & 8 & 0 \\ 0 & 0 & 9.5 \end{bmatrix}$	

The flexoelectric phenomenon is still under study. No numerical value, from theory or experimental measurements, is available for aluminum nitride. In the table below, the main flexoelectric tensors are reported, exploiting the symmetry of the AlN wurtzite-type-structure.

Table A.3

Flexoelectric tensor matrix of Aluminum Nitride (hexagonal 6mm system class)

Parameter	*Description*	*Value*	*Unit*
$[\mu_{pq}]$	*Flexoelectric coefficients matrix*	$\begin{bmatrix} \mu_{11} & \mu_{12} & \mu_{13} & 0 & 0 & 0 \\ \mu_{12} & \mu_{11} & \mu_{23} & 0 & 0 & 0 \\ \mu_{13} & \mu_{23} & \mu_{33} & 0 & 0 & 0 \\ 0 & 0 & 0 & \mu_{44} & 0 & 0 \\ 0 & 0 & 0 & 0 & \mu_{44} & 0 \\ 0 & 0 & 0 & 0 & 0 & \mu_{66} \end{bmatrix}$	*C/m*

BIBLIOGRAPHY

1. Dario, P., et al., *Biologically-Inspired Microfabricated Force and Position Mechano-Sensors*, in *Sensors and Sensing in Biology and Engineering*, F. Barth, J.C. Humphrey, and T. Secomb, Editors. 2003, Springer Vienna. p. 109-125.

2. Drimus, A. and A. Bilberg, *Novel Approaches for Bio-inspired Mechano-Sensors*, in *Intelligent Robotics and Applications*, S. Jeschke, H. Liu, and D. Schilberg, Editors. 2011, Springer Berlin Heidelberg. p. 12-23.

3. Dario, P., et al. *Design, fabrication and applications of biomimetic sensors in biorobotics*. in *Information Acquisition, 2005 IEEE International Conference on*. 2005.

4. Dahiya, R.S., et al., *Tactile Sensing - From Humans to Humanoids.* IEEE Transactions on Robotics, 2010. **26**(1): p. 1-20.

5. Lee, W.W., J. Cabibihan, and N.V. Thakor. *Bio-mimetic strategies for tactile sensing*. in *SENSORS, 2013 IEEE*. 2013.

6. Lederman, S.J. and R.A. Browse, *The Physiology and Psychophysics of Touch*, in *Sensors and Sensory Systems for Advanced Robots*, P. Dario, Editor. 1988, Springer Berlin Heidelberg. p. 71-91.

7. Sadava, D.E., D.M. Hillis, and H.C. Heller, *Life: The Science of Biology*. 2011: W. H. Freeman.

8. Kandel, E.R., et al., *Principles of neural science*. 2014.

9. Vallbo, Å.B. and R. Johansson, *Properties of cutaneous mechanoreceptors in the human hand related to touch sensation.* Hum Neurobiol, 1984. **3**(1): p. 3-14.

10. Johansson, R.S. and J.R. Flanagan, *Coding and use of tactile signals from the fingertips in object manipulation tasks.* Nature Reviews Neuroscience, 2009. **10**(5): p. 345-359.

11. Amato, M., V. Massimo De, and S. Petroni, *Advanced MEMS Technologies for Tactile Sensing and Actuation*, in *MEMS*. 2013, CRC Press. p. 351-380.

12. Dahiya, R. and M. Valle, *Tactile Sensing Technologies*, in *Robotic Tactile Sensing*. 2013, Springer Netherlands. p. 79-136.

13. Kappassov, Z., J.-A. Corrales, and V. Perdereau, *Tactile sensing in dexterous robot hands — Review.* Robotics and Autonomous Systems, 2015. **74, Part A**: p. 195-220.

14. Lee, M.H., *Tactile Sensing: New Directions, New Challenges.* The International Journal of Robotics Research, 2000. **19**(7): p. 636-643.

15. Ohka, M., H. Kobayashi, and Y. Mitsuya. *Sensing characteristics of an optical three-axis tactile sensor mounted on a multi-fingered robotic hand*. in *Intelligent Robots and Systems, 2005.(IROS 2005). 2005 IEEE/RSJ International Conference on*. 2005. IEEE.

16. Ohka, M., et al., *Sensing characteristics of an optical three-axis tactile sensor under combined loading.* Robotica, 2004. **22**(02): p. 213-221.

17. Ohmura, Y., Y. Kuniyoshi, and A. Nagakubo. *Conformable and scalable tactile sensor skin for curved surfaces*. in *Robotics and Automation, 2006. ICRA 2006. Proceedings 2006 IEEE International Conference on*. 2006.

18. Luo, R.-C., F. Wang, and Y.-x. Liu. *An Imaging Tactile Sensor With Magnetostrictive Transduction*. 1985.

19. Nelson, T., et al., *Shear-sensitive magnetoresistive robotic tactile sensor.* Magnetics, IEEE Transactions on, 1986. **22**(5): p. 394-396.

20. Torres-Jara, E., I. Vasilescu, and R. Coral, *A soft touch: Compliant tactile sensors for sensitive manipulation.* 2006.

21. Ando, S., et al., *Ultrasonic six-axis deformation sensing.* Ultrasonics, Ferroelectrics, and Frequency Control, IEEE Transactions on, 2001. **48**(4): p. 1031-1045.

22. Krishna, G.M. and K. Rajanna. *Tactile sensor based on piezoelectric resonance*. in *Sensors, 2002. Proceedings of IEEE*. 2002.

23. Omata, S., Y. Murayama, and C.E. Constantinou, *Real time robotic tactile sensor system for the determination of the physical properties of biomaterials.* Sensors and Actuators A: Physical, 2004. **112**(2): p. 278-285.

24. Najarian, S., J. Dargahi, and A. Mehrizi, *Artificial tactile sensing in biomedical engineering*. 2009: McGraw Hill Professional.

25. Wei, Y. and Q. Xu, *An overview of micro-force sensing techniques.* Sensors and Actuators A: Physical, 2015. **234**: p. 359-374.

26. Choi, W.-C., *Polymer micromachined flexible tactile sensor for three-axial loads detection*. Transactions on electrical and electronic materials, 2010. **11**(3): p. 130-133.

27. Hu, Y., et al., *Bioinspired 3-D tactile sensor for minimally invasive surgery.* Microelectromechanical Systems, Journal of, 2010. **19**(6): p. 1400-1408.

28. Kim, K., et al., *Polymer-based flexible tactile sensor up to 32 × 32 arrays integrated with interconnection terminals.* Sensors and Actuators A: Physical, 2009. **156**(2): p. 284-291.

29. Wettels, N., et al. *Biomimetic Tactile Sensor for Control of Grip*. in *Rehabilitation Robotics, 2007. ICORR 2007. IEEE 10th International Conference on*. 2007.

30. Eun-Soo, H., S. Jung-hoon, and K. Yong-Jun, *A Polymer-Based Flexible Tactile Sensor for Both Normal and Shear Load Detections and Its Application for Robotics.* Microelectromechanical Systems, Journal of, 2007. **16**(3): p. 556-563.

31. Beccai, L., et al., *Development and Experimental Analysis of a Soft Compliant Tactile Microsensor for Anthropomorphic Artificial Hand.* Mechatronics, IEEE/ASME Transactions on, 2008. **13**(2): p. 158-168.

32. Alcheikh, N., et al., *Characterization and modeling of a piezoresistive three-axial force micro sensor.* Sensors and Actuators A: Physical, 2013. **201**: p. 188-192.

33. Castellanos-Ramos, J., et al., *Tactile sensors based on conductive polymers.* Microsystem Technologies, 2010. **16**(5): p. 765-776.

34. Noda, K., et al., *A shear stress sensor for tactile sensing with the piezoresistive cantilever standing in elastic material.* Sensors and Actuators A: Physical, 2006. **127**(2): p. 295-301.

35. Someya, T. and T. Sekitani. *Bionic skins using flexible organic devices*. in *Micro Electro Mechanical Systems (MEMS), 2014 IEEE 27th International Conference on*. 2014.

36. Takahashi, H., et al., *A triaxial tactile sensor without crosstalk using pairs of piezoresistive beams with sidewall doping.* Sensors and Actuators A: Physical, 2013. **199**: p. 43-48.

37. Someya, T., et al., *A large-area, flexible pressure sensor matrix with organic field-effect transistors for artificial skin applications.* Proceedings of the National Academy of Sciences of the United States of America, 2004. **101**(27): p. 9966-9970.

38. Shimojo, M., et al., *A tactile sensor sheet using pressure conductive rubber with electrical-wires stitched method.* Sensors Journal, IEEE, 2004. **4**(5): p. 589-596.

39. Chang, W.-Y., et al., *Flexible electronics sensors for tactile multiscanning.* Review of Scientific Instruments, 2009. **80**(8): p. 084701.

40. Cheng, M.Y., et al., *A flexible capacitive tactile sensing array with floating electrodes.* Journal of Micromechanics and Microengineering, 2009. **19**(11): p. 115001.

41. Cheng, M.-Y., et al., *A Polymer-Based Capacitive Sensing Array for Normal and Shear Force Measurement.* Sensors, 2010. **10**(11): p. 10211.

42. Hyung-Kew, L., et al., *Normal and Shear Force Measurement Using a Flexible Polymer Tactile Sensor With Embedded Multiple Capacitors.* Microelectromechanical Systems, Journal of, 2008. **17**(4): p. 934-942.

43. Kim, H.-K., S. Lee, and K.-S. Yun, *Capacitive tactile sensor array for touch screen application.* Sensors and Actuators A: Physical, 2011. **165**(1): p. 2-7.

44. Maiolino, P., et al., *A Flexible and Robust Large Scale Capacitive Tactile System for Robots.* Sensors Journal, IEEE, 2013. **13**(10): p. 3910-3917.

45. Schmitz, A., et al., *Methods and Technologies for the Implementation of Large-Scale Robot Tactile Sensors.* Robotics, IEEE Transactions on, 2011. **27**(3): p. 389-400.

46. Akiyama, M., et al., *Flexible piezoelectric pressure sensors using oriented aluminum nitride thin films prepared on polyethylene terephthalate films.* Journal of Applied Physics, 2006. **100**(11): p. 114318.

47. Dargahi, J., M. Parameswaran, and S. Payandeh, *A micromachined piezoelectric tactile sensor for an endoscopic grasper-theory, fabrication and experiments.* Microelectromechanical Systems, Journal of, 2000. **9**(3): p. 329-335.

48. Seminara, L., et al., *Electromechanical characterization of piezoelectric PVDF polymer films for tactile sensors in robotics applications.* Sensors and Actuators A: Physical, 2011. **169**(1): p. 49-58.

49. Ikeda, T., *Fundamentals of Piezoelectricity. 1996*. Oxford Science Publications.

50. Jalili, N., *Piezoelectric-based vibration control: from macro to micro/nano scale systems*. 2009: Springer Science & Business Media.

51. Tichý, J., et al., *Fundamentals of piezoelectric sensorics: mechanical, dielectric, and thermodynamical properties of piezoelectric materials*. 2010: Springer Science & Business Media.

52. Vijaya, M., *Piezoelectric Materials and Devices: Applications in Engineering and Medical Sciences*. 2012: CRC Press.

53. Ballas, R.G., *Piezoelectric multilayer beam bending actuators: static and dynamic behavior and aspects of sensor integration*. 2007: Springer Science & Business Media.

54. Zubko, P., G. Catalan, and A.K. Tagantsev, *Flexoelectric effect in solids.* Annual Review of Materials Research, 2013. **43**: p. 387-421.

55. Kogan, S.M., *Piezoelectric effect during inhomogeneous deformation and acoustic scattering of carriers in crystals.* Soviet Physics-Solid State, 1964. **5**(10): p. 2069-2070.

56. Tiwana, M.I., S.J. Redmond, and N.H. Lovell, *A review of tactile sensing technologies with applications in biomedical engineering.* Sensors and Actuators A: Physical, 2012. **179**: p. 17-31.

57. Saccomandi, P., et al., *Microfabricated Tactile Sensors for Biomedical Applications: A Review.* Biosensors, 2014. **4**(4): p. 422-448.

58. Krishna, G.M. and K. Rajanna, *Tactile sensor based on piezoelectric resonance.* Sensors Journal, IEEE, 2004. **4**(5): p. 691-697.

59. Belavic, D., et al. *PZT thick films for pressure sensors: Characterisation of materials and devices*. in *Electronics System-Integration Technology Conference, 2008. ESTC 2008. 2nd*. 2008.

60. Dahiya, R.S., et al., *POSFET tactile sensing arrays using CMOS technology.* Sensors and Actuators A: Physical, 2013. **202**: p. 226-232.

61. Dahiya, R.S., et al., *Piezoelectric oxide semiconductor field effect transistor touch sensing devices.* Applied Physics Letters, 2009. **95**(3): p. 034105.

62. Qasaimeh, M.A., et al., *PVDF-Based Microfabricated Tactile Sensor for Minimally Invasive Surgery.* Microelectromechanical Systems, Journal of, 2009. **18**(1): p. 195-207.

63. Polster, T. and M. Hoffmann, *Aluminum nitride based 3D, piezoelectric, tactile sensor.* Procedia Chemistry, 2009. **1**(1): p. 144-147.

64. Tseng, H.-J., W.-C. Tian, and W.-J. Wu, *Flexible PZT Thin Film Tactile Sensor for Biomedical Monitoring.* Sensors, 2013. **13**(5): p. 5478.

65. Nabar, B.P., Z. Celik-Butler, and D.P. Butler. *Self-powered, tactile pressure sensing skin using crystalline ZnO nanorod arrays for robotic applications.* in *SENSORS, 2013 IEEE*. 2013.

66. Byungjune, C., et al. *Development of Anthropomorphic Robot Hand with Tactile Sensor : SKKU Hand II*. in *Intelligent Robots and Systems, 2006 IEEE/RSJ International Conference on*. 2006.

67. Seminara, L., et al., *A tactile sensing system based on arrays of piezoelectric polymer transducers*. 2012: INTECH Open Access Publisher.

68. Seminara, L., et al. *Piezoelectric polymer transducer arrays for flexible tactile sensors*. in *Sensors, 2012 IEEE*. 2012.

69. Cheng-Hsin, C., et al. *Flexible tactile sensor for the grasping control of robot fingers.* in *Advanced Robotics and Intelligent Systems (ARIS), 2013 International Conference on*. 2013.

70. Akiyama, M., et al., *Preparation of Oriented Aluminum Nitride Thin Films on Polyimide Films and Piezoelectric Response with High Thermal Stability and Flexibility*. Advanced Functional Materials, 2007. **17**(3): p. 458-462.

71. Akiyama, M., et al., *Sensitivity enhancement in diaphragms made by aluminum nitride thin films prepared on polyimide films.* Applied Physics Letters, 2008. **92**(4): p. 043509.

72. Guo-Hua, F., *A piezoelectric dome-shaped-diaphragm transducer for microgenerator applications.* Smart Materials and Structures, 2007. **16**(6): p. 2636.

73. Chunyan, L., et al., *Flexible Dome and Bump Shape Piezoelectric Tactile Sensors Using PVDF-TrFE Copolymer*. Microelectromechanical Systems, Journal of, 2008. **17**(2): p. 334-341.

74. Kim, M.S., et al. *A dome shaped piezoelectric tactile sensor array using controlled inflation technique*. in *Solid-State Sensors, Actuators and Microsystems (TRANSDUCERS & EUROSENSORS XXVII), 2013 Transducers & Eurosensors XXVII: The 17th International Conference on*. 2013.

75. Kim, M.-S., et al., *A dome-shaped piezoelectric tactile sensor arrays fabricated by an air inflation technique.* Sensors and Actuators A: Physical, 2014. **212**: p. 151-158.

76. Huang, W., et al., *A trapezoidal flexoelectric accelerometer.* Journal of Intelligent Material Systems and Structures, 2014. **25**(3): p. 271-277.

77. Majdoub, M.S., P. Sharma, and T. Cagin, *Enhanced size-dependent piezoelectricity and elasticity in nanostructures due to the flexoelectric effect.* Physical Review B, 2008. **77**(12): p. 125424.

78. Kwon, S.r., et al. *A new type of microphone using flexoelectric barium strontium titnate*. 2014.

79. Petroni, S., et al., *Tactile multisensing on flexible aluminum nitride.* Analyst, 2012. **137**(22): p. 5260-5264.

80. Choudhary, V. and K. Iniewski, *MEMS: Fundamental Technology and Applications*. 2013: CRC Press.

81. Cingolani, R., *Bioinspired approaches for human-centric technologies*. 2014: Springer.

82. Heywang, W., K. Lubitz, and W. Wersing, *Piezoelectricity: evolution and future of a technology*. Vol. 114. 2008: Springer Science & Business Media.

83. Defaÿ, E., *Integration of ferroelectric and piezoelectric thin films: concepts and applications for microsystems.* 2013: John Wiley & Sons.

84. Piazza, G., P.J. Stephanou, and A.P. Pisano, *Piezoelectric Aluminum Nitride Vibrating Contour-Mode MEMS Resonators.* Microelectromechanical Systems, Journal of, 2006. **15**(6): p. 1406-1418.

85. Harrington, B.P. and R. Abdolvand, *In-plane acoustic reflectors for reducing effective anchor loss in lateral–extensional MEMS resonators.* Journal of Micromechanics and Microengineering, 2011. **21**(8): p. 085021.

86. Bjurström, J., I. Katardjiev, and V. Yantchev, *Lateral-field-excited thin-film Lamb wave resonator.* Applied Physics Letters, 2005. **86**(15): p. 154103.

87. Rinaldi, M., et al., *Super-high-frequency two-port AlN contour-mode resonators for RF applications.* Ultrasonics, Ferroelectrics, and Frequency Control, IEEE Transactions on, 2010. **57**(1): p. 38-45.

88. Sinha, N., et al., *Piezoelectric aluminum nitride nanoelectromechanical actuators.* Applied Physics Letters, 2009. **95**(5): p. 053106.

89. Sinha, N., et al., *Body-Biased Complementary Logic Implemented Using AlN Piezoelectric MEMS Switches.* Microelectromechanical Systems, Journal of, 2012. **21**(2): p. 484-496.

90. Elfrink, R., et al., *Vacuum-packaged piezoelectric vibration energy harvesters: damping contributions and autonomy for a wireless sensor system.* Journal of Micromechanics and Microengineering, 2010. **20**(10): p. 104001.

91. Ting-Ta, Y., et al., *Corrugated aluminum nitride energy harvesters for high energy conversion effectiveness.* Journal of Micromechanics and Microengineering, 2011. **21**(8): p. 085037.

92. Guedes, A., et al. *Aluminum nitride pMUT based on a flexurally-suspended membrane*. in *Solid-State Sensors, Actuators and Microsystems Conference (TRANSDUCERS), 2011 16th International*. 2011.

93. Shelton, S., et al. *CMOS-compatible AlN piezoelectric micromachined ultrasonic transducers*. in *Ultrasonics Symposium (IUS), 2009 IEEE International*. 2009.

94. Williams, M.D., et al., *An AlN MEMS Piezoelectric Microphone for Aeroacoustic Applications.* Microelectromechanical Systems, Journal of, 2012. **21**(2): p. 270-283.

95. Goericke, F.T., et al. *High temperature compatible aluminum nitride resonating strain sensor*. in *Solid-State Sensors, Actuators and Microsystems Conference (TRANSDUCERS), 2011 16th International*. 2011.

96. Olsson, R.H., et al., *Post-CMOS-Compatible Aluminum Nitride Resonant MEMS Accelerometers.* Microelectromechanical Systems, Journal of, 2009. **18**(3): p. 671-678.

97. Iborra, E., et al., *Piezoelectric properties and residual stress of sputtered AlN thin films for MEMS applications.* Sensors and Actuators A: Physical, 2004. **115**(2–3): p. 501-507.

98. Ababneh, A., et al., *c-axis orientation and piezoelectric coefficients of AlN thin films sputter-deposited on titanium bottom electrodes.* Applied Surface Science, 2012. **259**: p. 59-65.

99. Jin, H., et al., *Deposition of c-axis orientation aluminum nitride films on flexible polymer substrates by reactive direct-current magnetron sputtering.* Thin Solid Films, 2012. **520**(15): p. 4863-4870.

100. Petroni, S., et al., *Aluminum Nitride piezo-MEMS on polyimide flexible substrates.* Microelectronic Engineering, 2011. **88**(8): p. 2372-2375.

101. Guo-Hua, F. and K. Eun Sok, *Piezoelectrically actuated dome-shaped diaphragm micropump.* Microelectromechanical Systems, Journal of, 2005. **14**(2): p. 192-199.

102. Ceseracciu, L., et al., *Contact strength of ceramic laminates.* Composites Science and Technology, 2008. **68**(1): p. 209-214.

103. Stoney, G.G., *The Tension of Metallic Films Deposited by Electrolysis.* Proceedings of the Royal Society of London. Series A, Containing Papers of a Mathematical and Physical Character, 1909. **82**(553): p. 172-175.

104. Boerman, A. and D. Perera, *Measurement of stress in multicoat systems.* Journal of Coatings Technology, 1998. **70**(881): p. 69-75.

105. Hui, C.Y., H.D. Conway, and Y.Y. Lin, *A Reexamination of Residual Stresses in Thin Films and of the Validity of Stoney's Estimate.* Journal of Electronic Packaging, 2000. **122**(3): p. 267-273.

106. Bouchet, J., A.A. Roche, and E. Jacquelin, *Determination of residual stresses in coated metallic substrates.* Journal of Adhesion Science and Technology, 2001. **15**(3): p. 321-343.

107. Hsueh, C.-H., *Modeling of elastic deformation of multilayers due to residual stresses and external bending.* Journal of Applied Physics, 2002. **91**(12): p. 9652-9656.

108. Akhbari, S., et al. *Self-curved diaphragms by stress engineering for highly responsive pMUT*. in *Micro Electro Mechanical Systems (MEMS), 2015 28th IEEE International Conference on*. 2015.

109. Akhbari, S., et al. *Highly responsive curved aluminum nitride pMUT*. in *Micro Electro Mechanical Systems (MEMS), 2014 IEEE 27th International Conference on*. 2014.

110. Naghdi, P.M. and A. Kalnins, *On Vibrations of Elastic Spherical Shells.* Journal of Applied Mechanics, 1962. **29**(1): p. 65-72.

111. Sammoura, F., S. Akhbari, and L. Liwei, *An analytical solution for curved piezoelectric micromachined ultrasonic transducers with spherically shaped diaphragms.* Ultrasonics, Ferroelectrics, and Frequency Control, IEEE Transactions on, 2014. **61**(9): p. 1533-1544.

112. Reddy, J.N., *Theory and analysis of elastic plates and shells*. 2006: CRC press.

113. Timoshenko, S., S. Woinowsky-Krieger, and S. Woinowsky-Krieger, *Theory of plates and shells*. Vol. 2. 1959: McGraw-hill New York.

114. Love, A.E.H., *The small free vibrations and deformation of a thin elastic shell.* Philosophical Transactions of the Royal Society of London. A, 1888: p. 491-546.

115. Guido, F., et al. *Piezoelectric soft MEMS for tactile sensing and energy harvesting*. in *IC Design & Technology (ICICDT), 2014 IEEE International Conference on*. 2014.

116. Petroni, S., et al., *Flexible AlN flags for efficient wind energy harvesting at ultralow cut-in wind speed.* RSC Advances, 2015. **5**(18): p. 14047-14052.

117. Bertacchini, A., et al. *AlN-based MEMS devices for vibrational energy harvesting applications.* in *Solid-State Device Research Conference (ESSDERC), 2011 Proceedings of the European*. 2011.

118. Petroni, S., et al., *Flexible piezoelectric cantilevers fabricated on polyimide substrate.* Microelectronic Engineering, 2012. **98**: p. 603-606.

119. Lee, J.-B., et al., *Effects of bottom electrodes on the orientation of AlN films and the frequency responses of resonators in AlN-based FBARs.* Thin Solid Films, 2004. **447–448**: p. 610-614.

120. Pătru, M., et al., *Structural, mechanical and piezoelectric properties of polycrystalline AlN films sputtered on titanium bottom electrodes.* Applied Surface Science, 2015. **354, Part B**: p. 267-278.

121. Martin, F., P. Muralt, and M.-A. Dubois, *Process optimization for the sputter deposition of molybdenum thin films as electrode for AlN thin films.* Journal of Vacuum Science & Technology A, 2006. **24**(4): p. 946-952.

122. Guido, F., *AlN-based Piezoelectric MEMS for Energy Harvesting by Vibrations and Air Flows (Unpublished doctoral thesis).* Università del Salento, Dipartimento di Matematica e Fisica "Ennio De Giorgi", Lecce, Italy, 2015.

123. Mastronardi, V.M., et al., *Low stiffness tactile transducers based on AlN thin film and polyimide.* Applied Physics Letters, 2015. **106**(16): p. 162901.

124. Mastronardi, V.M., et al., *Piezoelectric ultrasonic transducer based on flexible AlN.* Microelectronic Engineering, 2014. **121**: p. 59-63.

125. Dubois, M.-A. and P. Muralt, *Properties of aluminum nitride thin films for piezoelectric transducers and microwave filter applications.* Applied Physics Letters, 1999. **74**(20): p. 3032-3034.

126. Gerfers, F., et al., *Sputtered AlN thin films for piezoelectric MEMS devices-FBAR resonators and accelerometers*. 2010: INTECH Open Access Publisher.

127. Lueng, C.M., et al., *Piezoelectric coefficient of aluminum nitride and gallium nitride.* Journal of Applied Physics, 2000. **88**(9): p. 5360-5363.

128. Akhbari, S., F. Sammoura, and L. Liwei. *An equivalent circuit model for curved piezoelectric micromachined ultrasonic transducers with spherical-shape diaphragms.* in *Ultrasonics Symposium (IUS), 2014 IEEE International*. 2014.

129. Young, W.C. and R.G. Budynas, *Roark's formulas for stress and strain.* Vol. 7. 2002: McGraw-Hill New York.

130. *IEEE Standard on Piezoelectricity.* ANSI/IEEE Std 176-1987, 1988: p. 0_1.

131. Nguyen, T.D., et al., *Nanoscale Flexoelectricity.* Advanced Materials, 2013. **25**(7): p. 946-974.

132. Yudin, P.V. and A.K. Tagantsev, *Fundamentals of flexoelectricity in solids.* Nanotechnology, 2013. **24**(43): p. 432001.

133. Tagantsev, A.K., *Piezoelectricity and flexoelectricity in crystalline dielectrics.* Physical Review B, 1986. **34**(8): p. 5883-5889.

134. Ma, W. and L.E. Cross, *Observation of the flexoelectric effect in relaxor Pb(Mg1/3Nb2/3)O3 ceramics.* Applied Physics Letters, 2001. **78**(19): p. 2920-2921.

135. Ma, W. and L.E. Cross, *Strain-gradient-induced electric polarization in lead zirconate titanate ceramics.* Applied Physics Letters, 2003. **82**(19): p. 3293-3295.

136. Ma, W. and L.E. Cross, *Flexoelectricity of barium titanate.* Applied Physics Letters, 2006. **88**(23): p. 232902.